2022-12-01

Achieving Safe Use Of Advanced Materials In Drinking Water Through Novel Nano Analytics And Enabling Electrification Using Green Catalyst

Kenneth Ray Flores
University of Texas at El Paso

ACHIEVING SAFE USE OF ADVANCED MATERIALS IN DRINKING WATER

THROUGH NOVEL NANO ANALYTICS AND ENABLING

ELECTRIFICATION USING GREEN CATALYST

KENNETH RAY FLORES

Doctoral Program in Chemistry

APPROVED:

Jorge L. Gardea-Torresdey, Ph.D., Chair

Paul Westerhoff, Ph.D.

Jason G. Parsons, Ph.D.

Sreenivasan, Sreeprasad , Ph.D.

Dino Villagran, Ph.D.

Stephen L. Crites, Jr., Ph.D.
Dean of the Graduate School

by

Kenneth Ray Flores

2022

DEDICATION

This work is dedicated to my mother, Nelda M. Cardenas, who went above and beyond to ensure I continued pursuing my education. Your strong work ethic provided me with a great model early on in life, and I will always be grateful for the sacrifices you made.

This work is also dedicated to Carolina Valdes, you have always provided me with the support I needed to complete this academic venture. It has been a great journey and it would have been impossible without you.

ACHIEVING SAFE USE OF ADVANCED MATERIALS IN DRINKING WATER

THROUGH NOVEL NANO ANALYTICS AND ENABLING

ELECTRIFICATION USING GREEN CATALYST

By

Kenneth Ray Flores

DISSERTATION

Presented to the Faculty of the Graduate School of

The University of Texas at El Paso

in Partial Fulfillment

of the Requirements

for the Degree of

DOCTOR OF PHILOSOPHY

Department of Chemistry and Biochemistry

THE UNIVERSITY OF TEXAS AT EL PASO

December 2022

ACKNOWLEDGMENTS

ABSTRACT

The accumulation of engineered nanomaterials (ENMs) in environmental sectors will continue to increase as more applications are discovered for their unique properties and characteristics. Additionally, the presence of nanomaterials in the environment becomes exacerbated as more consumer products containing nanoparticles are approved for use. It is debated whether the toxic effects of nanoparticles stem from the particles themselves, ionic species, or formation of secondary particles. Therefore, understanding the behavior of nanoparticles in the environment becomes key to discerning the toxicological effects of nanoparticles. Many advancements have been made with ICP-MS to understand the behavior of nanoparticles in the environmental systems, as well as improve trace detection of nanomaterials in complex matrices. The development of single particle inductively coupled mass spectroscopy (spICP-MS) has been imperative to studying nanoparticle stability and accumulation in environmental and biological matrices.

Carbon black (CB) is an ENM with numerous industrial applications and high potential for integration into nano-enabled water treatment devices. However, few analytical techniques are capable of measuring CB in water at environmentally relevant concentrations. Therefore, we intended to establish a quantification method for CB with lower detection limits through utilization of trace metal impurities as analytical tracers. The lanthanum impurity was chosen as a tracer for spICP-MS analysis based on measured concentrations, low detection limits, and lack of polyatomic interferences. CB stability in water and adhesion to the spICP-MS introduction system presented a challenge that was mitigated by the addition of a nonionic surfactant to the matrix. Following optimization, the limit of detection (64 µg/L) and quantification (122 µg/L) for Monarch 1000 CB demonstrated the applicability of this approach for samples expected to contain trace

amounts of CB. When compared against gravimetric analysis and UV–visible absorption spectroscopy, spICP-MS quantification exhibited similar sensitivity but with the ability to detect concentrations an order of magnitude lower. Additionally, a more complex synthetic matrix representative of drinking water caused no appreciable impact to CB quantification. In comparison to existing quantification techniques, this method has achieved competitive sensitivity, a wide working range for quantification, and high selectivity for tracing possible release of CB materials with known metal contents.

As nitrate pollution in groundwater continues to escalate, more is being discovered about the detrimental environmental implications associated with this pollutant. Thus, there is a great necessity for the effective and sustainable remediation of nitrate from water. The electrocatalytic reduction of nitrate (ERN) has been identified as a promising technology with respect to selective product formation (N_2(g) and NH_3/NH_4^+), adaptable instrument configurations, and compatibility with renewable energy sources. Traditional catalysts for ERN applications include expensive platinum group metals, which makes the widespread utilization of this technology economically unfavorable. Alternatively, research within the last five years has shown cost-effective catalytic materials such as bimetallic systems, graphitic composites, metal oxides, and metal sulfides exhibiting substantial activity/selectivity for ERN applications. Herein, we are developing a bioinspired electrocatalyst, molybdenum disulfide supported on graphene oxide (MoS_2/GO), for selective conversion of nitrate pollution into ammonia for resource recovery applications. Utilizing a Cu foam cathode, decorated with MoS_2/GO electrocatalytic ink, has culminated to a low cost and effective 3D design with 93.7% selectivity towards NH_3/NH_4^+. Following system optimization this cathodic design has a high potential for implementation as a resource recovery technology for nitrate pollution.

TABLE OF CONTENTS

LIST OF TABLES

LIST OF FIGURES

CHAPTER I

ENVIRONMENTAL APPLICATIONS AND RECENT INNOVATIONS IN SINGLE PARTICLE INDUCTIVELY COUPLED PLASMA MASS SPECTROMETERY[1]

Introduction

The continual discovery of new and exciting characteristics of nanomaterials has led to their widespread use in research and, more recently, consumer products. The application of engineered nanoparticles, as well as their incorporation into textiles and consumer products, has increased the potential for environmental contamination. In 2014, there were more than 1800 consumer products on the market containing nanomaterials, according to the nanotechnology Consumer Product Inventory (CPI).[2] Once introduced into the environment, the number of possible interactions becomes tremendous including interactions with various biological systems. However, the properties and behavior of nanomaterials tend to be matrix-dependent and dynamic, making the study of the interactions of nanoparticles in the environment inherently difficult.[3] Recently, there has been a significant push to develop analytical techniques capable of simultaneously detecting and characterizing nanoparticles in various matrices.

spICP-MS has been the focus of development in recent years for its ability to analyze metal containing nanomaterials. spICP-MS has the capability to study nanoparticles with respect to size, elemental composition, physicochemical states, and particle concentrations at environmentally

---

[1] Reprinted from K. Flores, R. Turley, C. Valdes, Yuqing Y., J. Cantu, J. Hernandez, J. Parsons, J. Gardea (2019) Environmental applications and recent innovations in single particle inductively coupled plasma mass spectrometry (SP-ICP-MS). *Applied Spectroscopy Reviews*, 56, ©2019 Taylor & Francis. All rights reserved.

relevant concentrations.[4] Single particle analysis using ICP was first reported in 1986 when the technique was implemented with ICP optical emission spectroscopy (ICP-OES). The authors utilized spICP-OES for analysis of airborne and aerosol particles.[5] Currently, the SP technique has become more applicable to ICP-MS instrumentation due to the capability of detecting ion pulses on a "particle to particle" basis. The ability to detect ion pulses from individual particles stems from the instruments' acquisition speed, which is comprised of a combination of the dwell and settling times. The dwell time of an instrument refers to the duration where analysis or a reading is occurring. The settling time refers to the stabilization time of the electronics between readings. The application of ICP-MS in SP analysis occurs with the application of a minimal settling and maximum dwell time, which allows for the detection of a pulse from an individual particle.[6] Due to the sensitivity of the mass selective detector and the fast acquisition speed, particle samples analyzed by ICP-MS must be diluted to appreciably low concentrations. The dilution of the particle solution ensures the detected pulses arise from a single particle rather than an overlap of multiple particles, which is referred to as coincidence.[7] Transport efficiency becomes an extremely important parameter in spICP-MS, which is defined as the amount of analyte reaching the plasma with respect to total analyte taken by the sampling system. Transport efficiency needs to be established before either particle sizing or particle concentrations can be determined. To determine particle concentrations for a given sample, the transport efficiency is applied to account for volume loss of the sample during nebulization. For the sizing of nanoparticles, the transport efficiency used to compensate for differences between mass transport of single nanoparticles and dissolved ions during the nebulization process.[8] The ability of the transport efficiency to account for the effects of minute variations is measured during the daily performance testing and are crucial in validating data produced by spICP-MS analysis. Transport efficiency is further utilized by this

technique to relate concentration to elemental mass based on the relationship displayed in equation 1. As with any other traditional mass-based technique signal intensity must be first be related to concentration through a dissolved standard calibration curve. Once these relationships are established, and the matrix background is analyzed, the pulse intensities from an unknown nanoparticle sample can be converted to mass per events for particle analysis by applying equation 2. If a density is applied to the analyte, particle sizing can be accomplished based on assuming a spherical geometry displayed in equation 3.[8]

$$(1)\ W = [\eta_n \cdot q_{liq} \cdot t_{dt} \cdot C]$$

W is the mass observed per event, η_n is the transport efficiency, q_{liq} is the sample flow rate, t_{dt} analysis dwell time, and C (μg/ml) is the analyte concentration

$$(2)\ m_p = f_a^{-1} \left[\frac{\left((I_P - I_{Bgd})\eta_i \right) - b}{m} \right]$$

Where m_p is the mass of the corresponding particle, f_a is the mass fraction of the analyzed element in the particle, I_P is the intensity of a pulse from an individual particle, I_{Bgd} is the average background intensity, η_i is the particle ionization efficiency and m and b are the slope and y-intercept from the dissolved calibration curve.

$$(3)\ d = \sqrt[3]{\frac{6m_p}{\pi\rho}}$$

Where d is the diameter of the particle, and ρ is the particle density.

The release of anthropogenic nanomaterials into the environment will be a continuing, persistent, and increasing trend for as long as industrial activities continue. Since the industrial revolution, both direct and indirect actions of humans have led to the generation of incidental nanoparticles, which can persist and change within the environment.[9] Both incidental nanoparticles and engineered nanomaterials (ENMs), which are synthesized for specific properties and

characteristics, are relatively new materials added to the natural material cycles of the earth. Therefore, the impacts and implications of these types of materials existing in nature need to be further understood. Components of the environment such as water, soil, air, and organisms control the migration paths as well as the degree of transformation of these materials. Understanding the transformations of nanomaterials in specific environmental components is key to determining possible toxicological effects of nanoparticles. Evaluation of nanomaterials internalized by biological organisms is equally necessary to further understanding of nanomaterial toxicology [10–13]. spICP-MS is helpful in nanoparticle analysis due to the ability to detect, quantify, and characterize particles in environmentally relevant conditions. Compared to other analytical techniques such as transmission electron microscopy (TEM), spICP-MS is able to operate in environmentally relevant concentrations (μg/L – ng/L) without the need for complex sample preparation.[14] Solution variables such as nanoparticle concentration, pH, dissolved organic content, and ionic strength greatly affects the characteristics of nanoparticles.[15,16] Therefore, analyzing these types of materials with minimal changes to the solution conditions will help provide a better understanding of the behavior of nanoparticles in the environment.

In recent years many improvements have been made to spICP-MS analysis to overcome issues related to limited resolution, matrix and isobaric interferences, low transport efficiency, and fixed mass scanning per analysis. Through the attachment of complementary instrumentation to spICP-MS analysis, issues such as matrix interferences can be resolved by separating individual components of the samples. Once components are separated, the signal to noise ratio can increase, which directly affects the resolution of spICP-MS analysis for target nanoparticles. The utilization of laser ablation has been shown to greatly increase the transport efficiency of spICP-MS analysis, when compared to traditional nebulization. Furthermore, the use of reaction/collision cells have

been shown to decrease isobaric interferences through selective ion – molecule chemistry.[17] Once ionized in the plasma, the sample components (ions) mix with gases to create "new" chemical species, which can be accounted for by anticipating the mass shift of the target analyte in newly created molecules. In addition, the incorporation of detection principles such as time of flight (TOF) mass spectroscopy can greatly increase the diversity of SP-ICP-MS. Unlike the traditional quadrupole for mass selection, the TOF mass spectrometer provides a method for the detection of multiple masses in a single point analysis. TOF expands the possibility for the detection and characterization of multiple nanoparticle identities in a single analysis. Furthermore, TOF can allow for the discrimination between natural and synthetic nanomaterials.[18] spICP-MS analysis will continue to adapt as the needs for detection and resolution of nanomaterials evolves. The proper characterization, identification, and the transformations of nanomaterials in the environment will be paramount in developing an understanding of the consequences of nanomaterials in the environment.

1.0 Environmental Leaching of ENMs from Consumer Products

The global nanotechnology market continues to grow due to the vast range of ENMs applications and the potential influence of these materials on various economic sectors. However, the rapid growth and commercialization of ENMs presents a challenge for risk assessment and regulation associated with ENM technology. The high number of commercial nanomaterial-containing consumer products (over 1800 manufacturer-identified products) complicates risk assessment. The complicated risk assessment further exacerbates the regulation of ENMs due to the different types of ENMs and the seemingly endless applications.[2] In 2006, one of the first publications to recognize the requirements for the "safe handling of nanotechnology" identified the need to develop instruments capable of monitoring ENMs.[19] Presently, the same challenges

persist and the need to develop new methodologies and instrumentation to evaluate nano-enhanced products have been echoed in recent publications.[20,21] From an analytical perspective, the evaluation of nanomaterials presents obstacles such as the need to determine particle size, elemental composition, low analyte concentration, and matrix interferences. A complete characterization of ENMs is often complex and requires the use of multiple techniques.

spICP-MS is a technique that has evolved to address the knowledge gap in ENM analysis. The technique has the capability of characterizing the size and number of ENMs; furthermore, owing to the detector, spICP-MS can identify ENMs at environmentally relevant concentrations (e.g. ng/L). Thus, spICP-MS has established itself as a valuable characterization and monitoring tool to evaluate the release of ENMs from nano-enhanced consumer products into the environment. Table 1.1 shows a list of studies that have used spICP-MS to evaluate the release of ENMs from consumer goods.

Table 1.1: Analytes evaluated by SP-ICP-MS from different consumer products, the extraction medium used, transport efficiency (TE) standard, dwell time, and obtained results. NS=Not specified.

Analyte	Sample	Medium	TE Standard	Dwell time [milliseconds]	Results	Reference
Ag	Textiles	Water & Detergents	100 nm Au NPs	5	Particle size distribution of 100nm and 50nm.	Mitrano et al., 2016
Ag	Textiles	Artificial sweat	60 nm Au NPs	3	Citrate coated AgNPs dissolved less than uncoated AgNPs.	Wagener et al., 2016
Ag	Medical plaster	Artificial sweat	75nm Ag NPs	50	AgNPs (50nm) represent >0.4% of the total Ag.	Aznar et al.,
Ag	Food box & Baby bottle	Food simulant	40nm & 60nm AgNPs	10	Particle size distribution in the 18-30nm range represent 0.1-8.6% of the total Ag.	Ramos et al., 2016
Ag	Plastic food containers	Food simulant	NS	3	Acidic environment promoted dissolved Ag. The total mass of particulate Ag was higher in acidic environment.	Mackevica et al., 2016
Ag	Plastic food containers	Food simulant	N/A (used a microdroplet generator)	1	Approximately 12% of the total Ag is in the form of AgNPs	von Goetz et al., 2013
Ag	Toothbrushes	Water	60 nm Au NPs	3	AgNPs median size of 42-47nm. Total Ag released was 10.2ng	Mackevica et al., 2017
TiO$_2$	Textiles	Water	60 nm Au NPs	100	Particle sizes 27-200nm. Released nano fraction accounts for 0-80% of total TiO2 release	Mackevica et al., 2018
TiO$_2$ & ZnO	Sunscreen	water	60 nm Au NPs	5	TiO$_2$ particles with average size of 107nm. ZnO	Bocca at al., 2018

					particle size 98nm.	
TiO_2 & Au	Cosmetics and personal care products	Water and SDS solution	30, 50 and 100 nm Au NPs	100	TiO_2 particles with average sizes of 30 to 120nm	De la Calle et al., 2017
TiO_2	Sunscreen	Water	50, 80 and 100 nm Au NPs	100	TiO_2 particles with average sizes from 32 to 40nm	Dan et al., 2015
Cu	Antifouling paint	Water	30nm Au NPs	NS	TiO_2 average size of 44nm	[22]
Pt	Road dust	Water	60 nm Au NPs	5	Pt particulates of 9 and 21 nm.	Folens et al., 2018

1.1 Nanoparticles in textiles

Silver nanoparticles (AgNPs) are the most highly used nanomaterial in consumer products due to their antimicrobial properties.[2] Silver in the nano-form has shown enhanced properties, compared to the bulk material, such as an increased bactericidal behavior as well as the possibility to minimize the total amount of silver used in a product.[23] Furthermore, the use of AgNPs in textiles has the advantage of higher breathability compared to other forms of silver, such as microscale silver.[24] However, the elevated number of consumer products that incorporate AgNPs and the absence of regulations have presented a challenge in the risk assessment of the nanomaterial. The spICP-MS technique has been applied to addressing the emerging challenges. spICP-MS has been used to rapidly resolve physical/chemical properties of AgNPs used in consumer products under realistic exposure and release scenarios.

Mitrano *et al*. studied the effects of sunlight and laundering on nano-enhanced textiles, which showed the presence of AgNPs in the wash solution with predominant particle sizes of 100nm (i.e. original particle size) and 50nm.[24] The study also showed that nano-enhanced textiles exposed to light and then washed released less Ag than when washing alone. The results suggest a stabilization of the AgNPs by exposure to sunlight. As a quality control measure, the study used 100nm citrate stabilized Au ENMs as inert tracers to distinguish between mechanically induced release of

nanoparticles and chemical release associated with oxidative dissolution of the Ag nanoparticles. Due to the limitation of the detection limit of the technique, the authors did not analyze fabrics containing AgNPs of <30nm. In a similar study, Wagener *et al.* evaluated the migration of AgNPs from AgNP-enhanced textiles into artificial sweat at pH 8 and 5.5.[25] The study used NIST 60 nm gold nanoparticles as a reference standard and a dwell time of 3 milliseconds for the SP-ICP-MS analysis, a shorter time in comparison to the 5-millisecond dwell time utilized by the Mitrano group. This shorter dwell time led to an improvement in sizing resolution up to 20nm for AgNPs. Improved detection limits are not always ensured with a reduction in dwell time. Significant reduction to this variable may result in multiple reading for a single particle, referred to as a split particle event. Thus, both concentration and particle size must be considered when optimizing for dwell time.[26] The results from the study showed that the citrate coating of AgNPs had an influence in the dissolution behavior; however, textiles with both coated and uncoated AgNPs displayed an average decrease in particle size. The authors concluded the decrease in NP size was indicative of dissolution of the NPs.

Isobaric interferences can be a challenge for spICP-MS but reaction or collision cells help to mitigate this problem; nevertheless, using alternative isotopes can reduce the sensitivity of the analyte of interest. One option to determine the effect of isobaric interferences is to analyze the sample twice, which accounts for both the analyte and the isobaric interference. Mackevica *et al.* followed the latter approach when analyzing nano-titanium dioxide (TiO_2) release from textiles.[27] The study analyzed both ^{48}Ti and ^{48}Ca to correct for the isobaric interference and found that some synthetic fabrics release 80% of the total Ti (3.13 mg/L) as NPs (50-75nm). It should be noted, nanoscale titanium dioxide is also used in a variety of personal care products such as cosmetics and sunscreens. Studies have successfully used surfactants (e.g. SDS, Triton X-100) or extraction

steps (e.g. hexane) to disperse sunscreen before spICP-MS analysis.[28–30] The results demonstrated that TiO$_2$ in the sunscreen samples occurred as nano-TiO$_2$ (Table 1.1).

1.2 Nanoparticle impregnated products

In addition to textiles, SP-ICP-MS has been used to evaluate the leachability of ENMs from other consumer products, providing invaluable information for risk assessment studies. Simultaneously, the data collected from these types of studies has been used to strengthen and optimize the technique's methodology. Aznar *et al.* used spICP-MS to analyze artificial sweat exposed to medical plaster that claimed Ag content.[31] The authors evaluated two ENMs standards, gold (NIST 60nm) and silver (PVP coated Ag NIST 75nm), selecting the latter due to its improved precision. In addition, the study determined that the analysis was not improved by the addition of a separation step using asymmetrical flow field flow fractionation. After eighteen hours of simulated friction, AgNPs (approximately 50 nm) were detected in the artificial sweat, although the ENMs represented less than 0.4% of the detected Ag.

Plastic food containers are other consumer products that incorporate AgNPs for their antimicrobial properties. Von Goetz *et al.* investigated the migration of AgNPs from four commercially available nano-enhanced plastic food containers into four food simulants over various exposure periods.[32] The results showed that acidic food simulants (i.e. 3% acetic acid) had the largest Ag migration with 0.5 ng/cm^2. spICP-MS demonstrated approximately 12% of the total Ag was released with particle sizes ranging from 100 to 350 nm. It should be noted, the authors used a microdroplet dispenser to introduce the sample into the plasma, which achieved a 100% transport efficiency. Similar experiments have corroborated that acidic food simulants (3% acetic acid) show the highest migration of AgNPs occurs with sizes ranging from 18 to 89 nm.[33,34]

Apart from nanomaterials used intentionally in products, incidentally created nanoparticles may also be studied by spICP-MS analysis at environmentally relevant concentrations. Folens *at al.* investigated the platinum (Pt) NPs found in road dust as a result of emissions from catalytic converters.[35] The study used water to extract the Pt and found the total concentration was in the ng/g range with a predominant size of 18nm.The authors concluded that despite the low concentrations of Pt, spICP-MS was suitable for the analysis.

2.0 Environmental spread of NPs – water, air, and soil systems

The incorporation of ENMs into consumer products and textiles, as well as their purposeful application, has increased their potential for environmental contamination.[36] Utilization of spICP-MS has allowed for the efficient and accurate analysis of ENMs in a variety of environmental samples as well as complex matrices. Air, water, and soil systems act as a means of transport for ENMs dictating their migratory path as well as their physical and chemical states. The size distribution of ENMs, at environmentally relevant conditions, and the degree of transformation (aggregation, dissolution, and dissolution/reprecipitation) are crucial information for the determination of environmental fate.[31]

2.1 NPs in water systems

The transport behavior of ENMs refers to both the chemical and physical changes occurring to the particles while in natural water systems. Currently, spICP-MS has been used to track changes in ENM size distributions, particle concentrations, and the ratio of particulate-to-dissolved ions in environmental waters. R. Merrifield *et al.* found concentration to be a major factor in the transport behavior of gold-silver core-shell nanoparticles (NPs) in moderately hard waters (MHW).[37] The authors observed that dilute and environmentally realistic concentrations encouraged the dissolution of the silver shell, while the gold core remained stable. Conversely, higher NP

concentrations showed appreciable agglomeration of the particles in the same media, promoting silver shell stability. Under dilute conditions, the homo-agglomeration of the nanoparticles was limited, encouraging the oxidation and dissolution of the silver shell. However, the gold core of the nanoparticles tended to express a higher level of stability in both dilute and concentrated conditions.[38]
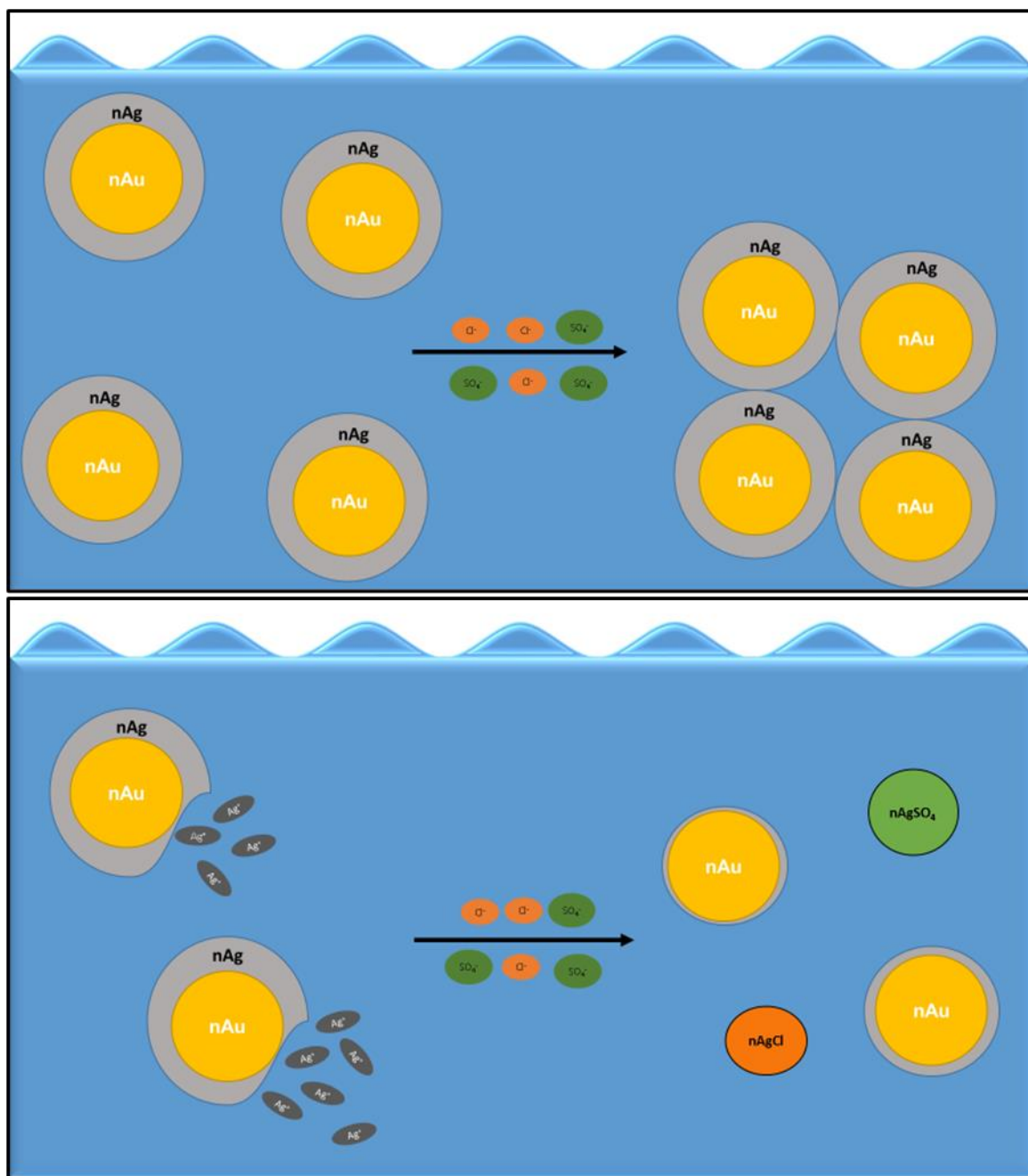
Figure 1.1: Effects of concentration on the stability of gold core - silver shell nanoparticles. Higher concentrations encourage agglomeration while lower concentrations bring forth dissolution and secondary particle formation.

The dissolution of citrate and polyvinylpyrrolidone coated AgNPs (80nm) was reported in municipal waste waters (WW), which lead to the formation of secondary nanoparticles with a composition nAg_xS_y (22nm). The formation of the incidental nanoparticle was thought to occur by the interaction of Ag^+ ions with inorganic sulfides and dissolved organosulfur compounds, which

are a portion of the dissolved organic matter (DOM). DOM concentrations and the level of AgNP dissolution has been reported to exist in an inversely proportional relationship, with DOM acting as a stabilizing agent. Conversely, dissolved oxygen (DO) concentrations tend to exist in a directly proportional relationship with AgNP dissolution.[39] The toxicity of AgNPs to environmental receptors (i.e. living organisms) was thought to be solely caused by the release of Ag^+ ions from the particles. However, results reported by Azimzada *et al.* revealed additional complexity to AgNP toxicity.[40] The authors utilized spICP-MS to determine particle concentrations of dissolved Ag^+ and AgNPs. The concentration determination was performed in tandem with a bioavailability study using *C. reinhardtii* (green algae) as the model organism. With optimized conditions, including a 500 µs dwell time, analysis by spICP-MS could detect silver down to a concentration of 0.02 ng/L (ppt). The concentration of bioavailable silver could not be explained the by the levels of dissolved silver alone. The data indicated that small AgNPs and/or complexed Ag species contributed to the expressed bioavailability. The continued enhancement of the ability of spICP-MS to distinguish between dissolute or agglomerated particles, by signal characterization, has been shown to be fundamental in establishing the transport behavior of ENMs.[41]

The environmental fate of ENMs has been shown to be affected by the removability of common wastewater and drinking water treatment processes. A simulated study focusing on the removal of AgNPs during wastewater processing showed the NP size was the primary variable. A study on the water treatment of AgNPs showed that the bulk of the 40nm NPs were partitioned into the sludge fraction of the treatment sample. The authors of the study indicated the partition was occurring through hetero-aggregation with native particle populations. However, AgNPs of 10nm tended to bypass this aggregation, which suggests smaller particles possess greater environmental persistence.[42] A similar result was reported for removal of zinc containing

14

nanoparticles (75nm) and spiked zinc oxide (ZnO) particles (80-200nm) during a simulation of drinking water treatment. The authors observed, approximately 80% of NPs were removed during the alum coagulation process; furthermore, the authors showed the persistent zinc particles had a size distribution of 35-50 nm.[43] Both drinking and wastewater treatment processes showed size dependent fate dynamic where larger particles were accumulated in treatment media. spICP-MS analysis of ENMs under water and waste-water treatment conditions tends to be challenging, specifically in achieving appropriate signal to noise ratio, including low detection limits, and the ability to distinguish ENMs from other chemical forms. Researchers have utilized chromatography systems to alleviate problems in complex matrices. Coupled chromatography systems allow for the separation of sample components before ionization and analysis. Reverse phase chromatography coupled to spICP-MS has allowed for the separation and speciation of samples. However, hydrodynamic chromatography has been utilized for the separation of components by hydrodynamic radii. In either case, the separation of analyte from the matrix allows for higher level of specificity, sensitivity, and better analysis of the targeted ENM.[44,45]

2.2 Nanoparticles in air and aerosol systems

Single particle aerosol mass spectroscopy (SPAMS) has been used for the determination of emissions and distribution patterns of nanoparticles. In comparison to filter-based analytical techniques and traditional individual particle measurements, SPAMS is advantageous due to the continuous real-time detection of single particles.[46] The ability to monitor size distributions, chemical composition, and aging process of nanoparticles will help determine both the environmental and human health effects of nanoparticles.

SPAMS has been utilized in areas with high pollution and/or incidences of respiratory ailments. This technique monitors the changes to nanomaterials, engineered and naturally

occurring alike, under a variety of conditions. A study performed in Beijing utilized SPAMS to categorize particles by size and composition during clear, hazy, and dusty conditions. Carbonaceous and potassium-rich particles were observed to dominate under all conditions (25-54%). Whereas, metal containing NPs were observed in higher percentages during hazy days; secondary particle formation was observed for all nanoparticle classes (potassium-rich, carbonaceous, metal containing, dust, and sodium-rich).[47] Many industrial processes, including metallurgical manufacturing, greatly contribute to the environmental spread of potentially toxic particulate matter. Samples collected near an iron-manganese alloy manufacturing plant reported that captured particles were predominantly calcium, manganese, and aluminum containing. The abundance of NPs was observed to vary depending on the area where the samples were collected. For example, near the sintering unit (i.e. formation of solid mass by heating and increased pressures – no liquification) calcium containing particles dominated the firing area, while manganese and aluminum containing particles were observed to dominate in the cooling area. The analysis of samples from the smelting unit (extraction of metal from ore using melting and heating) showed manganese containing particles were of the highest abundance.[48] Characterization of the physicochemical properties of airborne particulate matter is key to identifying any possible toxicological effects.

2.3 Nanoparticles in soil and sediments

It has been shown in the literature that the introduction of ENMs from anthropogenic contributions into soil and sediment systems occurs through byproducts from industrial activities, soil amendments with wastewater sludge, deliberate environmental applications, and leaching from ENM-containing products.[49] In addition, ENMs can enter soil and sediment systems through interaction with bordering air and water systems. Bordering systems can introduce ionic metals

16

that may eventually transform into metal containing nanoparticles through biological and/or chemical reductions.[50] ENMs and naturally occurring nanomaterials (NNMs) can further undergo transformation through interactions with trace elements and natural organic matter (NOM). High colloidal concentration in soils creates hydrophobic characteristics and/or negative electrostatic charges. The soil matrix characteristics add complexity to ENM & NNM analysis by using spICP-MS. Current research efforts have required the modification of extraction/preconcentration methods before introduction into the instrument, which allows for the accurate analysis of nanoparticle concentration, size distributions, and particle state.

Conventional extraction methods include the use of dialysis, centrifugation, filtration, liquid-liquid extraction, or liquid-solid extraction, which can affect the physicochemical properties of the NPs.[51] To overcome the aforementioned challenge, Mahdi *et al.* developed a specific method for the extraction and characterization of silver NPs from soil media.[50] This extraction method was comprised of three stages: pre-wetting, aqueous extraction, and spICP-MS analysis. The authors noted the percent recoveries of silver NPs were low at 32% and 46% for sandy and clay-containing soils, respectively. In addition, the technique had low reproducibility, which ranged from 25 to 29%.[50] Another technique for NP isolation from complex matrices, includes cloud point extraction (CPE). The CPE method has been utilized to extract and pre-concentrate gold NPs from spiked soil samples. CPE employs the use of surfactants to create micelles for the extraction of hydrophobic compounds. The supernatant (surfactant deficient layer) must be treated with additional compounds such as salts, NaCl or $CaCl_2$, and acid to decrease the coulombic repulsions and the overall charge on the NPs. Hadri *et al.* showed the use of only surfactant (TX-114) and the use of surfactant plus NaCl maintained a consistent particle size of 60nm. However, the authors also showed the use of the same surfactant in combination with HNO_3 or $CaCl_2$ created an

extractant with two separate average particle sizes. The authors attributed the inconsistency in sizing to aggregation of the gold nanoparticles (AuNPs). It should be noted, recoveries of >90% were observed for sole TX-114 extractions, as well as with the TX-114 + NaCl.[51] The development of efficient extraction methods, that do not alter the physicochemical state of NPs, are crucial for spICP-MS analysis for NPs in their environmental state.

The complexity of ENMs characterization in soil increases with the presence of naturally occurring nanoparticles (NNPs). Traditional spICP-MS has the capacity to detect one single isotopic signature per analysis. The inability to detect more than one isotope during an analysis makes it impossible to distinguish between NNPs and ENMs, which is generally achieved through isotopic fingerprinting. Praetorius *et al.* utilized spICP-TOFMS (Time-of-Flight Mass Spectrometer) for simultaneous multi-element or isotope detection to distinguish between NNPs and ENMs in soil.[18] The authors determined that CeO_2 ENMs contained exclusively Ce; whereas, naturally occurring CeO_2 contained variable amounts of rare earth elements (REEs).[18] Traditionally, REEs normally fall below the limit of detection due to the low concentration of REEs in the analysis of naturally occurring CeO_2, which results in falsely classifying NNPs as ENMs. The limits of detection, in units of mass per particle, for Ce and La were reported at 0.14 and 0.13 fg for analysis by spICP-TOFMS. Incorrectly classified NPs are an issue in environmental nanotechnology research. The study by Praetorius *et al.* applied a threshold and a machine learning algorithm to reduce the number of false positives when distinguishing between NNPs and ENMs. The machine learning algorithm was applied within the data processing software of spICP-MS to produce a predictable empirical model incorporating recursive feature elimination with cross validation (RFECV). Samples using manual identification of nanoparticles in one sample (containing only NNPs) led to false identification of all 300 NP samples as ENMs; however, the

use of machine learning algorithm and RFECV lead to proper classification of 292 NPs as naturally occurring, which showed the validity of the process.

Identification and accurate characterization of nanoparticles, engineered and naturally occurring alike, is an inherently difficult task. The task is complicated due to particle transformations and complex matrices. To overcome these issues, characterization/separation techniques in tandem with spICP-MS, including statistical processing, are necessary to solidify this technique for NP characterization in a wide variety of applications.

3   Analysis of nanoparticles in various biological tissues

spICP-MS has been applied extensively to nanoparticle analysis in aqueous media, there is still a need for the development and application to the analysis of biological tissues from plants and animals. The long-term effects of NPs on living organisms will be resolved by further understanding the accumulation and physicochemical state in specific biological samples. Exposure to NPs is inevitable, whether through direct contact or trophic transfer. Consequently, investigating possible toxicological effects is paramount for both human and environmental health.

3.1 Enzymatic digestions prior to spICP-MS analysis

Conventionally, the techniques used for analyzing NPs include electron microscopy with energy dispersive spectroscopy, dynamic light scattering, UV-Vis spectroscopy, powder X-ray diffraction, and static light scattering. Although these techniques are widely applied, they are limited with respect to concentration analysis, real time data collection, and are generally unsuitable for the concentrations of NPs found in biological systems.[52] However, spICP-MS delivers a robust method of analysis providing statistical and quantitative information on NPs with real-time data collection. With respect to NPs in biological matrices, it is common practice for spICP-MS analysis to be performed in tandem with enzymatic digestions. In general, enzymatic

digestions are used to selectively degrade biological matrices, without changing the physicochemical state of the NPs. Studies have focused on alkaline digestions using tetramethylammonium hydroxide in comparison to enzymatic digestions in samples of mouse and human placental tissues for the extraction of AgNPs.[53,54] While alkaline digestions tend to be more cost-effective, they tend to affect the state of NPs rendering them unsuitable for single particle analysis.

Current applications of enzymatic digestions include the use of protease for the extraction of NPs in animal tissues and a combination of pectinase, cellulase, and hemicellulase has been found effective for NP extraction from plant tissue.[54] Proteinase K has been utilized in enzymatic digestion of animal samples including various organ tissues [55,56], placental tissues [54,57], earthworms [58], and consumable meats.[59] The proteinase K enzyme is known for its stability and high reactivity for the degradation of proteins into amino acids. Macerozyme R-10, a commercial enzymatic digesting product, is widely used in the pretreatment of plant samples. The macerozyme R-10 product contains a combination of pectinase, cellulase, and hemicellulase, which has been shown to digest plant tissues without affecting NP size with a variety of NPs including CuNPs [60], PdNPs [61], PtNPs [62] and CeNPs.[63] For quality control purposes, NPs suspension can be spiked into control plant samples before digestion to confirm the NPs remain unaltered.[62] Alternatively, calibration standards (0–5 µg/L dissolved Ce) have been added to diluted control plant digestate to match the sample matrix for each plant.[63]
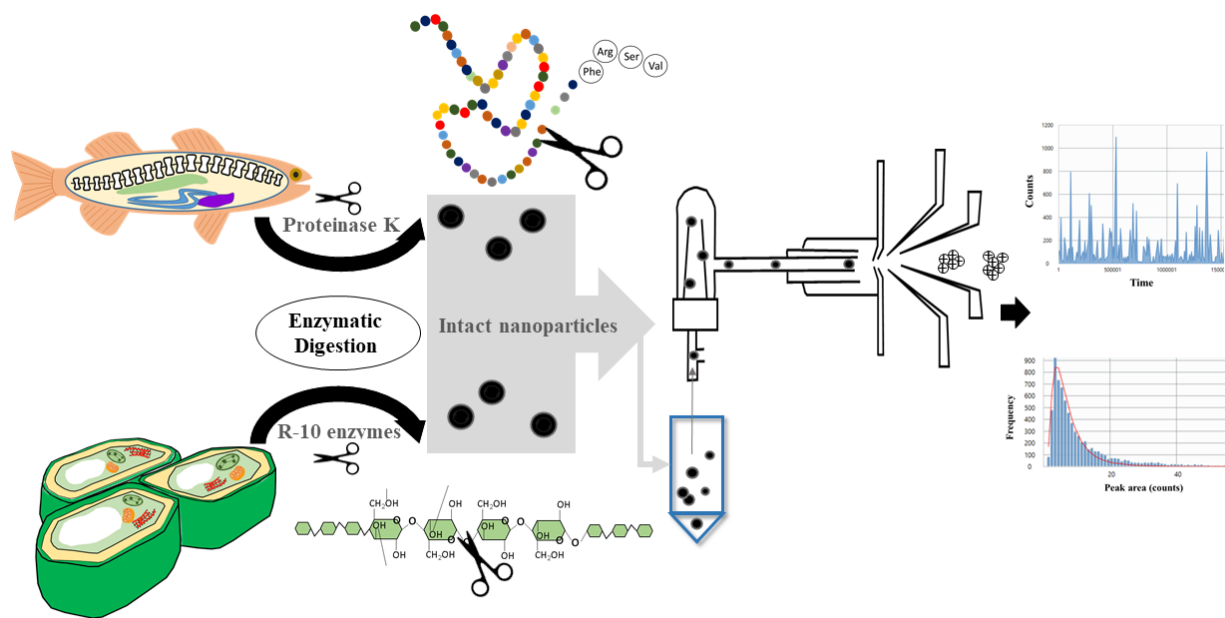
Figure 1.2: Enzymatic digestions of biological matter and tissues preserves nanoparticle size and composition providing a means to liberate nanoparticles from a sample for analysis by spICP-MS without altering their chemical or physical properties.

3.2 Nanoparticle-plant interactions and spICP-MS analysis

Due to the widespread application of NPs in agriculture, there exists a concern for the accumulation of NPs in food crops and exposure to humans through consumption. A better understanding of the NP-plant interactions and NP-transport is needed. Recently, enzymatic digestion and spICP-MS have been adopted in different studies to detect both the presence and translocation of NPs inside plants and/or between plants and the environment.

For example, the uptake and bioaccumulation of platinum NPs (PtNPs) [62] and cerium dioxide NPs (CeO$_2$ NPs) [63] were studied in different crops following NP exposure. The size distribution and particle concentrations of these two NPs were determined in different plant tissues. In addition, the authors also determined the presence and concentrations of their dissolved

counterparts. Both results suggested that all tested plant species were capable of the uptake of intact NPs, but the level of bioaccumulation was observed to be species dependent. PtNPs displayed high stability considering the lack of dissolved platinum signals, while cerium was observed in both the particulate and dissolved forms. The speciation observed for the CeO_2 NPs in plant tissues indicates further investigation is needed to fully understand the behavior of NPs in biological matrices. Another area of interest in the NPs-plant interaction are physiological responses of plants to NP exposure. It has been shown in the literature that smaller sized NPs displayed greater distribution in tissues without significant effect on growth and/or morphology.[61] Li *et al.* reported that both the accumulation and phytotoxicity of AgNPs were dependent on the exposure pathways while the NPs size distribution was independent of exposure pathway.[64] Regardless of the exposure route, AgNPs can be translocated through different plant tissues, indicating the need for risk assessment.

In addition to NP transport occurring within individual plants, NP transfer from these organisms into the environment has been observed as well. Plant to the environment NP transfer is exemplified from a study where the leaves from three edible vegetable were rinsed with water and the washes were tested for the presence of CuNPs.[60] The results of the study showed the presence of CuNPs at a ppb level in wash-water; however, most of the NPs were retained in vegetable leaves. Furthermore, Cu-bearing particle detection and size distribution analysis has been performed in foliar wash-off suspensions from wine leaves using SP-ICP-MS.[65] The analysis showed the copper was bound to smaller sized organo-mineral NPs (25-152 nm) and were contained wash-off samples. These studies provided valuable information on the possible human-NP exposure from foods.

3.3 Nanoparticle-animal interactions and spICP-MS analysis

Nano-titanium dioxide NPs (TiO_2-NPs), which are widely used and commercially available, have been known to cause intestinal and systemic immune system impairment in rats.[66] However, the effect of TiO_2-NPs on humans remains unknown. Disturbingly, TiO_2-NPs are one of the most used NPs in consumer products. A study was performed to quantify the total titanium concentration and the number of TiO_2-NPs in 15 post-mortem human livers and spleens. The study determined that 24% of titanium particles within these tissues were of sizes smaller than 100nm. Furthermore, half of the administered dosages had concentrations associated with liver damage.[56] Research has been performed in arthroplasty, which includes a specific case study of failed hip replacements with a tantalum (Ta) alloy prosthetic. spICP-MS analysis was implemented to identify the presence of NPs containing Ta, Zr, Co, Cr, Mo, Ti, Al, and V in periprosthetic tissue, bone marrow, and synovial fluid. While Ta and Zr NPs were determined to be stable against oxidation, it was shown that Co, Cr, Mo, Ti, Al, and V based NPs were prone to dissolution.[67] Although the effects of NPs in human health are currently unknown, determining the ability of NPs to accumulate and/or transform in specific organisms is crucial to understanding the impacts of NPs on humans.

Another case study investigating simulation of *in vitro* human digestion of chicken meat exposed to AgNPs has been performed. In the study, it was observed that successive size and dispersion transformations of AgNPs occurred during salivary, gastric, and intestinal digestions, which resulted from shifts in temperature, pH, variable enzymatic concentrations, and salt concentrations.[68]

Although not all health impacts of NPs on humans are known, the use of silver NPs has been reported to cause forms of toxicity in many living organisms. The presence of AgNPs in rat liver cells resulted in a significant depletion in mitochondrial function and an increase in the levels of

reactive oxygen species, which are potentially caused by oxidative stress [69]. Extensive work has been and is being performed to evaluate the presence of AgNPs in biological systems with the aid of spICP-MS. It has been shown that NP uptake in biological tissues can be greatly affected by surface coating; therefore, tissue permeability of certain surface coatings has been heavily researched. For AgNPs, changes in the overall size and/or surface charge resulting from coating the NPs with either polyethylene glycol (PEG), sodium carboxylate (COONa), citrate, bovine serum albumin (BSA), chitosan, or polyvinylpyrrolidone (PVP) surface coatings have been investigated.[12,54,55,58] To minimize confounding variables, (eco)toxicological effects also need to be considered to determine the stability and permeability of NPs to distinct biological tissues. Malysheva et al. has reported on the differences in AgNPs sorption to reaction vessels, plastic containers, for algal growth inhibition and mammalian cell toxicological assays. Up to 97% of AgNPs were sorbed on the reaction vessel for the algal growth assay, while only 15% were lost to vessel sorption in the mammalian cell assay. This vast difference in NP sorption was proposed to have occurred due to the high concentration of protein and biomolecules in mammalian cells leading to NP steric stabilization.[70]

Current NP dose and response research has focused on model systems investigating edible animal meat and human tissues/organs to observe the physiological response to NPs. Nanoparticle exposure to living organisms from the environment can occur through direct contact, maternal-fetal transfer, or trophic transfer. Gallocchio *et al.* evaluated the effects of oral administration of PVP coated AgNPs in hens. The authors determined that AgNP accumulation occurred in the liver and yolks but was not present in other tissues.[55] When evaluating the applications of PEG and sodium acetate coated AgNPs (27 and 34nm, respectively) in an *ex vivo* human placenta perfusion model, it was concluded that PEG coated NPs translocated more readily, while sodium acetate

coated NPs experienced greater clustering.[48] The results for the study intensify the debate to whether the accumulation is caused by the initial AgNPs or through secondary NP formation.

As previously mentioned, NPs can persist in soil leading to direct exposure to organisms living in soils, such as worms. The evaluation of the effects of positive, negative, and neutrally coated AgNPs to earthworm exposure showed BSA coated NPs were absorbed more readily by these organisms. Although all AgNPs at sufficiently high concentrations, regardless of coating, were shown to impair earthworm reproduction, BSA coated particles were the most toxic.[58] The data suggests that metal-based NP properties can be altered by surface coating and further change the animal response to the NPs.

Although there have been many advancements in the utilization of spICP-MS in biological applications, certain limitations still need to be addressed. For example, it is still not well understood whether NPs cross cellular membranes or if the detected concentrations come from precipitated ions. Further examples include NP agglomeration in biological tissues as well as the formation of protein coronas, which may influence size distribution leading to an overestimation of NP size. However, the use of separation techniques such as hydrodynamic chromatography (HDC) can determine whether dissolution, agglomeration, or formation of protein coronas occurs.[71] But, HDC requires careful sample dilution and has been shown to have an upper limit on size detection.[72] Compared to conventional instrumentation, abundant information can be acquired from spICP-MS yet a relatively large fraction of small sized NPs are undetected in the instrument.[54] To address the issue of only partial-particle detections, sensitivity to smaller sized NPs (<10nm) must be further optimized. In addition to sensitivity issues, there is a lack of multiple standard reference materials to perform proper size calibrations and transport efficiencies, which can cause reliability and application problems. Other suitable techniques to validate spICP-MS analysis in

biological media, including electron microscopy, do exist and create a need for interlaboratory collaborations. It is imperative to develop consistent NP detection and characterization techniques in biological media to expand the understanding of the human health and environmental impacts of NPs.

4   Innovations and advancements in spICP-MS

Many innovations and advancements in the field of spICP-MS have more recently been through the coupling of spICP-MS to other techniques such as capillary electrophoresis (CE), electrospray-differential mobility analysis (ES-DMA), asymmetric flow field flow fractionation (AF4), flow injection (FI), isotope dilution, laser desorption and ablation, and time-of-flight (TOF).[73–78] The advances in instrumental methods have occurred through techniques such as elemental droplet evaporation, circumventing spectral interferences, adjusting temporal resolution, sensitivity drift correction, isotope dilution, and total consumption methods.[79–83]

4.1 Capillary electrophoresis – spICP-MS

Hybridization of separation techniques with spICP-MS has been shown to increase selectivity and improve the quality of size analyses. Mozhayeva *et al.* preconcentrated AgNPs through capillary electrophoresis to successfully separate a mixture of 20, 40, and 60 nm AgNPs. After optimization of the CE system, the researchers observed that sensitivity increased 14 times, 21 times, and 28 times for 20 nm AgNPs, 40 nm AgNPs, and 60nm AgNPs, respectively. The authors found that a 3 second preconcentration mode was appropriate following an injection time of 110 seconds. The study also showed the ability to separate mixtures of the three NPs with a broad concentration range. The separated NP peaks were fully resolved from both the background and between each nanoparticle size. Unfortunately, coupling CE to spICP-MS did increase the

background for Ag due to the organic matrix; however, the method was able to separate 20 nm AgNPs from the background signal.[73]

4.2 Electrospray – Differential Mobility Analysis – spICP-MS

Another novel form of hybridization involves coupling electrospray-differential mobility analysis (ES-DMA) to spICP-MS. Tan *et al.* used ES-DMA as a technique for size discrimination by exploiting the differential mobility of NPs. Furthermore, DMA can separate NPs from ionic species, which can improve the background signal observed in environmental samples. Tan *et al.* used NIST 30 and 60 nm (RM 8012 and RM 8013) AuNPs and commercial 40, 80, and 100 nm AuNP suspensions. NP sizes were validated through mobility measurements using electrospray differential mobility coupled to a condensation particle counter. The technique was able to successfully separate a mixture of the five different sized AuNPs. ES-DMA-spICP-MS was also shown to be able to separate aggregates of 40 nm NPs for analysis that had formed over a nine-day period. The separation of the NP aggregates showed the technique was able to monitor the degree of NP aggregation temporally.[74]

4.3 Field Flow Fractionation – spICP-MS

One of the more popular separation techniques hybridized to spICP-MS is field flow fractionation. Field flow fractionation is a separation technique wherein the sample is introduced into a channel and subjected to a laminar flow. The laminar flow is applied along the length of the channel and the separation field is applied perpendicular to the channel. The application of the separation field forces particles or molecules toward the channel bottom separating them by their mobilities, which is dependent on the applied field (such as flow, electrophoretic, or magnetic). In flow FFF, larger particles are forced to the bottom of the channel more quickly and easier than smaller particles due to their size. The cross flow enters from a membrane located at the top of the

channel and exits through a semi-permeable membrane on the accumulation (bottom) side of the channel. The AF4 system is like the FFF, but the AF4 system only has one semi-permeable membrane located on the accumulation side of the channel. The separation field is formed when the carrier liquid exits through the semi-permeable membrane.

AF4-spICP-MS methodology is continuously changed to produce results that are representative of the sample used. However, some researchers have pointed out the effect of capping agents on NPs is often not considered in the analysis. Lee *et al.* attempted to correct the gap in knowledge analyzing two types of silver nanoparticles (AgNPs), polyvinylpyrrolidone-coated (PVP-) and citrate-coated, in three sizes, 30, 60, and 100 nm. In addition, the authors investigated the use of the three carrier liquids in the AF4 system, which were deionized water (DW), inorganic salt solutions (NaCl and $NaNO_3$) and a surfactant solution containing FL-70. The study showed that DW had near 100% recovery after AF4 analysis, while the surfactant solution had the lowest recovery of >80% but was still relatively high. Fractions obtained from the analysis were analyzed offline using spICP-MS. The spICP-MS analysis showed that PVP coated 30 nm nanoparticles had good separation in all carrier liquids; however, the separation of the 60 nm PVP-AgNPs was dependent on the carrier liquid. Similar results were observed for citric acid coated NPs. The 1.0 mM $NaNO_3$ solutions and distilled water carrier liquids were shown to be the most suitable carrier liquids. In addition, the distribution of NPs was observed to change between the carrier liquids due to poor resolution of the particles and co-existence of 30 nm particles with the 60 nm particles. The authors showed that online detectors including UV-Vis and multi-angle light scattering (MALS) were unable to resolve the separation of the 30 and 60 nm sized NPs; whereas, spICP-MS was able to detect their coexistence.[75]

Offline analysis of samples is useful especially after FFF pre-concentration; however, online coupling can further increase sample throughput and analysis. Hetzer *et al.* used online coupling of AF4 to a spICP-MS to detect release of AgNPs from food packaging films. The results of the study showed that online coupling had two beneficial effects on the analysis of AgNPs, namely, the reduction of the ionic background in the sample and the concentration of NPs in the sample. These benefits provided an improved sensitivity that increases the size characterization capabilities of spICP-MS. The study used three food simulants to determine AgNP leaching, which included 3% acetic acid, ultrapure water, and 10% ethanol. These simulants were stored in food packaging impregnated with AgNPs at elevated temperatures for 10 days to mimic long term storage. AF4 successfully used to reduce the amount of ionic silver fraction in the samples and reducing the background counts from 12,000 cps or higher to 200-600 cps. Without the reduction in silver ionic background, smaller NPs in the size range of 18 to 22 nm would have been lost in the background and not detected. However, the cross-flow of the AF4 channel has been shown to induce NP agglomeration as the NPs are pressed against each other and the membrane along the lower channel wall.[84]

4.4 Application of collision/reaction cells to spICP-MS

Single particle mode in ICP-MS can successfully be used with triple quadrupole mass spectrometers. Candas-Zapico *et al.* analyzed titanium dioxide NPs under various measuring modes including single quadrupole mode with a collision/reaction cell system as well as in a triple quadrupole mode. Helium, ammonia, and oxygen were used as reaction gasses in the collision cell, which enabled the researchers to measure 26 nm TiO_2 particles in triple quadrupole mode with a dwell time of 10 milliseconds. The purpose of the research was to explore the influence of cell reaction gases for the removal of isobaric interferences. Due to the isobaric interference of

^{48}Ca with the most abundant isotope of titanium, ^{48}Ti, ^{47}Ti is often the isotope used in ICP-MS studies. The reduction of isobaric interferences for the ^{47}Ti isotope can be achieved using oxygen in the reaction cell, which forms a ^{47}Ti^{16}O$^+$ species. The ^{47}Ti^{16}O$^+$ species reduces interferences such as ^{35}Cl^{12}C$^+$ or ^{15}N^{16}O$_2{}^+$, which are formed in the plasma. Triple quadrupole ICP-MS can measure titanium after a collision event by focusing on the mass of the ^{47}Ti^{16}O$^+$ or 63 amu. The same process can also be applied to titanium and ammonia products. The authors analyzed chewing gum for the presence of TiO$_2$ NPs using a simple water extraction to show the utility of the collision cell in spICP-MS analyses. The results showed a broad size range for E171 TiO$_2$ NPs from 30 nm to 200nm with approximately 40% of particles smaller than 100nm.[85]

4.5 Laser Desorption Coupled spICP-MS

Laser desorption methods can also be used to complement SP-ICP-MS instrumentation. Benesova *et al.* used substrate-assisted laser desorption (SALD) to directly introduce samples into a spICP-MS circumventing the standard nebulization. Using a Nd:YAG laser as an energy source, gold nanoparticles were liberated from an absorbing plastic surface. The authors observed that by varying laser power, scan rate, and the carrier gas flow rate, disintegration of the AuNP can be avoided and satisfactory transport efficiency can be achieved. Using 56 nm gold nanoparticles, a transport efficiency of 61% was achieved, which is lower than a typical aerosol transport efficiency of 80%. However, this transport efficiency was much higher than what is normally observed for nebulization. The study also showed the size distribution of the NPs analyzed was approximately 56 nm and most particles remained intact after desorption. Laser desorption, while not suitable for aqueous samples, can be capable of analyzing solid samples with embedded NPs such as plastic packaging, food containers, or textiles.[78]

4.6 Flow Injection Coupled spICP-MS

Flow injection coupled to spICP-MS may provide a powerful method that maintains detection limits while employing a simple introduction method. Injecting a known volume into an instrument eliminates the need to measure the sample flow rate. Therefore, the number of NPs that enter the nebulizer is the nanoparticle concentration multiplied by the known injection volume. However, the transport efficiency of NPs has been shown to remain the same at approximately 5% for both flow injection and direct nebulization techniques. The mean particle size determined using each injection technique for a 60nm reference standard of AuNPs was shown to be approximately 62 nm under direct nebulization and approximately 60 nm with flow injection. The result of the study indicated that flow injection increases the dispersion of the sample before nebulization allowing for higher resolution and lower coincidence of particles at the detector. As a consequence of the higher dispersion, the recovery of the sample was $90.7 \pm 5.0\%$ for flow injection as opposed to $83.5 \pm 1.5\%$ for conventional sample introduction, although not statistically significantly different.[77]

4.7 Application of a total consumption introduction system

The ability to remove the uncertainty introduced by the transport efficiency of NPs into the plasma from the sample is highly desired in spICP-MS analysis. To reduce the transport efficiency uncertainty, a total consumption sample introduction system can be used. Miyashita *et al.* designed a total consumption introduction system that has a potential transport efficiency of 100%. The system thus eliminates the errors in analysis introduced by loss of sample observed using conventional nebulization. The authors used a setup that allowed for continuous nebulization of a sample, from which a transport efficiency of 93% was achieved for platinum NPs with a size of 70 nm with good reproducibility.

4.8 Time Of Flight spICP-MS

One disadvantage of spICP-MS is the inability to measure multiple elements simultaneously. Sequential detection of elements is possible but requires the quadrupole to switch between masses, which requires time. Subsequently, NPs consisting of heterogenous compositions or coatings cannot have all elements analyzed simultaneously. These shortcomings can be overcome using time-of-flight (TOF) technologies. Naasz *et al.* analyzed steel, $(Bi_{0.5}Na_{0.5})TiO_3$, and $BiVO_4$ NPs that are primarily used in industrial applications using both spICP-MS with a quadrupole mass analyzer and a spICP-TOFMS system with a time-of-flight mass analyzer.[76] The authors noted that in TOF the ions from the particles enter a field-free-region where separation occurs according to the velocity of ions, which is dictated by the mass. Whereas a quadrupole mass analyzer utilizes oscillating electric fields to separate ions traveling between four electrodes. Particle size calculated by each instrument was comparable; however, the spICP-TOFMS could detect smaller diameter particles than the quadrupole spICP-MS. In addition, the ability of the spICP-TOFMS to analyze a full mass spectrum simultaneously determined the composition of each NP highlighting the multi-element capacity of the instrument. Improvements to multi-elemental detection on quadrupole equipped instruments are possible by reducing the settling time. However, results are semi-quantitative due to the requirement of switching from one mass to another and signal loss during mass switching.

5   Conclusion

The versatility of ENMs allows for a multitude of applications in consumer and industrial products. The purposeful application as well as incorporation of ENPs into different products will be a trend that will not only continue but will increase in both the near and distant future. The

characteristics and possible transformations of NPs make assessing their effects on the environment and human health a difficult task. The ability to accurately monitor the presence, migration, and transformation of nanomaterials in environmental systems strengthens the possibility for predicting the effects posed by these materials. In addition, monitoring the size distribution of NPs over time indicates NP stability and physicochemical state expressed by the materials in that media. The overall stability and transformations of these materials will dictate the toxicity associated with their use. The high throughput and sensitivity of spICP-MS analysis provides for a detection and characterization method capable of studying ENMs and NNPs in an efficient time frame and in an unaltered state.

CHAPTER II

TARGETING METAL IMPURITIES FOR THE DETECTION AND QUANTIFICATION OF CARBON BLACK PARTICLES IN WATER VIA spICP-MS[2]

Introduction:

Carbon black (CB) is the longest established commercial form of carbon nanomaterial currently on the market. It is one of the most inexpensive available nanocarbon products with a price of approximately 1 US dollar/kg, with a projected annual production of 15 Mt by the year 2025.[86] When compared to the price of other nanocarbon sources such as graphene nanoplatelets ($450/kg)[87], carbon nanotubes ($700/kg)[88], and C60 fullerenes ($95,000/kg)[89], it is evident why the market for CB is rapidly expanding. As the application and uses of this material continue to increase, including those intended for water treatment[90] and renewable energy[91,92], so will the need for a detection method capable of measuring CB release from engineering devices imbedded with this material.

The largest application for CB is as a reinforcing agent in tires and rubbers in the automotive industry.[93] In addition, many other consumer products incorporate this carbon material in their production as an additive including inks, paints, coatings, and plastics.[93] The high demand for CB ranks it as one of the top 50 industrial chemicals manufactured in the world.[94] The continued research on the properties and structure of this nanomaterial has led to its use in renewable energy [91,92] and environmental remediation applications.[86] The electrically conductive

---

[2] Reprinted from K. Flores, L. Rand, C. Valdes, A. Castillo, J. Cantu, J. Parsons, P. Westerhoff, J. Gardea (2022) Targeting Metal Impurities for the Detection and Quantification of Carbon Black Particles in Water via spICP-MS. *Environmental Science & Technology*, 56, ©2022 American Chemical Society. All rights reserved.

nature of CB has led to its incorporation into anodic and cathodic materials for fuel cells and batteries [91,92], while the thermally conductive nature is reason for CB's implementation into water treatment technologies including nanophotonic enhanced solar membrane distillation.[90]

CB exists as aggregates of primary particles of spherical shape ranging between 10 and 100 nm in diameter. The primary particle consists of an amorphous (turbostratic) graphitic core surrounded by graphene sublayers forming a disordered onion-like nano structure referred to as the basic structural unit.[95] These are bound to other basic structural units to form CB aggregates, which may only be separated through structural fracturing. CB is formed through a thermal controlled decomposition in an inert or oxygen deficient atmosphere.[86] Currently there is a large variety of synthesis methods to tailor properties for specific applications for the utilization of these materials. Like other nano and micron sized graphitic materials CB has been known to contain metal impurities within its structure which may give rise to specific properties but the extent and variety of these impurities is poorly understood.[96] CB particles have been reported to contain trace metals (Cu, Fe, Mn, Mo, Ni, V) present in concentrations of mg of metal per kg of CB.[97] While potential health concerns related to metals in CB have been raised, these metal impurities may be useful for the purpose of analytical detection.

Utilizing these metals as tracers could provide a viable route for detection and quantification of CB particles in water, considering that currently available quantification methods targeting the bulk (carbon) portion of graphitic materials are severely lacking in many key aspects.[98] For CB and related graphitic materials, thermal gravimetric analysis and thermal optical transmittance require concentrated samples (10-100 mg/L), which would not be suitable for environmental detection. Total organic carbon analysis and Raman spectroscopy can handle lower concentrations (0.1-1.0 mg/L), but the non-specific nature of these methods leave them highly

susceptible to inferences from other carbon sources common in environmental samples.[1] Finally, microscopy techniques are considered powerful tools for characterization of graphitic particles, but these methods are unsuited for high throughput quantification due to the necessary time for particle counting and complex sample preparation.[96] Based on these considerations, the need for a sensitive, robust, and high throughput analysis of CB particles, and related materials, in environmental waters is of high priority.

Single particle inductively coupled plasma-mass spectrometry (spICP-MS) is a highly sensitive technique for nanoparticle (NP) detection, quantification, and sizing. Extremely fast acquisition times (10,000 scans/s) allows for counting of particle number concentrations in an aqueous sample ($\frac{number\ of\ particles\ detected}{mL\ of\ sample}$) and sizing based on pulses generated from the ionization of particles.[99] The rapid analysis time can provide high throughput analysis capable of accurate determination of particle sizes and number concentrations in minutes. Detection limits for most metals are low ng/L concentrations, which may allow for a detection method based on impurities present at extremely low mass fractions in a material, as has been shown for carbon nanotubes.[100–103] In this work, spICP-MS was evaluated for CB particle quantification based on detection of trace La after a full characterization of the metal compositions of commercially available CB materials. We show successful validation of this technique based on a highly reproducible and strong linear relationship between counts of La-containing particles and CB mass concentrations in the Monarch 1000 (M1000) CB variety. The quantification accuracy of this method was compared with gravimetric analysis and UV-visible spectrophotometry. Additionally, the sensitivity and detection limit remain unchanged when CB M1000 particle suspensions were spiked with dissolved La, at environmentally relevant concentrations. This method should be well

suited for quantification and detection in future release monitoring studies on developing CB-containing materials and applications.

Methodology:

2.1 Digestion and ICP-MS Analysis of NIST SRM 1635a & Commercial Carbon Black Materials

Digestions of a standard reference material (SRM) for trace elements in coal (NIST 1635a) were carried out alongside CB for the purposes of method validation. For an accurate determination of mass when calculating the mg of impurity present per kg of carbon material, all CB samples and SRMs were dehydrated to remove moisture. This was accomplished by placing a one gram sample within a clean crucible with a predetermined dry mass. The sample was heated to a temperature of 110°C for 1 hour then weighed within 2 min of removing from the oven. The dry mass percentages of the NIST SRM's as well as the commercial CB materials are provided in Table S3 of the supplementary information (SI).

A minimum mass of 250 mg was utilized as suggested by the NIST certificate for SRM 1635a and commercial CB materials to ensure reproducibility. For both the SRM and CB materials digestions and analysis were conducted in nine-replicate sets to establish a reliable estimation of these concentrations of metal impurities. The mass was placed within a perfluoroalkoxy microwave digestion vessel (75 ml capacity) which was then filled with 40 ml of 70% plasma pure trace metal grade HNO_3 (SCP Science) then sealed with a stopper and screw cap. Samples were then digested in a CEM Mars 5 digestion microwave system in a three-step method: 10 min at 400 W, 25 min at 800 W, and 25 min at 1200 W. Following this method, the remaining solutions were clear in appearance indicating that the carbon-based material was oxidized and dissolved, and complete digestion had occurred. The digestate was placed into 50 mL acid resistant tubes (digitubes - SCP Science) diluted with additional 70% plasma pure HNO_3 to reach a final volume

of 20 ml and stored for later analysis. For the ICP-MS analysis of metal impurities, aliquots of 0.2 ml of the digestate were diluted with MilliQ water (18.2 Ω) to a final volume of 10 mL, resulting in a 50x dilution. For cleaning purposes, the digestion vessels were soaked overnight in a 10% HNO_3 bath, cleaned with laboratory grade soap and deionized water, then rinsed thoroughly with MilliQ water (18.2 Ω).

Quantification of 18 metals (listed in Table S4) was determined with a Perkin Elmer NexION 1000 ICP-MS with an S10 autosampler. The instrument was fitted with a glass concentric type C nebulizer, glass cyclonic C3 high sensitivity spray chamber with matrix gas port, and a one-piece 2.5 mm I.D. injector quartz torch. For the peristatic pump, 0.51 mm PVC pure tubing was used. Ultra-High Purity Argon Gas (>99.998%) was utilized as the source for the plasma generation. Typical instrument operating parameters and criteria for the daily standard performance check are provided in Tables S1 and S2 of the SI. All element calibrations were performed using high purity standards obtained from Sigma Aldrich. Calculations to determine SRM and CB metal mass fractions and recoveries are detailed in section S2 of the SI.

2.2 Single Particle ICP-MS Analysis of Carbon Black Suspensions

Stock suspensions of CB were prepared by placing 100 mg of the Monarch 1000 CB variety into 368 mL of milliQ water in a 1 L Erlenmeyer flask, mixed by swirling and then by bath sonication for 10 min. To improve CB suspension stability and reduce sorption to container surfaces, 32 mL of Triton X-100 (TX-100) nonionic surfactant was then added. The solution was then placed on a sample shaker (Revco) for a period of 15 min at a speed of 130 RPM. The resulting solutions were of a concentration of 250 mg/L CB and 8% by volume TX-100. This stock solution was then diluted with milli-Q water. In order to maintain a constant matrix of TX-100 across the range of CB concentrations analyzed, TX-100 was added from a 5% stock during dilutions.

Because early work indicated high likelihood of sorption of CB to the instrument's sample uptake system, all spICP-MS analysis was conducted via manual sample introduction to reduce the tubing length and potential particle loss. This was accomplished by introducing sample from just ahead of the peristatic pump, instead of the autosampler probe. Additionally, the introduction system was flushed for 1 min with pure milli-Q water between replicates. The sample flow rate was measured daily and ranged between 0.25 and 0.3 mL/min. Time-resolved data collection and processing was performed using the Perkin Elmer Syngtistix Nano application with a dwell time of 100 µs and a scan time of 180 s for TX-100 optimization studies, and a scan time of 420 s was used to maximize peak counting for the creation of the CB calibration curves (La instrumental response vs CB concentration). Dissolved analyte and transport efficiency (TE) calibrations were performed daily using dissolved Au and La standards at 1, 5, 10, and 20 µg/L (Sigma Aldrich) and a 500 ng/L 60 nm Au-citrate nanosphere standard (Nanocomposix). Transport efficiency (TE) was determined using the particle size method described by Pace et al.[99] The initial threshold used to separate particle events from background signal was calculated by the Syngistix software using a 3σ algorithm. Sample data was then reprocessed after adjusting the threshold to a higher value to reflect a more conservative size detection limit (discussed further in SI section S6). Statistical tests (non-parametric ANOVA and Dunn's Test) to compare size distributions were carried out in R Studio. All graphing was performed in OriginPro 2021.

Results and Discussion

3.1 Metal profiles of six commercial carbon black materials

The metal profiles of six commercially available CB materials (Emperor 2000, Emperor 1800, Monarch 1000, Monarch 800, Monarch 120, and Vulcan XC72R) were established by ICP-

MS analysis following a HNO₃ microwave assisted digestion. The purpose of generating these metal profiles was to fully characterize their composition and investigate possible metal tracers that could be utilized in a single particle ICP-MS (spICP-MS) approach for detection of CB particles in water. Figure 2.1 shows the metal profiles established for the six commercially available CB materials, divided into CBs with high and low metal contents (upper and lower panels, respectively). Emperor 1800 contained the highest concentration of Ni (1.85 mg/kg), while the Vulcan XC-72R variety was identified to contain the greatest concentration of Cr (1.50 mg/kg). Finally, the Monarch 1000 CB variety was the most notable for Pb (0.433 mg/kg) content from the six aforementioned varieties. Although present in CB, these metals were observed at extremely low mass fractions in comparison to the concentrations of other metals identified as possible tracers.
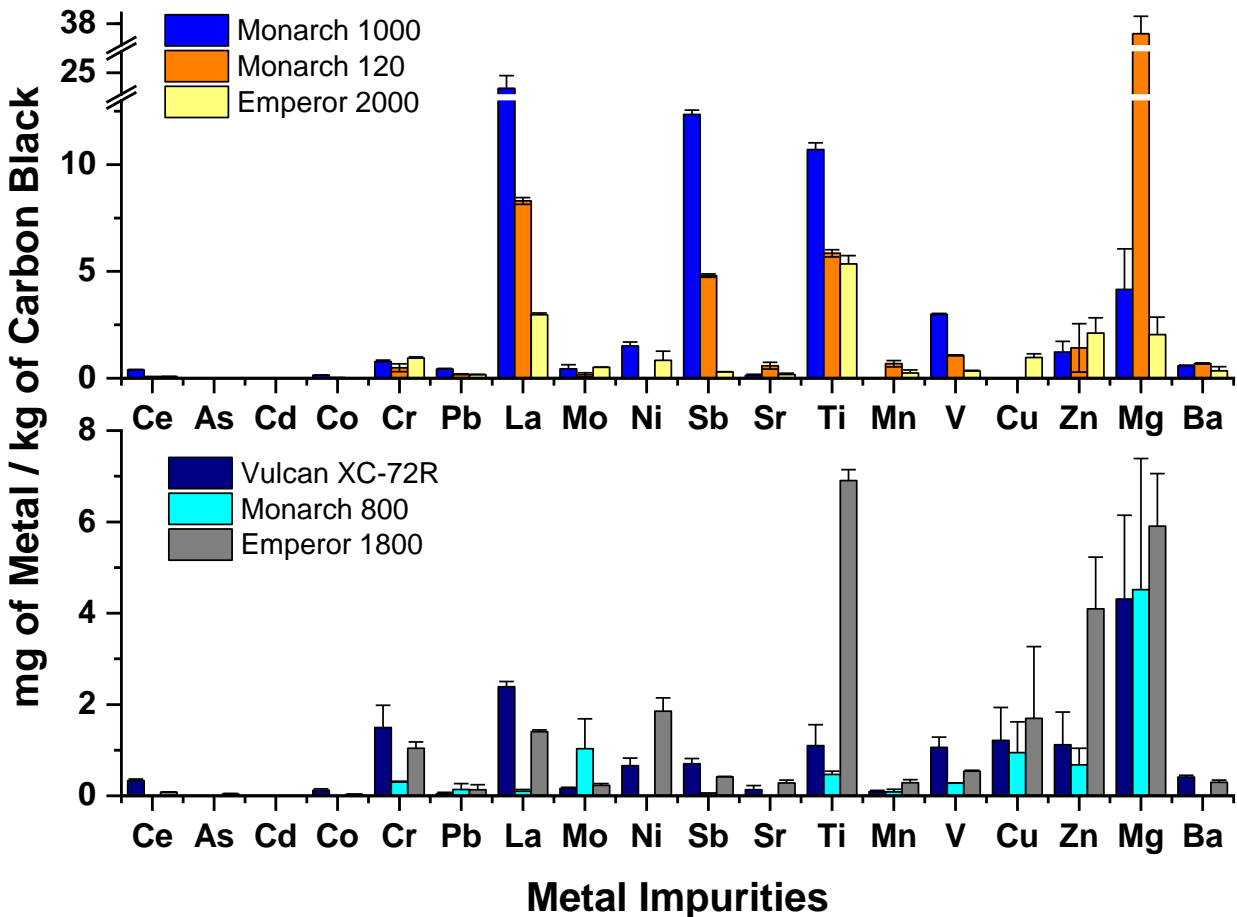
Figure 2.1: Profile of metal impurities for high metal content CB varieties (top) and low metal content CB varities (bottom).

The metals that were present in high enough concentration to be considered for use as a tracer in SP analysis included Mg, La, Sb, and Ti. Of these metals, La was chosen due to its lack of interferences and its low detection limits for mass spectrometry.[104,105] In addition, the low natural abundance of this rare earth element suggests low likelihood of dissolved La background existing in waters used in CB-containing water treatment technology. One developing application of CB materials is solar desalination technologies and the low abundance of La in seawater (3.4 x10^{-3} μg/L) supports the use of La as an appropriate metal tracer in that context.[90,106] Conversely, Mg is ubiquitously present at appreciable concentrations (>10 mg/L) in many types of water sources, which would limit its use in spICP-MS detection of CB particles.[107] Ti occurs in water

between concentrations of 1-10 µg/L and suffers from a variety of polyatomic interferences, which results in larger particle size detection limits (>65 nm) for single particle analysis on standard quadrupole ICP-MS instruments.[108] Sb is only known to suffer from one polyatomic interference, $^{94}Zr^{16}O_2$, but this element was found to be present in CB at half the concentration of La.

3.2 Optimization of the single particle inductively coupled plasma-mass spectrometry method for carbon black detection

Based on the metal profiles and the selection process discussed above, La was identified as a suitable tracer for spICP-MS detection. Since the M1000 CB material contained the highest mass concentration (mg/kg) of La, this variety of CB was chosen to develop the spICP-MS method utilizing metal tracers for the detection of CB particles. Considering that spICP-MS determines particle concentrations and sizes on a particle-by-particle basis, results are most accurate when enough detectable NPs are present for well-developed size distributions and good counting statistics. Therefore, method development efforts focused on establishing a limit of detection and maximizing particle counting. First, a calibration curve was established from known quantities of M1000 CB material and these concentrations were correlated to the observed La signal. This relationship can then be used to determine unknown CB concentrations based on the measured number of particles containing the metal impurity. As seen in Figure 2.1 all commercial CB materials contained La but the concentration varied greatly between these varieties. Consequently, the method sensitivity is expected to depend heavily on this ratio of metal to carbon mass and known relations should be established to set capabilities for this proposed method.

Figure 2.2 shows the time resolved La analysis of M1000 CB suspensions. The number of peaks in an analysis window is directly related to concentration of La-containing particles in a solution, while the peak area is proportionally related to the mass of La in the associated CB

particle.[99] In preliminary analysis, particles were "sticking" or adhering onto the ICP-MS sample uptake system (probe, tubing, nebulizer, and spray chamber), which greatly reduced the sensitivity of the proposed method. After screening several potential dispersing agents, the adhesion issue was resolved with the addition of a nonionic surfactant Triton X-100 (TX-100). The addition of TX-100 was found to reduce CB sorption to surfaces as well improve the stability of CB suspensions, with no observable impact to the background. The use of TX-100 for spICP-MS analysis has been reported in literature to increase dispersion and reduce agglomeration of nanoparticles in solution[109,110], resulting in better suspension stability. Initial trials including TX-100 were conducted at a concentration of 0.05%, which significantly improved particle detection (Figure 2.2b).
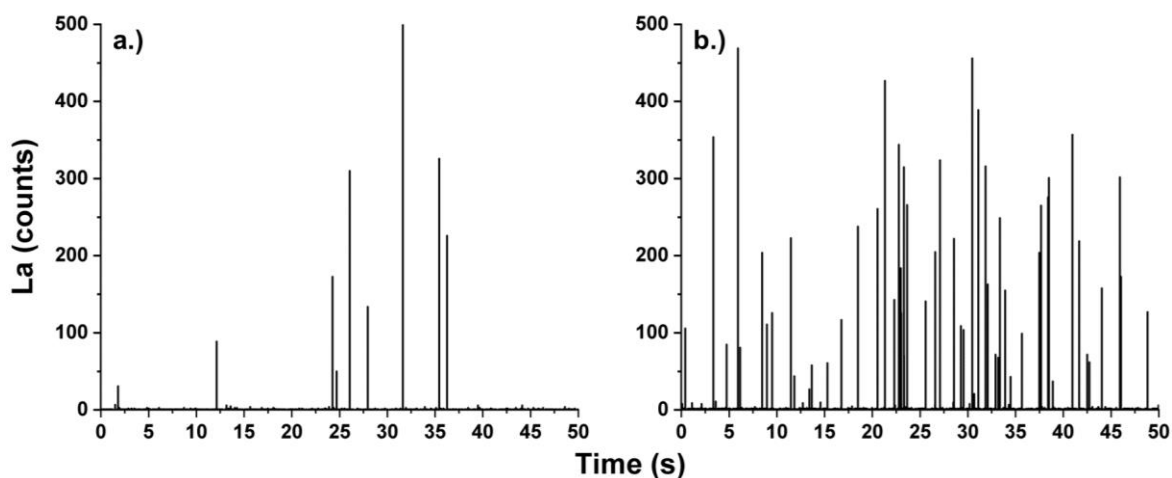
Figure 2.2: spICP-MS analysis of 2.5 mg/L of CB M1000 without surfactant (a) and the same concentration of CB with 0.05% of TX-100 surfactant (b).

The use of the surfactant helped increase and maintain consistent numbers of La-containing particles detected in the same concentration of CB. To ensure that the addition of TX-100 did not negatively impact the instrument sensitivity to La signal, the calibration standards of dissolved La and Au as well as particulate Au were prepared in matrices containing the same concentration of

TX-100, with no observed changes to the slope or y-intercept of the calibration curve obtained (Table S5 in the SI).

After confirming that the use of surfactant increased the observable particulate signal during spICP-MS analysis, experiments were carried out to determine the optimal concentration of surfactant in sample matrices. TX-100 concentrations of 0, 0.1, 0.15, 0.2, 0.3, 0.5, 0.75, and 1.0% by volume were examined in relation to total NP peaks in an analysis window. Figure 2.3 shows the influence of TX-100 concentration on number of La peaks detected by spICP-MS for three different CB concentrations. Separately, the impact of surfactant on NP/background threshold and minimum detectable CB size were examined. The observable number of La peaks in the controls were initially insignificant but did steadily increase with increasing concentration of TX-100 (SI Table S6). Therefore, blank subtractions were performed on all CB sample results in order to account for false positives generated by the surfactant.

Analytical measurements were conducted for every concentration of TX-100 stated above and were tested over three separate concentrations of CB particles: 1000, 500, 250 μg/L. Figure 2.3 indicates increasing La particle detections with addition of TX-100. The spICP-MS results of all three CB concentrations indicated that La peak counts were maximized in sample matrices containing 0.15% TX-100. At higher surfactant concentrations, a slight decrease in signal was observed, followed by no effect of increasing concentration. The standard deviation of samples also increased at higher concentrations of surfactant, suggesting a negative impact to the precision of analytical results. The 0.15% TX-100 sample matrix was therefore chosen as the optimal concentration of surfactant for all following experiments. Our TX-100 concentration selection for CB is similar to other studies that have utilized TX-100 to stabilize Ag and Pt metallic NPs for spICP-MS analysis, which reported 0.1% by volume as their optimum concentration.[111,112]
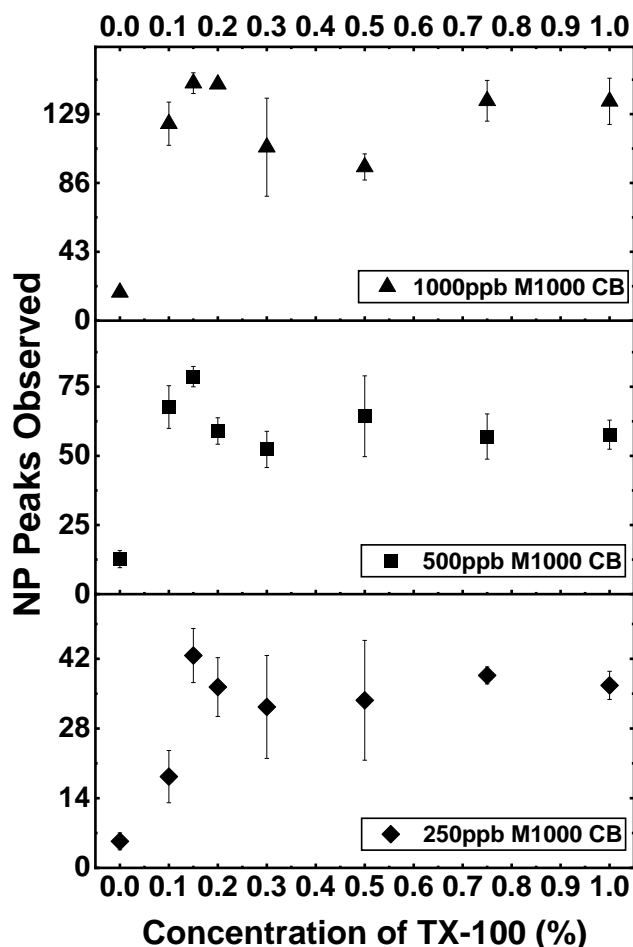
Figure 2.3: Optimization of surfactant TX-100 concentration suitable for spICP-MS analysis, based on the number La peaks measured after blank subtraction (determined by analysis of a matrix blank with identical TX-100 concentration). CB suspensions at three separate concentrations were examined: 1000 µg/L (top), 500 µg/L (middle), and 250 µg/L (bottom). In all three cases, maximum detection of La peaks was observed at 0.15% TX-100.

       After selecting the optimal TX-100 concentration, the threshold for separating particle

events from background was evaluated from analysis of matrix blanks. This value, which defines

the minimum La mass for a CB particle to be detected, is a critical consideration in spICP-MS

analysis. The threshold determination and corresponding particle size detection limit is discussed

extensively in section S6 of the SI. Calculating a particle diameter from the intensity of its La

signal would require assumptions as to the La mass fraction and density of these particles, which

are unknown and may even vary between particles within a sample. Therefore, while this subject is explored somewhat in the SI, further discussions of particle sizing in section 3.5 are presented in terms of particulate La mass rather than CB size in nm.

3.3 Single particle ICP-MS calibrations, detection limits, and robustness

In order to determine CB concentration from the La signal observed during single particle analysis, two separate calibration approaches were taken. The first calibration (C1) uses the number of La peak events in an analysis window versus CB concentration. The second (C2) utilizes the calculated number of La-containing particles per mL of sample analyzed versus CB concentration. Both of these calibrations are presented in Figure 2.4. C2 incorporates both the transport efficiency (TE) of the instrument (defined as percentage of NPs in the sample nebulized, ionized, and in turn detected)[99], as well as the number of La peaks counted to calculate the number of La containing particles per mL of solution. While the TE value was similar between analysis throughout the study, a small amount of daily variation (6 – 8%) was present due to slight differences in flow rates (0.28 – 0.32 ml/min), instrumental tuning parameters (nebulizer flow and torch alignment), and the conditions of the hardware (sampling and skimmer cone). Examining the calibration with and without TE incorporated into the particle counting allows the potential impact of day-to-day instrument performance to be considered.
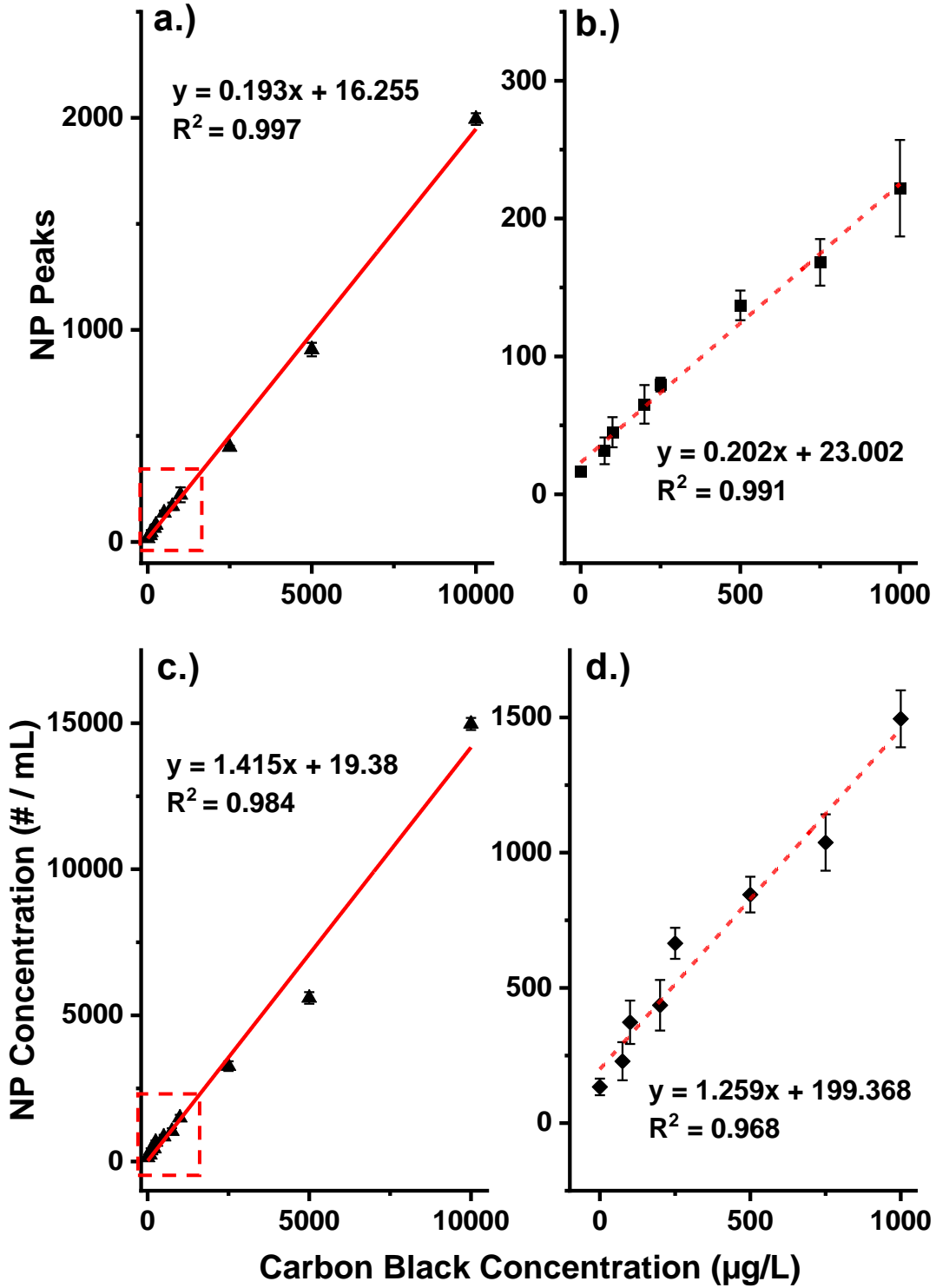
Figure 2.4: Complete calibration for NP peaks vs M1000 CB concentration (a), lower concentration focused calibration for NP peaks vs M1000 CB concentration (b), complete calibration for NP concentration vs M1000 CB concentration (c), lower concentration focused calibration for NP concentration vs M1000 CB concentration (d)

All CB concentrations were tested as the average of four replicate samples, except for the lowest concentration (75 µg/L) and the blank which were tested as the average of ten replicates. The separate calibrations are shown in Figure 2.4 with C1 being displayed in panels a and b, while C2 is displayed in panels c and d. The linear regressions in Figure 2.4a and c include the entire range of CB concentrations tested (75 – 10,000 µg/L), while Figures 2.4b and 4d include only the lower concentrations of the set (75 – 1,000 µg/L). As seen from the coefficient of determination (R^2), both approaches achieved excellent linearity over a wide range of concentrations. As expected, a slightly lower R^2 was generated for the C2 approach when compared to C1, due to the added variability of the TE. This was also the case for the linear regressions restricted to the lower CB concentrations as seen in panels c and d of Figure 2.4.

Both calibrations were statistically evaluated based on the limit of detection (LOD), defined as the lowest CB concentration which can be reliably distinguished from a blank, and the limit of quantification (LOQ), which refers to the lowest accurately measurable concentration of analyte that can be determined as a function of sensitivity[113]. These parameters were calculated by two different approaches: 1) the analytical response from a blank sample, which will be referred to as the Blank Determination (BD), and 2) the instrumental response from the calibration curves created by C1 and C2, subsequently referred to as the Linear Regression Determination (LRD). The equations used for each are provided below. The LOD and LOQ were given particular consideration given the potential impact of the surfactant on sensitivity.

In the BD approach (Equations 1-3), the mean and standard deviations of the blank was used to establish the limit of the blank (LOD_{blank}). The LOD_{BD}, or limit of the detection for CB particles based on the blank determination, was then calculated based on the LOD_{blank} and the standard deviation of the lowest CB concentration analyzed. The LOQ was then calculated by

the typical method, which is ten times the standard deviation of a blank added to the mean of the blank. The calculations for the LRD approach are provided in Equation 4 and 5, where SD_Y is the standard deviation of the y-intercept and *m* is the slope of the linear regression. The results of each approach are shown in Table 2.1, based on the calibration curves limited to the lower concentration range (75-1,000 µg/L, as shown in Figure 2.4c and d). The dynamic linear range (DLR) of the instrument, defined as the concentration range for which the analysis generates a linear response, spans from the LOQ to the highest concentrations which maintained a linear trend ($R^2 \geq 0.95$).

Blank Determination Approach[114]*:*

$$LOD_{blank} = mean_{blank} + 1.645(SD_{blank}) \qquad \text{Eq. 1}$$

$$LOD_{BD} = LOD_{blank} + 1.645(SD_{low \; concentration \; sample}) \qquad \text{Eq. 2}$$

$$LOQ_{BD} = mean_{blank} + 10(SD_{blank}) \qquad \text{Eq. 3}$$

Linear Regression Determination[113,115]*:*

$$LOD_{LRD} \; \frac{3.3*SD_Y}{m} \qquad \text{Eq. 4}$$

$$LOQ_{LRD} \; \frac{10*SD_Y}{m} \qquad \text{Eq. 5}$$

Table 2.1: LOD and LOQ values for the two separate correlations based on the limit of the blank and linear regression determinations. Dynamic linear range (DLR) refers to the concentrations greater than LOQ which maintained linearity. C1: Calibration using peak numbers. C2: Calibration using particle number concentrations.

	$C1_{BD}$	$C1_{LRD}$	$C2_{BD}$	$C2_{LRD}$
LOD (µg/L)	73.5	63.9	80.6	119.7
LOQ (µg/L)	122.2	193.7	192.3	362.7
DLR (µg/L)	122 - 10,000	194-10,000	192 – 10,000	363 – 10,000

Considering both the DLR and LOD, spICP-MS analysis using La as a tracer provides improved quantification capability compared to established techniques in the lower concentration ranges (0.1 – 10 mg/L). The $C1_{BD}$ approach established the largest DLR, from 122 to 10,000 µg/L of quantifiable concentrations for CB in water. The linearity of CB quantification by spICP-MS in this approach may be valid at concentrations greater than 10,000 µg/L, but this investigation was directed towards improving quantification capability at low concentrations relevant to water treatment samples. Several additional experiments (details in SI) were carried out to examine potential matrix effects and verify that the LOD and LOQ determined are valid when dissolved La is present at concentrations typical of natural waters (0.004 µg/L).[116] For CB calibration solutions containing dissolved La at this concentration, no adverse impact to CB detection was observed even at low CB concentrations (Figure S4).

Comparing the LOD of each approach, both $C1_{BD}$ (74 µg/L) and $C1_{LRD}$ (64 µg/L) were competitive for CB detection compared to pre-existing methods.[1] Common alternative techniques for detection of bulk graphitic materials (CNTs, graphene oxide, CB, etc.) in a simple water matrix are shown in Table 2.2 for comparison to spICP-MS. In addition to the methods in Table 2.2,

microscopy has been a very popular approach for characterizing nanocarbons, including CNTs and graphitic materials, but is impractical for quantification of CB particles in water. As further validation against existing quantitative techniques, a simple test on samples of unknown CB concentration were collected by passing concentrated suspensions (1000 mg/L) of M1000 CB through a Whatman P3 filter (pore size 6µm) in a Büchner funnel. The resulting filtrate was then analyzed via spICP-MS, gravimetric analysis, and UV-vis in order to quantify the amount of CB M1000 (details in section S4 of SI). This test was repeated three times and showed the spICP-MS determination of concentration to be in good agreement with the other techniques. The filtrate test was also repeated with major cations and anions typically present in drinking water sources included in the unknown sample matrix. The results from this analysis of CB in a simulated drinking water[117–119] also indicate minimal impact to the analysis (SI Figure S5). These method validations and the wide DLR combined with the high throughput capability of spICP-MS support that this technique will be advantageous to future studies on the detection of CB particles in water where release at µg/L concentrations is likely.

Table 2.2: Comparison of quantification capabilities of established techniques to the current method developed in this study.[1] TGA: Thermogravimetric analysis, AF4-MALS: Asymmetric flow field flow fractionation-multiangled light scattering, TOC: Total organic carbon, TGA-MS: Thermogravimetric analysis-mass spectrometry, AUC: analytical ultracentrifugation , TOT: Thermal optical transmittance.

Dynamic Linear Range (mg/L)	Quantification Techniques
10 – 100	TGA, A4-MALS, TOC
1 – 10	TGA-MS, Raman, UV-vis
0.1 – 1	AUC, TOT, TOC
0.1 – 10	Metal Impurity Tracing by spICP – MS (current study)

3.4 Particle size distributions from single particle analysis

In addition to developing and validating a method for quantifying CB concentrations based on trace La detection, the particle sizing capability of spICP-MS is an additional benefit. Simply calculating CB particle diameter from the peak area of each La pulse would require an assumed La mass percentage, density, and particle shape which may not be homogenous within the same CB sample. Rather than report inaccurate diameters calculated with assumed values, the CB particle size data are instead presented here in terms of the La mass detected in each CB particle. The calibrations presented in the previous sections support that CB concentration can be reliably quantified down to the parts-per-billion range based on the number of La peaks counted in single particle mode. It was additionally hypothesized that the size distributions generated from spICP-MS analysis would be consistent across the same DLR of CB concentrations tested.

Figure 2.5 shows the average particulate La masses, for all measured concentrations of M1000 CB, with corresponding descriptive statistics provided in Table S10 (see SI). At each CB concentration, the distribution of results (interquartile range, mean, median) was very similar, while the most frequent particle mass (mode) was nearly identical across the entire CB concentration range. These distribution properties, especially the mode, may be utilized to determine shifts from established values occurring from any background La-containing particles that may be present in environmental samples. This would be beneficial for natural water samples containing La rich minerals such as monazite and bastnasite.[106] The particle masses of each replicate at every concentration of CB were tested for statistical equivalence by performing a non-parametric Kruskal-Wallis ANOVA and post-hoc Dunn's Test of pairwise comparisons in R Studio (details in SI section S6). For every CB concentration, all replicates were found to be statistically equivalent to each other at the 95% significance level. This suggests a high degree of

reproducibility for CB analysis by spICP-MS. However, about half the paired comparisons between differing CB concentrations were found to be statistically different from each other.
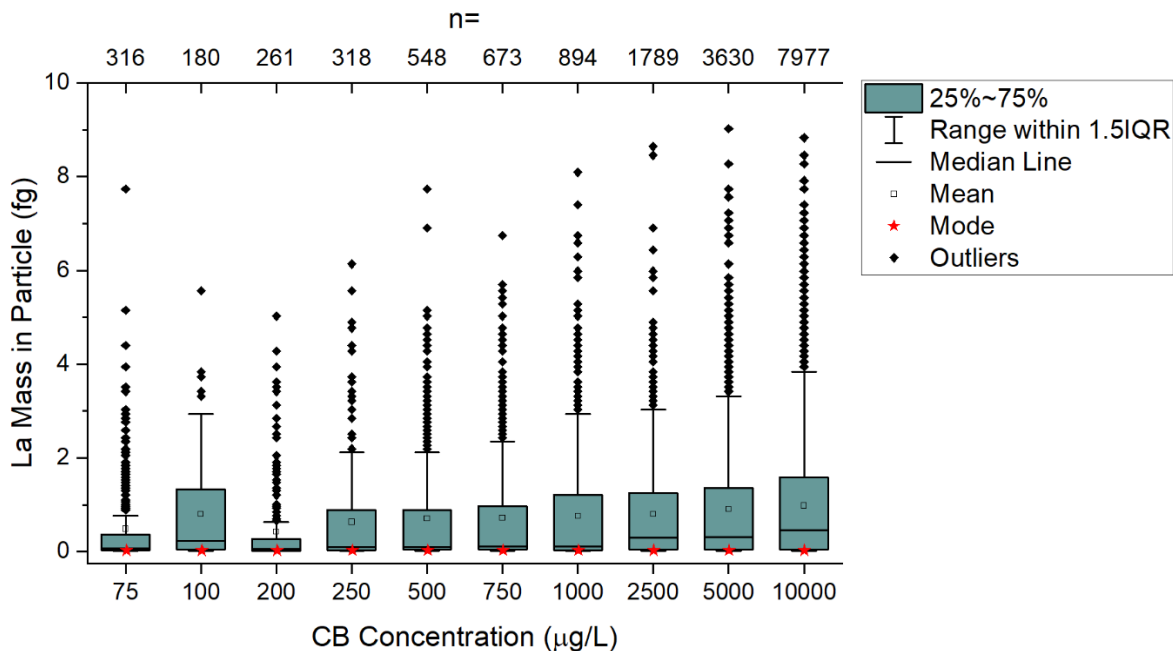
Figure 2.5: Distributions of CB particle size, in terms of La mass in femtograms (fg), measured in all CB concentrations using spICP-MS. Replicate analyses were combined into one dataset for each concentration, where n is the total number of particles counted.

Many of the significantly different pairwise comparisons were between concentrations for which very different particle counts (n) were obtained. This suggests that the variation in distribution shapes, which appear minor but result in appreciable differences, are a consequence of a low number of observations (n) and can be resolved by increasing the number of particles counted which make up the distribution. It is already known that spICP-MS sizing can suffer when counting statistics are poor and this may be overcome with longer analysis times[120], thereby increasing the number of measured particles contributing to the distribution, or by analyzing a more concentrated sample. The influence of the number of observations (n) on the distribution shape is clearly seen in the lowest CB concentrations analyzed. Whereas all other concentrations tested were analyzed as the average of four replicates, ten replicates were analyzed for the 75 µg/L

CB set, which brought the total number of particles counted closer to that of the 200 and 250 µg/L distributions as shown in Figure 2.5. Notably, the distribution of the pooled 75 ug/L masses are more comparable to the 200 and 250 µg/L samples and in fact, the Dunn's Test results indicated no significant differences between these three concentrations. This supports that while low concentrations require extended analysis time, spICP-MS can provide highly reproducible results for quantifying particulate La masses in CB.

3.5 Analytical Implications for Carbon Black Detection

The current study pushed the capabilities of spICP-MS with a standard quadrupole mass analyzer to its analytical limits in the quantification of CB M1000 particles by detection of trace La impurity. Our evaluation of the new application of this technique indicates that this approach can detect down to 64 µg/L and quantify CB mass concentrations down to 122 µg/L, with a high degree of accuracy and reproducibility. Additionally, spICP-MS size measurements of the particulate La impurity in CB suspensions reliably determined the most abundant (mode) particulate La mass as well as provided estimations over the mean and interquartile range, with improved resolution of mass distributions at higher particle counts. While the results obtained are based on the M1000 CB variety, the same approach can be utilized for other graphitic nanoparticles containing residual catalysts or other sources of trace metal impurities. The analytical sensitivity and detection limits can be expected to vary depending on the abundance of the tracer in the material of interest, but these limits can be improved by optimizing sample stability with the addition of surfactant and extending analysis time in order to maximize the particles counted. For future use of this method in monitoring scenarios or leaching studies, we suggest (i) identifying metal impurities that are suitable to serve as analytical tracers, (ii) verifying the use and impacts of non-ionic surfactants such as TX-100 for optimum detection, and (iii) establishing a calibration

54

to investigate detection limits for carbon particles of known metal content. This technique has been validated for quantifying CB concentrations, filling an analytical need in future studies measuring the presence and/or accumulation of CB, of known metal content, in drinking water matrices.

Figure 2.6: Graphical Representation of CB detection by spICP-MS
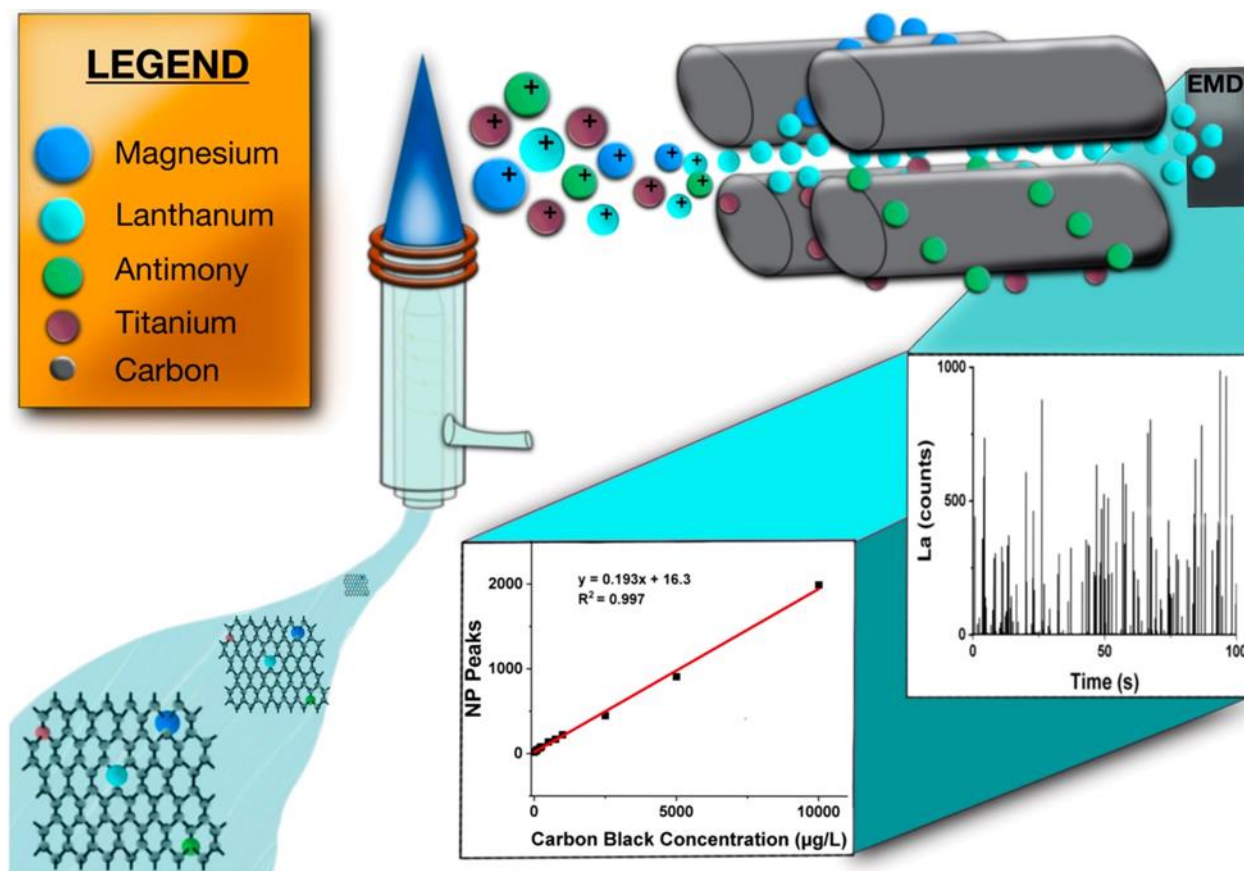
CHAPTER III

OUTLINING KEY PERSPECTIVES FOR THE ADVANCEMENT OF ELECTROCATALYTIC REMEDIATION OF NITRATE FROM POLLUTED WATERS[3]

1 Nitrate pollution in groundwater & its adverse health effects -

Industrial conversion of atmospheric nitrogen (N_2) into ammonia (NH_3) through the Haber-Bosch process has been essential in sustaining large-scale agriculture. However, artificial nitrogen fixation has increased the influx of nitrogen species into the environment leading to an imbalance of the natural nitrogen cycle.[121,122] Ammonium (NH_4^+) and nitrate (NO_3^-) are the most common nitrogen containing compounds for plant nutrition, while urea is also considered another important source for nitrogen containing species for agriculture.[123] Both NH_4^+ & NO_3^- are present within artificial fertilizers at appreciable concentrations. The NO_3^- concentrations are noteworthy because they are typically higher by a factor of 10 –1000 fold. The higher concentrations of NO_3^- versus NH_4^+ is due to rapid nitrification in soils resulting in the conversion of NH_4^+ into nitrite (NO_2^-) and further oxidation to form NO_3^-.[123] Approximately half the nitrogen applied to crops is lost to the environment, which results in considerable accumulation of nitrogen species in both ground and surface waters.[124] The continuous accumulation of nitrogen compounds in the top-soils after growing seasons steadily increases soil nitrate concentrations, which can further pollute water

---

[3] Reprinted from K. Flores, G. Cerrón-Calle, C. Valdes, A. Atrashkevich, A. Castillo, H. Morales, J. Parsons, S. Garcia-Segura, J. Gardea (2022) Outlining Key Perspectives for the Advancement of Electrocatalytic Remediation of Nitrate from Polluted Waters. *ES&T Engineering*, 5, ©2022 American Chemical Society. All rights reserved.

sources surrounding agricultural regions.[125] Nitrate exhibits high solubility and mobility within water, which results in the rapid permeation throughout aquifers. High levels of nitrate pollution in groundwater and other drinking water supplies is an ongoing issue within agricultural areas throughout the globe.[126] Figure 3.1 provides a mechanistic description of the transport of nitrate in agricultural regions.
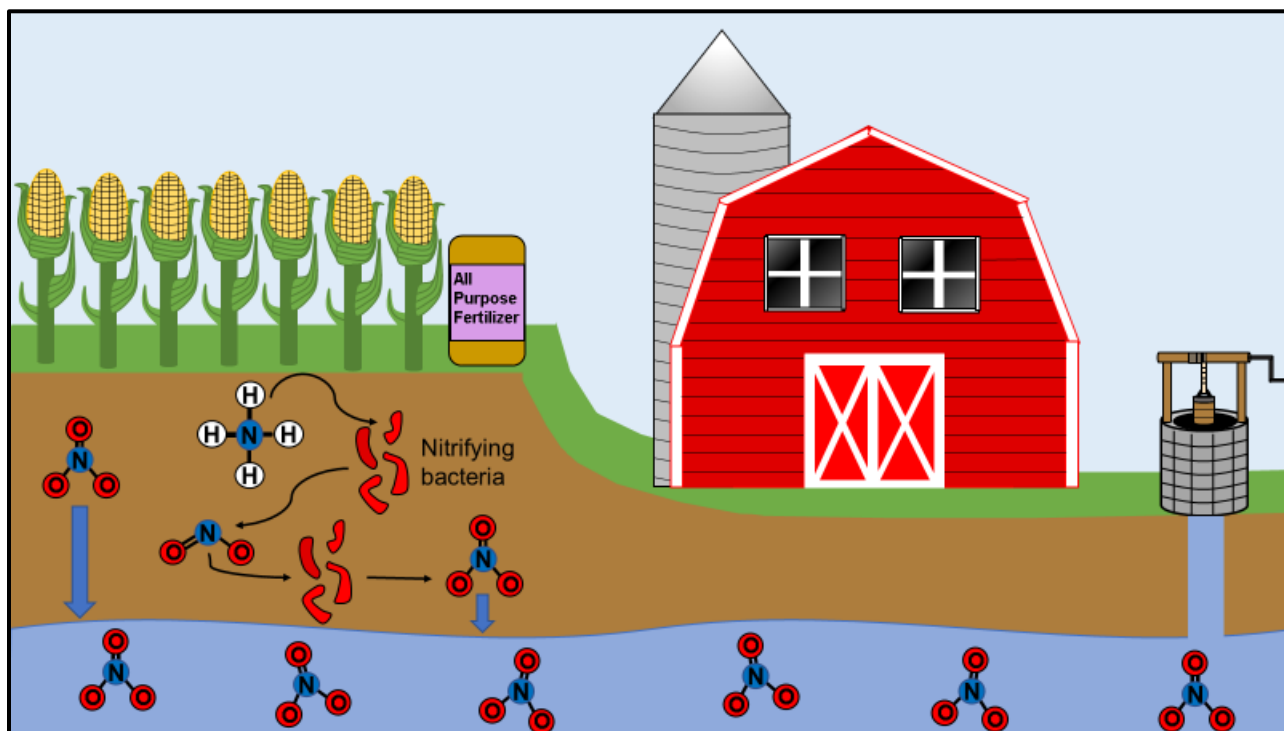
Figure 3.1: Permeation of nitrates into groundwater sources from the application of fertilizers to crops.

Anthropogenic input of N-species has been associated to severe environmental issues (e.g., acid rain, algal blooms) and deleterious effects to human health such as methemoglobinemia and cancer.[127] Methemoglobinemia is a blood condition where methemoglobin, an abnormal form of hemoglobin, is produced in excess. Methemoglobin is unable to transport either oxygen or carbon dioxide throughout the body resulting in hypoxia.[128] Ingestion of elevated nitrate concentrations in drinking water has been correlated to the development of gastric cancer. Once nitrate enters the body it can react with various organic compounds to form nitrosamines and mitrosamides.[129]

Mitrosamides and nitrosamines are believed to be carcinogenic compounds for humans, these compounds can be further metabolized into a DNA alkylating agents[130]. High ingestion of nitrates may also lead to hypertension, goiter, and various congenital birth defects.[129] In the United States a maximum contaminant level (MCL) of 10 mg-N/L (ppm) for NO_3^- in public drinking water has been set by the Environmental Protection Agency (EPA). The MCL was defined to protect infants from blue baby syndrome – infant methemoglobinemia,[131] although more stringent limits may be considered in the near future given the identification of nitrate as a carcinogenic trigger. Recent studies conducted in Spain, Italy, and Denmark reported that ingestion of nitrate between levels 0.7 - 2.0 mg/L significantly increased an individual's risk for colorectal cancer, therefor current MCLs should be reconsidered with the risks present.[132,133] High concentrations of nitrate over the MCL currently limits access to drinking water sources; therefore, the development of flexible technologies and point of use systems have been identified by the national academy of engineers as an urgent need.

Conventional technologies used for the removal of nitrate from ground water include physical separation technologies and biological processes.[134–136] Ion exchange and reverse osmosis are the most common physical separation approaches implemented in the past to remove nitrate from drinking water, however, they generate concentrated NO_3^- brines. The secondary waste requires further treatment and/or disposal, which leads to increased remediation costs and environmental risks.[137] Biological denitrification requires careful control of the pH, temperature, dissolved oxygen, and dissolved organic matter content of the reaction solution. In addition, the requirement for large reactors, to improve conversion rates, also limits the application of the aforementioned process.[138] Electrocatalysis is an emerging compact technology that is attractive

given its product selectivity, low overall cost, and no requirements for additional chemical treatments.[139–141]

This review outlines major engineering principles for the electrocatalytic reduction of nitrate including engineering figures of merit. Recent advances on electrocatalytic materials are discussed focusing on advanced materials with high selective reduction of nitrate towards: (i) innocuous nitrogen gas for drinking water applications and (ii) ammonia as a resource recovery approach. Differential topics covered in this work explore key aspects that require more attention to ensure successful advancement of electrochemical reduction of nitrate as an emerging water treatment technology. In particular, emphasis is placed on the advancement of non-platinum group metal catalyst as sustainable and techno-economic competitive electrocatalysts to minimize reliance of water technologies on costly noble metals. Discussions are supported by providing techno-economic perspective to clarify reasons for such specific need. Bimetallic electrocatalysts, metal oxides, and metal sulfides are emerging as promising electrodic interfaces for nitrate reduction as described herein. Water matrix effects from the pH of the reaction solution and coexistence of ions are examined, including combination with electrochlorination processes. Finally, aging and fouling are discussed as key parameters to evaluate the lifetime of electrochemically driven systems under real conditions.

2 Introducing fundamentals of electrocatalytic reduction of nitrate

Electrocatalytic water treatment exploits the use of delivered electrons into a system to perform chemical reactions that otherwise will not spontaneously occur. This treatment technique is governed by reduction and oxidation (REDOX) reactions occurring at the interface

59

of at least two distinct electrodes: a cathode for reduction reactions, and an anode for oxidation

reactions.[142]
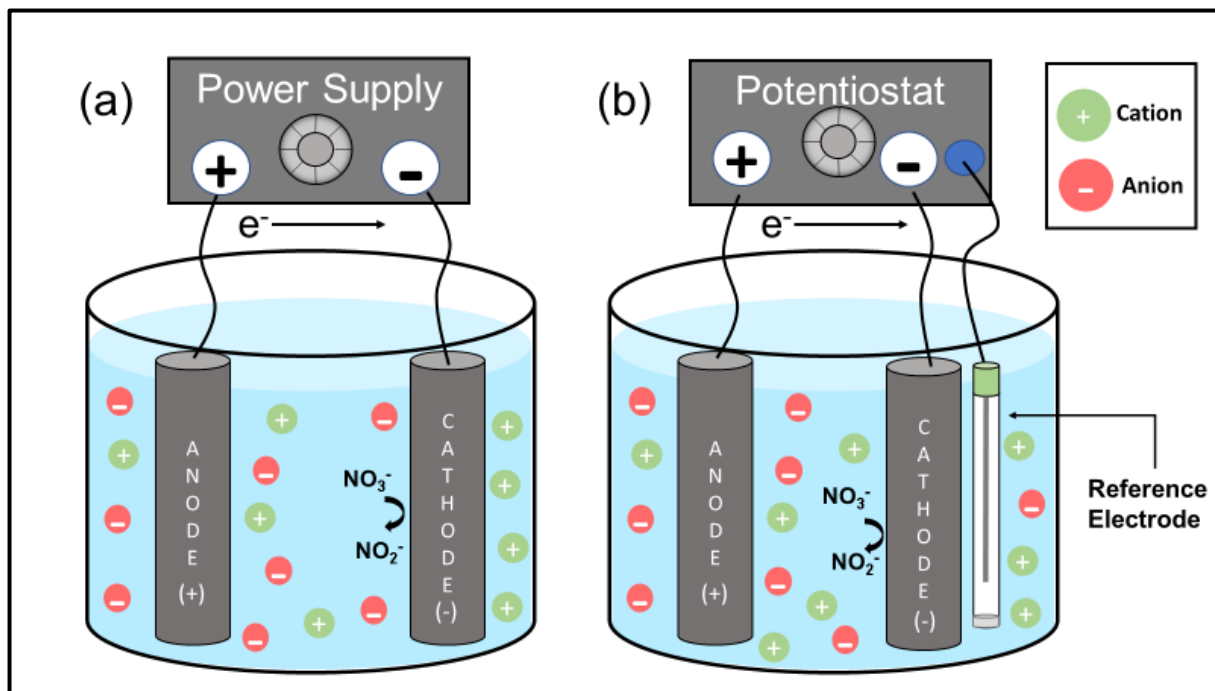
Figure 3.2: Different electrochemical configurations for the electrocatalytic reduction of nitrate (a) two electrode galvanostatic and (b) three electrode potentiostatic.

The electrolytic solution is comprised of ionic species that contribute to the solution conductivity.

The species in solution that are involved in either reductive or oxidative processes are referred to

as the electroactive species. Note that not all the species in solutions are necessarily electroactive

and may present inert character to redox processes under the given conditions (e.g., Na^+, ClO_4^-,

etc.). In electrochemical systems both reduction and oxidation reactions take place simultaneously.

However, the main emphasis for the electrocatalytic reduction of nitrate (ERN) is placed on the

reactions occurring at the cathode. Therefore, cathodic performance should be of extreme

importance for ERN processes, and proper metrics should be used to benchmark the catalytic

activity. The turnover frequency (TOF) is an important metric overlooked in many studies and is

telling of the intrinsic activity of catalytically active cathodes. Simply put, the TOF refers to the

number of revolutions of the catalytic cycle per unit of time, or the number of products made per

catalytic site per unit time. This value is crucial for comparing catalyst reproducibility in other labs, comparing different catalyst, and even for comparing size and crystal facet contributions to the overall catalytic activity.[143] Equation 1 below, represent a simple relationship between products and catalyst in order to establish a TOF value, based on flow by treatment.[144]

$$TOF = \frac{mmol\ (product)}{mmol\ (catalyst)} \div residence\ time \qquad \text{Eq (1)}$$

The two distinct operational modes for electrocatalysis of nitrate are galvanostatic and potentiostatic. A galvanostatic approach consists of a system under a fixed current density and typically utilizes a dual electrode (cathode and anode) configuration, see Figure 3.2a for visual representation. The electrical current density is defined as the fraction of current associated to the electroactive unit area of the electrode.[145] Applied current controls the electro kinetics of the process for this defines the number of electrons delivered per second, but does not provide accurate control over the preferential thermodynamic processes that takes place at the electrode surface. This lack of control on the working electrode potential results in lower Faradaic efficiencies given the enaction of coexisting parasitic reactions (i.e., hydrogen evolution reaction). Whereas, potentiostatic electrocatalysis is performed under a constant potential applied to the working electrode.[146] In order to control the applied potential to the working electrode a three electrode configuration is required. Note that application of a fixed potential without a reference electrode does not provide control over the working electrode potential, that defines the reactions taking place according to thermodynamics, but only the cell potential. The cell potential is a measure of the overall potential used in the operation, including the ohmic drop, and does not provide insight into the actual cathodic potential which dictates charge transfer reactions. Potentiostatic mode of operation includes a cathode as the working electrode (WE), an anode as the counter, and finally a reference electrode (RE) in which the cathodic potential is referred to (e.g., Ag/AgCl). The

reference electrode is utilized to continuously measure the surface of the WE in order to maintain a constant potential, see Figure 3.2b for visual representation of a RE in a potentiostatic system.[145]

The galvanostatic operation is the principal choice for scaling-up operations given its flexibility and adaptability in electrochemical engineering systems. Although the industrial scalability and cost-effectiveness of potentiostatic electrocatalysis is limited, the use of REs greatly improves product selectivity. Potentiostatic application is essential for fundamental and mechanistic studies, but the requirement of REs may hinder the scaling of this technology for engineering applications of electrified systems. The Faradaic efficiency (FE) is a figure of merit to evaluate the effectiveness of ERN comparing the experimental charge (Q_{exp}) to the theoretical conversion charge (Q_{theo}) according to the equation:

$$FE\ (\%) = \frac{Q_{exp}}{Q_{theo}} \times 100 = \frac{n \times N_i \times F}{t \times I} \times 100 \qquad \text{Eq (2)}$$

where the numerator (Q_{exp}) is calculated through multiplication of n, the number of electrons required per mole of product (mol e- mol^{-1}), N_i the amount of product generated during experiment (mol), and F is the Faradaic constant (96 487 C mol^{-1} of e-), which is then divided by the denominator (Q_{theo}) determined from t (time in hours) and I the current intensity (A).

FE values higher than 90% for nitrogen and ammonia production via potentiostatic electrolysis has been reported in the literature.[147,148] Whereas, galvanostatic experiments usually report lower FE values ($< 50\%$).[149,150] Thus, it has been noted that potentiostatic electrocatalysis is superior in product selectivity compared to the galvanostatic approach resulting in higher Faradaic efficiencies (FE). Product selection is enhanced by minimizing, or hindering, competitive reactions, occurring at overpotentials close to the reaction potential. Applying the precise potential to the electrolytic system allows for control over the electron transfer from the WE to the desired

electroactive species.[151,152] Whereas, under galvanostatic operation the cathode potential may change over time, or it can be located at higher potentials than required for nitrate reduction, therefore, enabling and/or enhancing the extent of competitive reactions that exist close to the nitrate reduction potential. One of the most common competitive reaction in ERN is the hydrogen evolution reaction (HER).[153] This reaction consumes electrons to produce hydrogen instead of fueling nitrate reduction. However, some articles reported added benefit to obtaining hydrogen near the electrode due to the high reduction activity through an indirect catalytic hydrogenation mechanisms.[154,155] The low technology readiness level of potentiostatic electrocatalysis is mainly attributed to the requisite of the reference electrode, complicating the design of scaled applications. Thus, galvanostatic operations have been considered as the most promising approach for scaled operations. This is a relevant aspect to highlight since the comparison of galvanostatic and potentiostatic results in comparisons in selectivity that should not be conducted.[156,157] Furthermore, simple evaluation of potentiostatic conversions may lead to an undesired over-estimation of electrocatalytic systems performance. Another important engineering figure of merit directly related to operational costs is the electrical energy per order (EE/O). The EE/O considers the electrical energy in kilowatt hours (kW h) required to reduce the pollutant concentration (*C*) by one order of magnitude in a unit volume of sample. The EE/O (kW h m^{-3} order^{-1}) for batch operation mode can be estimated from the following equation:

$$E_{EO} = \frac{E_{cell} \times t \times I}{V \times \log(C_0/C_f)}$$

Eq (3)

where E_{cell} is the cell potential (V), t corresponds to the time, *I* is the current intensity, *V* is the water volume (m^3), C_0 and C_f correspond to the initial and final concentration. Different electrode materials present different values of EE/O for the same application and similar treatment conditions. Note that some electrodes with high selectivity towards a desired product may have a

low energy efficiency due to excessive electricity consumption. Thus, trade-offs may exist when defining selection criteria of materials. When considering nitrogen reduction reactions it is ultimately necessary to steer the reduction mechanism towards specific final products in function of the desired final application.[158] This includes (i) evolution of innocuous nitrogen gas when aiming for drinking water purification, or (ii) electrogeneration of ammonia as a resource recovery for wide variety of applications; including pharmaceuticals and textiles, a source of hydrogen storage for fuel cells and other hydrogen driven technologies, and as ammonia enriched waters for agricultural irrigation.[159,160] These applications are visually displayed in the graphical abstract portion of this work. Nitrate removal (NR) is another common term used for electrocatalytic systems, yet this consideration is less specific only taking into concern the initial and final $[NO_3^-]$ calculated as follows:

$$NR = \frac{[NO_3^-]_{initial} - [NO_3^-]_{final}}{[NO_3^-]_{initial}} \times 100 \qquad \text{Eq (4)}$$

From a thermodynamic standpoint the reduction of nitrate is a nonspontaneous process which requires additional energy to overcome an activation energy barrier. To overcome this activation energy barrier, an overpotential is necessary to facilitate the reduction of nitrate. In electrocatalysis, efforts to minimize the applied overpotential is crucial for this is related to the overall energy expenditure of the system. A common strategy for reducing the overpotential includes surface activation prior to electrolysis. In the case of Rh electrodes pretreatment in KCl electrolyte induced surface modifications which decreased the overpotential by 27 kJ/mol (0.28 eV/particle) when compared to the inactivated surface.[137] Energy expenditure of the system may also be affected by other factors including electrolytic solution resistance and mass transport of electroactive species. Concentration optimization much also be considered as the mobility of

nitrate ions is dependent on concentration of nitrate present and the ionic strength of the reaction solution, with highest mobility occurring under dilute conditions.[145] Moreover, adsorption/desorption processes occurring at the interface of the cathode, and formation of various species in the vicinity of the electrodes can result in re-oxidation of the already reduced species, which can also have impacts on current efficiency.[146] Techniques used to minimize the re-oxidation of already reduced nitrate species include the use of divided cells by salt bridges and/or ion exchange membranes. Note that both approaches can minimize competitive reactions at the expense of increasing ohmic resistance and therefore resulting in higher energy consumption.

3.0 Selecting cathodic material as key aspect of translational efforts

Product selectivity and reaction kinetics of electrochemical reduction of nitrate is heavily influenced by the choice in cathodic material.[161,162] For a majority of metal cathodes, the initial reduction is regarded as the rate-determining step, but other factors such as the pH of the reaction solution, applied potential to the cathode, and coexistence of ions may alter/affect the ERN mechanism.[163,164] It has not been fully explored how pH and applied potential affect the rate-controlling step, which is an aspect that should be addressed in future fundamental research of interfacial electrodic processes for nitrate reduction. Fundamental studies suggest that for noble metal interfaces the nitrate reduction process may require an initial nitrate adsorption on the cathode surface following reaction (5). Nitrate adsorption would be required to enable inner sphere charge transfer process, despite other indirect reduction processes may co-exist (i.e., hydrogenation). Here it is important to remark that mechanistic intricacies are dependent on electrode interface characteristics as well as electrocatalytic material nature. Mechanistic pathways that require adsorption have been evaluated using electroanalytical tools that evaluate in situ surface coordination. A seminal study from da Cunha et al. suggest that the adsorption of nitrate

is driven through a two-fold coordination on Au and Pt, which might be translated to other noble metal cathodic surfaces.[165] Adsorbed nitrate can then undergo charge transfer when adsorption takes place under cathodically polarized surfaces, but there is some discussion regarding possible charge transfer induced by the adsorption itself according to hydrogen underpotential deposition measurements on previously hydrogenated (H_{ads}) surfaces.[164] Thus, that would hint co-existence of direct and indirect electrochemical reduction pathways. Indistinctly of the initial steps or the inner sphere or outer sphere nature of the mechanistic pathway, the initial reduction reaction of nitrate that generates nitrite may be described by consecutive reactions (6) – (8).[166]

$$NO_3^-{}_{(aq)} \leftrightharpoons NO_3^-{}_{(ad)} \qquad\qquad \text{Eq (5)}$$

$$NO_3^-{}_{(ads)} + e^- \rightarrow NO_3^{2-}{}_{(ads)} \qquad\qquad \text{Eq (6)}$$

$$NO_3^-{}_{(ads)} + H_2O \rightarrow NO_2^{\bullet}{}_{(ads)} + 2\ OH^- \qquad\qquad \text{Eq (7)}$$

$$NO_2^{\bullet}{}_{(ads)} + 2e^- \rightarrow NO_2^-{}_{(ads)} \qquad\qquad \text{Eq (8)}$$

This electrochemical-chemical-electrochemical (ECE) mechanism is generally summarized by the general expression of bielectronic equation (9) that also describes the alkalinization induced as result of nitrate reduction reaction.

$$NO_3^- + H_2O + 2e^- \rightarrow NO_3^{2-} + 2\ OH^- \qquad\qquad \text{Eq (9)}$$

The adsorption of the nitrate species on the cathode surface is critical since the charge transfer reaction occurs through an inner sphere process requiring direct interaction (adsorption) of the electroactive species (i.e., nitrate) with the surface of the cathode. For the adsorption of NO_3^- ions upon the cathode surface, these ions must travel from the bulk solution to the electrode-solution interface. The heterogeneous electrocatalytic reaction can be controlled by charge transfer or by

mass transport from/towards the electrode surface. The mass transfer-controlled process is defined by three mechanisms. The first, diffusion, refers to the movement of ions from areas of high to low concentrations, typically referred to as a gradient. The second mechanism convection refers to the hydrodynamics or movement of fluid in the system, which in context of electrochemical experimentation refers to mechanical stirring. Finally, the last process migration, arises from electrostatic interaction being produced by an applied potential. [167] With these considerations noted, the following sections outline the most commonly studied classes of cathodic materials (i.e., platinum group metals & bimetallic) as well as emerging electrode materials that are gaining traction given their prospective competitive character and sustainable nature (i.e., metal oxides, graphitic composites, and metal sulfides).

3.1 The cost-prohibitive platinum group metals

Platinum group metals (PGMs) have been utilized in a variety of catalytic processes because of their substantial catalytic activity and resistance to corrosion. In terms of nitrate reduction, PGMs have been known to be capable of producing desired products (N_2) via electrocatalysis but suffer from sluggish kinetics. The activity of these materials proceeds as Rh > Ru > Ir > Pt ≈ Pd based on the current densities observed for ERN under identical conditions.[168] Rh and Ru metals express superior activity for reductive processes, but these metals have been known to suffer from catalyst poisoning, or inactivation, during extensive electrochemical applications. Rhodium electrodes display preferential adsorption of hydrogen leading to catalyst poisoning, resulting in the inhibition of nitrate adsorption and in turn inhibited nitrate reduction. In order to combat the catalyst poisoning Tucker and coworkers developed an electrochemical activation method where the Rh electrodes were subjected to oxidation/reduction cycles in a KCl

electrolyte containing nitrate ions, leading to partial dissolution of the surface Rh. The morphological changes brought forth by the catalyst activation increased the reactive surface area, reduced the activation energy necessary for the reduction of nitrate, and increased the range of overpotentials where noncompetitive reduction of nitrate occurred.[137] This led to preferential N_2 formation from the reduction of nitrate on activated Rh electrodes, rather than the reduction of water molecules. Although enhanced activity for N_2 formation was observed, this was short lived because of instability of the activated surface. Ultimately N_2 formation decayed, and hydrogen evolution and ammonia formation prevailed.[137] In a similar fashion synthesized Ru strained nanocluster expressed an inhibition to HER activity due to increased energy requirements for the dimerization of hydrogen, compared to the unstrained variety. The induced strain, brought forth by subsurface oxygen doping, greatly reduced the activation energy for nitrate reduction resulting in catalytic activity (5.56 mol g_{cat}^{-1} h^{-1}) greater than the Haber-Bosch process for the production of ammonia. With the strained Ru clusters an increase in the energy requirement for hydrogen dimerization allowed for greater access to H* radicals, which was confirmed by electron spin resonance spectroscopy. This greater access to radicals, as well as the decreased activation energy, culminated to an effective catalyst design if nitrate reduction is intended for ammonia formation.[169]

Pt and Pd electrodes have been extensively tested because their ability to steer the reaction mechanism towards gaseous nitrogen products (N_2, N_2O) and NH_3, while maintaining a resistance to corrosion. Cunha et al., found that for electrodeposited Pt cathodes produced a mixture of N_2O and NO at potentials between 0.5 and 0.2 V vs. reversible hydrogen electrode (RHE) while lower potentials (<0 V) created a non-selective mixture of N_2, NH_2OH, and N_2H_2. The authors concluded that N-O bond breaking, and N-N coupling reaction occurred between potentials of 0.5 and 0.2 V vs RHE, while at potentials lower than 0 V vs RHE created a mixture of non-selective N-O

breaking, N-N forming, and N-H forming.[170] The ERN over Pd nanoparticles was recently investigated to determine the structure sensitivity of various crystal facets, Pd (100) and Pd (111), contained within specific particle shapes in order to elucidate the contributions from each surface.[171] Experimental studies were conducted in tandem with density functional theory (DFT) calculations in order to calculate the energy of species absorbed on the Pd surfaces in aqueous solution. A cuboctahedron shape of both facets - eight (111) and six (100) facets - was experimentally proven to have the highest yield of NH_3 from the ERN. The Pd (111) surface was calculated to have a lower energy barrier for NO_3^- adsorption and dissociation ($NO_3 \rightarrow NO_2$) leading to higher activity for this rate limiting step - the initial reduction. The Pd (100) surface was identified as the facet controlling product selectivity, due to its adsorption character of $*NO_2$ species. The higher degree interaction on the Pd(100) surface led to further dissociation to $*NO$ and finally NH_3, rather than desorption of $*NO_2$ to leading to release of aqueous nitrite as seen on the Pd (111).[171] These findings perfectly exemplify the utility of both activity and selectivity in catalytic processes. More fundamental studies like this, backed with DFT calculations, will be extremely important in the future of material selection for ERN applications.

The main inflection points for any material selection are the techno-economic aspects and material sustainability. Figure 3.3 illustrates the market price trend of the PGMs as raw material (manufacturing costs not associated) over the past 10 years (see Figure 3.3a). These costs are several orders of magnitude higher than other conventional raw materials that can be alternatively used (see Figure 3.3b). The exorbitant price of PGM materials raises questions about the cost-competitiveness of any water treatment system relying on their use.
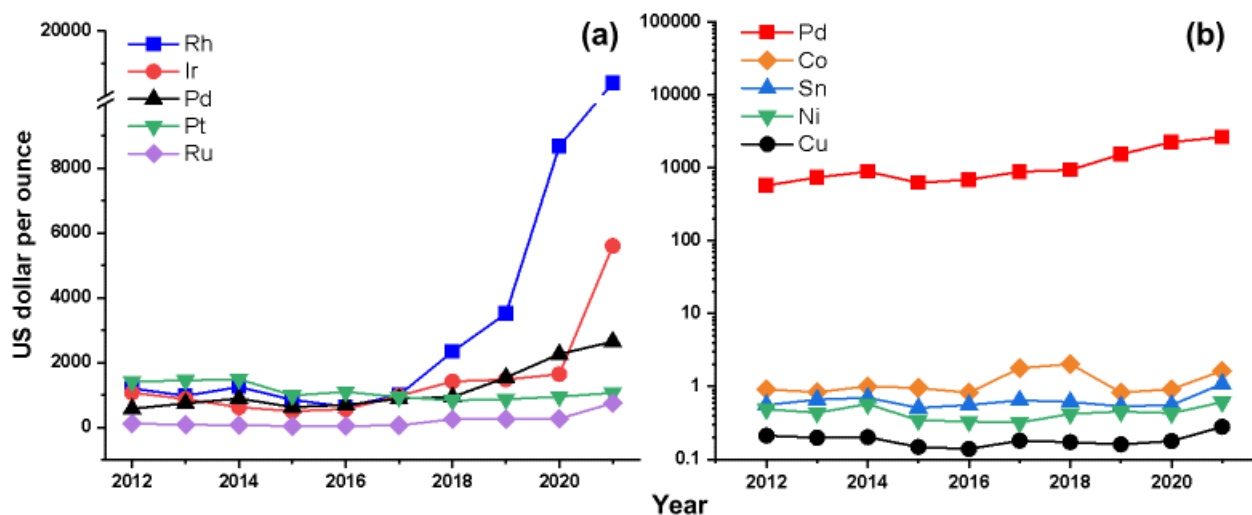
Figure 3.3: Price of PGM over the past ten years in US dollar per ounce (Y-scale linear) (a). Comparison of Pd and alternative catalytic materials of higher abundance and considerably lower cost (Y-scale logarithmic) (b). Prices determined mid to late July of each year. Adapted with permission from information gathered from ref. Copyright 2022. TRADING ECONOMICS.

Table 3.1: Cost in US dollars per ounce of PGM material as of 11/19/2021. Adapted with permission from information gathered from ref . Copyright 2022. TRADING ECONOMICS.

PGM Material	USD per ounce (11/19/21)
Platinum	$ 1,031
Palladium	$ 2,062
Rhodium	$ 14,350
Iridium	$ 4,400
Ruthenium	$ 600

Overexploitation of resources and low availability of certain elements in Earth crust may endanger sustainable development. Based on these principles "endangered elements" have been defined as elements in the chemical/engineering enterprise that may face critical supply risks. The periodic table of endangered elements developed by the American Chemical Society summarize the prospective risks of sustainable availability of different elements based on their availability and actual use/demand.[172] The identification of PGMs as endangered elements, in which extraction may not be sustainable, considers the overall life cycle assessment of these materials which pinpoints PGMs as unsustainable in the long run.[173–175] Because of price and sluggish kinetics, the use of pure PGM materials has decreased over the years, leading to increasing investigation of cost-effective materials. This has steered researchers towards the investigation of bimetallic

70

catalysts which utilize very minuscule amounts of PGM materials in order to produce a better cost-effective alternative to pure PGM electrodes while maintaining catalytic efficiency and selectivity.[176] To apply a cost comparison in a more effective manner it would be constructive to compare the price, for raw materials alone, of a highly reactive bimetallic electrocatalyst (Cu-Pt) to the price for the same size pure Pt electrode. A recent techno-economic analysis conducted on electrified water treatment found that the cost of the electrode material was an area of much importance in terms of maximizing the cost effectiveness of this technology.[177] Relying on an electrocatalyst design by Cerrón-Calle et al., for a highly active cathode for the reduction nitrate an electrode of a 10 cm^2 geometric area would cost approximate \$2.15 USD.[178] The bulk of this material would be copper foam (99.64%) which would account for \$1.60 USD while the remaining mass (0.36%) would come from the Pt nanoparticles with approximately \$0.50 USD in costs. Based on the market prices displayed for Pt in Table 3.1 the same size pure Pt electrode would cost a staggering \$7,800 USD, over 3600X times the price for the bimetallic counterpart. Nano decoration of Pt on low-cost bulk copper foam provides am effective catalyst design by maximizing activity, while minimizing the mass requirements for the PGM material. The added benefit of increased surface area and reactivity with nano enabled technologies could be a viable design option when looking for low-cost highly active electrodes for water remediation. The long-term stability of these nanosized particles would be of major importance for establishing the utility of nanotechnology and will be a major topic of discussion at the end of this work.

Techno-economic analysis (TEA) are useful tools to evaluate competitiveness of novel systems while also being essential to research roadmaps that assist in the advancement of technologies to higher readiness levels. Due to the fact that ERN systems are not currently in commercial operation, a TEA at this point in time can only be speculative in nature. Only a

preliminary TEA can be conducted taking many assumptions in consideration. One of the major assumptions would be related to the expected life of electrode systems under different water matrix conditions, which would be function of aging and fouling processes. Unfortunately, these are aspects seldomly explored in literature and they must be further analyzed to gauge their possible effects on the ERN. There are some recent works that indicate that need for preliminary TEA for electrified systems based on catalytic conversion.[179,180] The TEA can indicate niche applications for ERN while identifying barriers that should be addressed to enhance its competitiveness. Thus, it is evident that conducting TEA will arise as a need to enhance our understanding of electrocatalytic systems for water treatment.

3.2 Bimetallic electrodes to decrease reliance on PGMs

The use of two metal components to create electrodes has become a popular approach for the ERN. The creation of bimetallic catalysts stemmed from the observation of increased catalytic activities or physical properties when using dual metals, which are superior to the individual metal materials/particles.[181] Utilizing two metal components to create these electrodes has been thought to enhance the catalytic activity towards the reduction of nitrate, while simultaneously influencing product selectivity.[139] A popular approach for the creation of bimetallic catalysts is the combination of a PGM (either Pd or Pt) with a non-precious metal called a promoter (such as Cu, Sn, In, Co, Mo, and Fe). The PGMs influences product selectivity towards $N_{2(g)}$, while simultaneously stabilizing the less noble metal. The non-precious promoter is believed to accelerate the rate-determining step of the reaction (the initial reduction from NO_3^- to NO_2^-). [163,178,182] This approach holds the promise of minimizing the reliance on PGM by significantly reducing the mass of these metals required for the electrocatalytic reactor. In addition, it has

been proposed that using two or more metals creates a multifunctional surface, which has more than one type of adsorption site for ions. A multifunctional surface would prove useful by providing distinct binding sites for nitrate ions, intermediates, and hydrogen atoms and provide distinct overpotentials to alleviate possible interferences.[183] Bimetallic nanocomposites strategically exploit the unique properties of both components that get synergistically enhanced.

A conventional bimetallic catalyst (segregated) is comprised of separate metal components or clusters who are joined together at an interface, or multiple interfaces, but still maintain character of their individual metal components. Conversely, an alloy (bimetallic mixture) is a mixture of atoms from the two metals creating different atomic structures from the individual metals resulting in a solid solution with distinct alloy phases, see Figure 3.4 for further clarification. Utilization of Cu as a promoter has become a well-favored approach for segregated bimetallic catalyst utilized for ERN. This is due to observation of Cu accelerating the rate limiting step, initial reduction of NO_3^- to NO_2^-, through efficient adsorption of nitrate ions.[184,185] In addition, copper is a relatively affordable choice in catalytic material therefore using this metal in conjunction with other PGM brings down the overall price of the catalyst.[186] For Cu/Pd nanoparticles, supported on nickel foam, researchers reported a high selectivity towards N_2 formation (99%) for this segregated bimetallic electrocatalyst. The dual metal centers allowed for the accommodation of NO_3^- and NO_2^- ions on the Cu (100) plane apart from the hydrogen adsorption hotspots found on the Pd surface. The bimetallic catalyst design created a 3D grapelike like structure that resulted in high surface area with diffusion channels for efficient ion accommodation.[139] Such adsorption character on copper has been corroborated in other works. Bae S. et al. found substantial coverage of NO_3 occurred at a potential of - 0.3 V vs Ag/AgCl on the surface of the Cu (100), in comparison to other planes, confirmed by in situ electrochemical

scanning tunneling microscopy. Between a potential of -0.3 V and - 0.5 V nitrite was found to be the predominate species on the same surface. Both NO_3^- and NO_2^- species adsorbed as a (2x2) adlayer to the Cu (100) surface occurring through bidentate interaction with the oxygen atoms of the ions.[187] For a Cu/Ni segregated bimetallic electrocatalyst, decoration of Cu particles (900 nm) on the Ni surface drastically boosted nitrate reduction. An increase of approximately 84 % in the nitrate removal capacity for the Cu/Ni bimetallic catalyst, compared to pure Ni foam, was attributed to better adsorption of nitrate on the Cu sites and decreased resistance to electron transfer. The high standard reduction potential (0.597 V), in reference to the standard hydrogen electrode (SHE), between Cu and Ni created numerous galvanic cells resulting in increased current densities and accelerated electron transfer for this reductive process.[188] For these reasons copper has risen in popularity for ERN due to its nitrate and nitrite adsorption properties, tunable electronic properties, and low overall cost. In addition to dual metal center the fabrication method of electrocatalyst has been known to affect structure/morphology and in turn product selectivity of electrocatalytic materials. A study by Jenn Fang Su et al., investigated the effects of variance in the electrodeposition process and how this affected selectivity towards N_2 formation. The authors increased the amount of reaction solutions used to introduce Sn and Pd to a stainless-steel mesh electrode. With the crystalline size of the synthesized Sn_3Pd increasing linearly with the number of reaction solutions. The authors designed a deposition method where the reaction solution first contained both Pd and Sn cations in a 1:4 ratio. This continued with various pure solution of each cation for the electrodeposition, see Figure 3.5 for further clarification. The first approach was the most successful, which resulted in the formation of the highest amount of $N_{2(g)}$ (82%), with the smallest crystallite sizes of Sn_3Pd (214), Sn_3Pd (131), and Sn_3Pd (420). Surface roughness was correlated (inversely proportional to crystallite size) to the number of containers used (see Figure

3.5a). The authors concluded the formation $N_{2(g)}$ from the catalytic reduction of nitrate was affected by crystal facet distribution, please see Figure 3.5b for the relation between N_2 selectivity and crystallite size, arising from the number of cation containers used in the electrodeposition method.[140] In the case of the Sn_3Pd bimetallic catalyst this material existed as alloyed material or bimetallic mixture. The aforementioned Cu/Pd and Cu/Ni electrocatalyst segregated bimetallic catalyst reported XRD analysis indicative of pure metals coexisting on the same cathode, while for the Sn_3Pd catalyst researchers reported an alloy phase for three Sn_3Pd planes in the XRD analysis. In either case proper differentiation of both subclasses of materials will lead to better material development as new characteristics and benefits for these classes are being discovered and catalogued.

While a majority of the review focuses on product selectivity towards dinitrogen formation, catalyst, which achieve appreciable rates and selectivity towards ammonia should also be of interest. From an industrial perspective ammonia is one of the most common chemicals utilized for a wide variety of applications – agricultural, plastics, textiles, and pharmaceuticals.[189,190] In addition, this material shows much promise for a next generation energy carrier due to its high energy density (4.3 kWh kg^{-1}) and clean emission.[191] Traditional sourcing of ammonia comes from the energy intensive Harber-Bosch process which utilizes fossil fuels and hydrogen to drive artificial nitrogen fixation, resulting in 1% of global greenhouse emissions.[192] Therefore, being able to utilize nitrate polluted water as untapped source for the production of ammonia through electrocatalytic means, under mild conditions, has recently become of great interest.[190] A CuPd (3:1) bimetallic self-supported aerogel prepared by Y. Xu et al., expressed excellent selectivity towards ammonia formation (95.27%) via electrocatalytic reduction. This material contained networks of channels and pores providing abundant active sites to accommodate the transfer of

nitrate ions from the bulk solution to the aerogel interface. Introduction of Pd atoms on the surface is believed to tune the *d* band of the copper material to optimum (elevated) energies for the adsorption of nitrate, and related intermediates, at sites of Cu|Pd interaction.[193] The reduction mechanism was believed to occur by electrochemical reduction combined with hydrogenation where the Pd centers promoted adsorption of $H_{(ads)}$ that induced selective reduction.[193]

To summarize, the bimetallic electrocatalyst design has been proven to synergize the catalytic formation of both N_2 and NH_3 from nitrate polluted sources, while minimizing the reliance on PGM. This reduced need for PGM also decreases the cost for catalyst production and increases the probability for upscaled applications by this catalyst design. For segregated bimetallic catalyst Cu has been extensively used as a promotor because of its adsorption properties for nitrate ions, specifically on the Cu (100) plane, which drastically improves catalytic rates. The use of dual metal allows for a synergistic multifunctional surface, in segregated bimetallic catalyst, while in both varieties a combination of metals can alleviate interferences, tune binding energies, and accelerates the transfer of electrons.
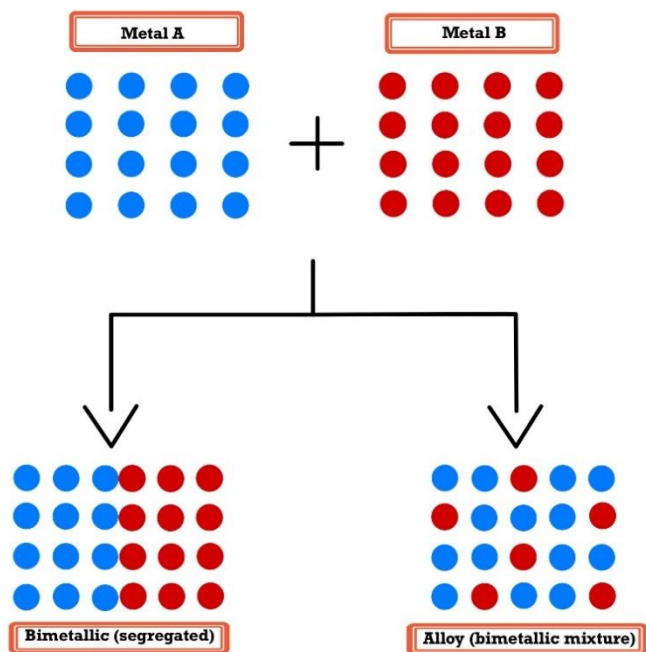
Figure 3.4: Differentiation of bimetallic and alloyed materials through the combination of two separate metals.
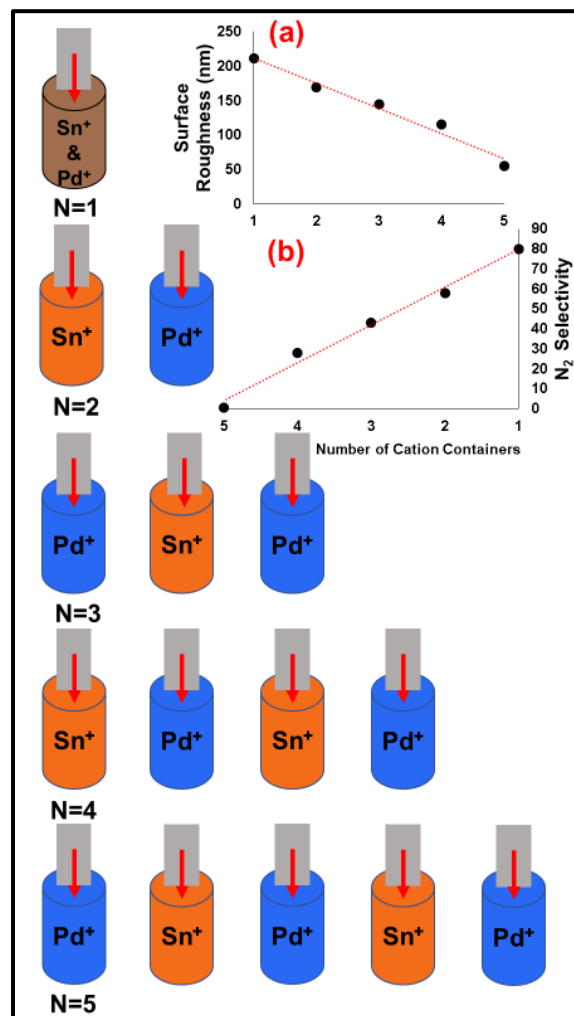
Figure 3.5: Variance in number of containers for the electrodeposition on palladium and tin ion in terms of surface roughness, inverse to crystallite size, (a) and product selectivity towards dinitrogen formation from the electrocatalytic reduction of nitrates (b). Adapted with permission from ref (193), Copyright 2019. Elsevier.

3.3 Graphitic composite electrodes for nano-enabling strategies and more

The use of graphitic materials as a support for catalytic nanoparticles has become a popular choice for creating hybrid catalyst with enhanced properties.[194] Pure graphene does not generate an appropriate electrochemical response to effectively reduce nitrate or its intermediates. However, graphite and graphene related materials are used as supports to enhance the properties of an assortment of catalytic nanomaterials (Rh, Pd, Pt, Cu, Fe). As supports, graphitic materials provide an effective scaffold for nanocatalyst while generating composite materials with substantial amounts of reactive surface area. In addition, the conductive nature of these materials helps boost the response of the electrocatalyst in terms of activity driven by the power source.

Examples of graphitic or graphite-based supports include graphene, graphene oxide (GO), reduced GO (rGO), activated carbon fibers, carbon black, mesoporous carbon, carbon paper, and carbon nanotubes (CNTs).[126,138,195–199] As supports, graphitic materials allow for a large magnitude of dispersed nano-catalytic sites that increases the fluid permeability of the composite material. The fluid permeability of these materials is directly correlated to the mass transfer of ions from the bulk solution to the electrode surface interface.[198] With a larger number of active sites (reactive surface area) the accommodation of greater number of nitrate ion on the electrode surface is made possible, which boosts catalytic activity. Many studies have concluded that an even dispersion of catalytic nanoparticles on the graphitic supports plays a role in improving reactivity and the overall reaction kinetics. A study by Wei Teng et al. exemplified excellent catalytic activity due to high surface area and even dispersion of nanocatalyst in a composite material. In this study, the authors utilized nanoscale iron encapsulated mesoporous carbon for the ERN. The iron-carbon material displayed a large surface area (660-830 m^2/g) with an even dispersion of nano iron particles (3-9 nm) over the surface. The hybrid catalyst reported a maximum removal capacity of 315 mg of N/

g of Fe with a 74% selectivity towards $N_{2(g)}$.[200] Duan et al., used a similar type of material, a N-doped graphitic carbon-encapsulated iron nanoparticle, which achieved 100% product selectivity towards N_2, in the presence of 1.0 g/L of NaCl over 20 catalytic cycles. The continued activity of the composite catalyst was attributed to the stabilization of the iron nanoparticles by the protective graphitic shells.[201] The results from the aforementioned cycling studies, corresponding SEM analysis, and a visual representation of the carbon-encapsulated iron nanoparticles can be seen in Figure 3.6.
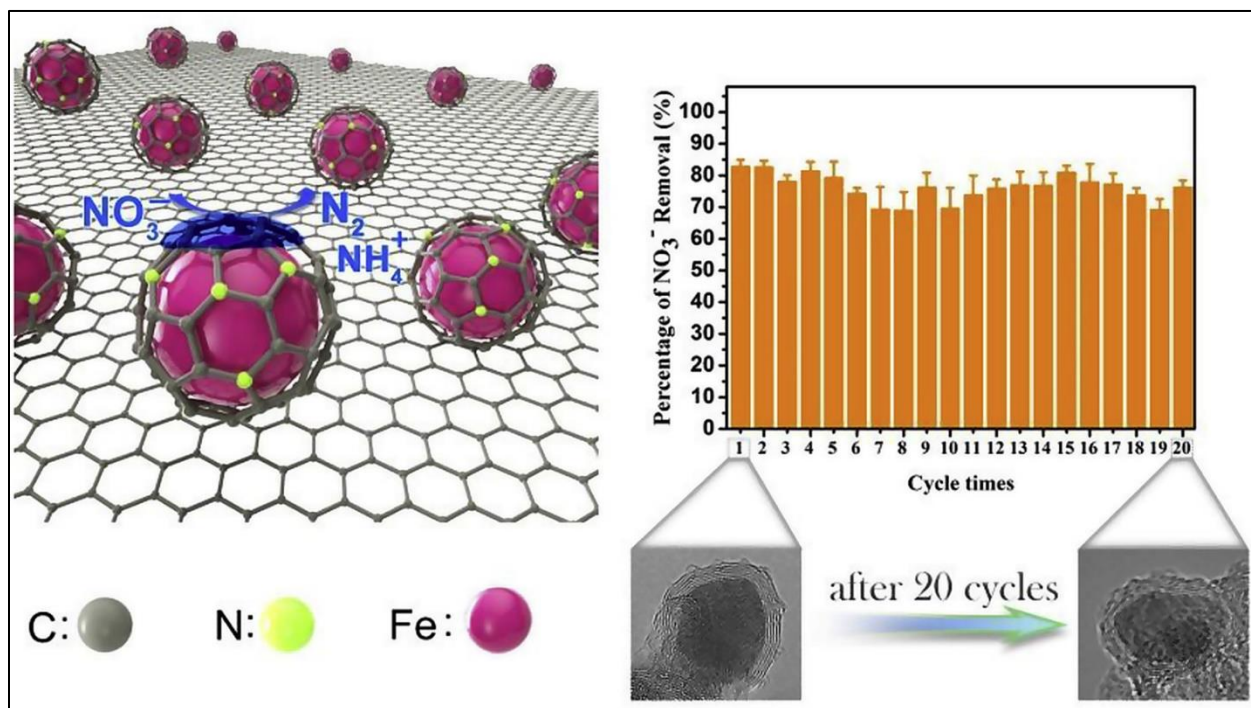
Figure 3.6: Visual representation of N-doped graphitic carbon-encapsulated iron nanoparticles (left), nitrate removal over twenty cycles with accompanying HRTEM imaging of the catalyst (right). Reprinted with permission from ref (201), Copyright 2019. Elsevier.

The supplement of Cl⁻ ions at the anode was thought to enhance breakpoint oxidation reaction at the anode responsible for converting remaining NH_4^+ and NH_3 to N_2.[202–204] Although these results are promising, the selectivity towards nitrogen is not defined by the electrocatalyst but driven by the chlorine-breaking point induced through electrochlorination.[205] Y. Shao et al. compared the

stabilizing effect of two graphitic materials, carbon black and CNTs, as supports for platinum nanoparticles. The CNTs achieved a greater level of composite stability due to better control of particle growth and increased resistance to electrochemical oxidation.[206] The conductive nature of these materials also helps with facile electron transfer at the electrode and in turn increased electrochemical performance.[197,198] Chen et al. reported a structure-function relationship between the conductivity of graphene paper and the degree of thermal treatment after synthesis. The authors showed as the temperature of thermal treatment increased so did the order between graphene layers. Electrical conductivity of the electrodes showed a liner relationship between conductivity measurements and the temperature of the thermal pre-treatment of the carbon support. The spacing between these graphene sheets was determined through XRD analysis which reported a decrease in the value for the d spacing, the reflection of the 002 plane of the graphene-based materials, as the temperature of thermal annealing increased.[207] In fact, the decrease of the carbon intralayer distance induced by the thermal treatment was described as the main cause for the enhanced electron transfer of the carbonaceous electrodes and the increased conductivity. Besides performance, these carbonaceous-based materials are of interest for electrochemical processes because of their low overall cost for certain varieties including carbon black (1 USD/kg) and carbon fiber (17 USD/kg).[86,208] When using graphitic supported catalysts, the majority of the electrode cost would stem from the synthesis of the catalytic nanoparticles (NP) themselves.

Recently, studies have reported that carbon doping can increase catalytic activity towards nitrate reduction. Doped carbon materials can be an alternative approach to using carbon as a support for metals and various nanoparticles. Heteroatomic doped carbon materials have the potential to become a lower cost alternative to graphitic supported catalyst. The doping of nitrogen atoms into the conjugated system of graphitic materials has been reported to enhance the overall

catalytic activity. The lone pair of electrons on the nitrogen atoms is thought to acts as a delocalized conjugated system which works in tandem with the sp^2 hybridized carbon frameworks. This interaction between the lone pair on the nitrogen and the sp^2 carbon atoms results in greater electrocatalytic performance and reactivity in electrochemical reductions.[209]   High reduction capacities for graphene quantum dots doped with both boron and nitrogen heteroatoms, have been reported by Huilong Fei and co-workers. The authors state that B and N doping resulted in hybrid material with a large number of catalytic sites resulting in better activities (1.1X) than Pt/C, with a greater positive (15 mV) onset potential vs Ag/AgCl reference, for the ERN. It is suggested that doping with both boron and nitrogen the hybrid material showed a synergistic coupling between these heteroatoms with the conjugated carbon backbone.[210]

Graphitic supported composites show much promise for the ERN applications for they reduce the amount of catalytic material necessary to achieve competitive levels of nitrate reduction. This catalytic activity stems of graphitic scaffold acting as a platform for well dispersed catalytic NPs, which can be synthesized in situ, which may also increase the durability of the catalytic sites. The conductivity of these materials helps with facile and efficient electrical current usage, which boost the overall electrochemical performance of these carbon-supported catalyst. Metal free varieties may also bridge a gap into a new class of low cost and nontoxic active materials for oxyanion reduction, but further research is required to elucidate the mechanisms associated to that enhancement.

3.4 Metal Oxide Electrodes as a new pathway for sustainable reduction of nitrate

Although bimetallic catalysts can decrease the use of PGMs, some of the most active forms still typically depend on small amounts of these expensive materials. Many research efforts to

move away from the use of PGMs have identified an alternative pathway through metal oxides as cost effective electrocatalysts.[162] Through the use of dopants to fine tune adsorption of species and accelerate the transfer of electrons, these materials have already been proven to be efficient even in real environmental samples. If demonstrated to be durable and stable these materials could provide a sustainable choice for electrocatalytic material for the remediation of nitrate from various water matrices.

Among metal-oxides, the study of transition metals has demonstrated excellent control over product selectivity. Metal oxides are semiconductor materials that can be doped with various atoms to increase their activity. These dopants commonly replace lattice oxygen with other species to better facilitate the transfer of electrons from the catalyst to the nitrate ions in solution and/or tune surface energies for the adsorption of target species. For example, Gao et al. prepared a phosphorus doped Co_3O_4/nickel foam electrode with a high rate for nitrate reduction. The Co_3O_4 has been used extensively as a cathodic material, for similar electrochemical processes (e.g., HER), due to the catalytic activity and durability of the Co_3O_4 catalyst. The controlled doping of Co_3O_4 catalyst with phosphorous provided by Gao et al. could offer a new perspective for an economically feasible non-PGM catalyst for large scale remediation of nitrate in drinking water. The phosphorous doping improved the activity of Co_3O_4 by replacing lattice oxygens resulting in a higher percentage of Co^{3+} and empty d orbitals. XPS data confirmed the higher Co^{3+}/Co^{2+} ratio in the doped catalyst suggesting lower electron density around the Co species. The higher Co^{3+}/Co^{2+} ratio was believed to led to increased adsorption capacity of H* species, which may enable simultaneous catalytic hydrogenation reduction mechanisms that can be utilized for the indirect reduction of NO_3^-.[211] This belief is consistent with the d-band theory that indicates empty antibonding orbitals of transition metals as favorable for hydrogen affinity.[212,213] This was further

confirmed with DFT calculations utilized to compute the energy of dissociation of H_2O to OH^- and H^* on the Co_3O_4 (311) surface of the doped and undoped surfaces. DFT calculations indicated a greater degree of thermodynamic favorability for the H_2O dissociation on the P-doped Co_3O_4 (311) surface [-0.73 eV] vs , compared to the pure Co_3O_4 (311) surface [1.86 eV], as illustrated in Figure 3.7.
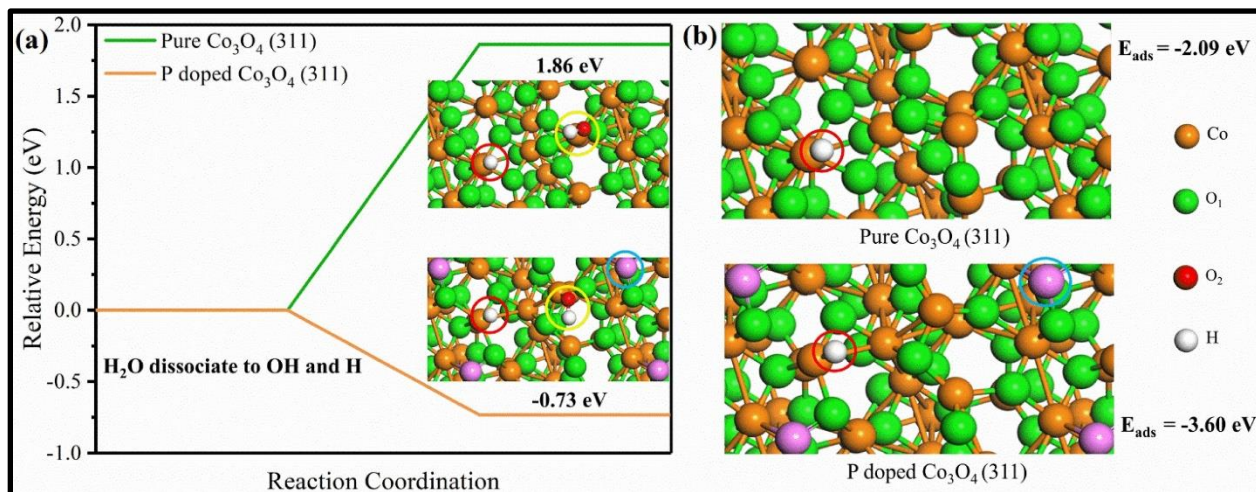
Figure 3.7: Energy for H_2O dissociation on the pure and P-doped Co_3O_4 catalyst (a) energy of H adsorption on both varieties as well as a visual representation of the phosphorous replacement of oxygen in the doped lattice (b). Reprinted with permission from ref (211), Copyright 2020. Elsevier.

In addition, the doped surface displayed a much larger energy of sorption (-3.60 eV) for H^* in comparison to the undoped surface (-2.09 eV) and even greater than PGM Pd (-2.88 eV). This led researchers to believe that reaction mechanism proceeded by a larger degree of indirect reduction through H^* on the doped variety due to inhibition of HER. Experimental studies done with tert-butyl alcohol (TBA) as a scavenger saw only saw a very minimal reduction (5%) in nitrate removal efficiency for the pure Co_3O_4 catalyst vs a 34% reduction in the presence of 5 mmol TBA. This theory was further proven by a much stronger peak intensity for electron spin resonance used to measure generation of the H^* radical. The phosphorous doped Co_3O_4 catalyst achieved complete removal of 50 ppm of NO_3^- in 120 minutes, which was 8.45x faster than the undoped Co_3O_4 catalyst, with nearly 100% N_2 formation when in the presence of 2500 mg/L of

chloride ions.[211] Chen Li prepared a Co_3O_4/Ti cathode that completely reduced 50 ppm of nitrate, within 150 minutes, with a specificity toward $N_{2(g)}$ formation but similar to the previous example this was only feasible in the presence of chloride ions. The Co_3O_4 electrocatalysts expressed selectivity towards ammonia, but ammonia specificity was shifted towards nitrogen gas by coupling the system with electrochlorination.[214] The yielded ammonia produced is oxidized to nitrogen gas through chemical oxidation by chlorine active species electrogenerated on the anode. For example, the use of CuO-Co_3O_4/Ti electrode had selectivity toward N_2 gas of 40.1 % that increased up to 94.0% when electrolysis was conducted in presence of 1 g/L of NaCl.[215] This same electrode material was employed in real environmental samples, which consisted of biological effluents from municipal wastewater, biological effluent of industrial wastewater from a chemical factory, and finally concentrate from an anion exchange process for nitrate removal (RC). Of the three environmental samples, the total nitrogen removal was largest for RC (78.5%) with a NO_3^- removal rate of 57.7 mg/$L^{-1}h^{-1}$. Interestingly, the RC sample showed the lowest energy consumption (2 x 10^{-4} kWh mg^{-1} TN) of the three environmental samples. Researchers attributed the high nitrogen removal efficiencies to high conductivity (1.8x10^5 µS/cm) and high concentration of chloride (9.83x10^4 mg/L) within this sample. The results of the aforementioned study exemplify the feasibility of this remediation technique in real environmental samples.[215]

Other examples of metal oxide electrodes used for the electrocatalysis of nitrate include Ni-Fe^0@Fe_3O_4 nanocomposite, Ni-TiO_2 nanotube array electrodes, and TiO_{2-x} nanotubes with oxygen vacancies. The Ni-Fe^0@Fe_3O_4 electrode achieved a high nitrate removal capacity of 90.2%, from a 50-ppm nitrate solution. The nitrate removal was achieved at a low current density (5 mA/cm^2) making for a low energy consumption process. In the presence of 10mM of NaCl,

$N_{2(g)}$ was the predominant product (88%), requiring 240 minutes to achieve approximately 90% nitrate removal.[150] The $Ni-TiO_2$ electrode was observed to achieve a similar removal capacity of 93.4% with the same initial concentration of nitrate (50 ppm) with 5.13mM NaCl, at pH of 11, under a current density of 30 mA/cm^2.[216] The faster nitrate removal attained with $Ni-TiO_2$ (almost complete after 90 min), when compared to $Ni-Fe^0@Fe_3O_4$, can be ascribed to the six times greater applied current density. Although the process was faster, the energy requirements were much greater. In addition, the optimized reaction conditions were observed to be pH 11 with a NaCl concentration of 5.13mM.[216] In this instance the aforementioned materials highlight the potential tradeoff between energy and time efficiency. The implementation of oxygen vacancies in metal oxides such as TiO_2 have been reported to boost selectivity and reactivity in materials utilized for the ERN[217]. These vacancies help increase the interaction between oxygen atoms in the nitrate ions and the oxygen vacant portions of the TiO_2 surface. Recent studies reported an increase in nitrate conversion (95.2%) to ammonia and higher levels of selectivity (87.1%) based on experimental findings for the oxygen deficient variety of TiO_{2-x} in comparison to the traditional TiO_2 (61.3% and 66.9% respectively) material. Density of state calculations determined higher adsorption energies for nitrate on the TiO_2 surfaces with more oxygen vacancies, which was a key factor in the ammonia synthesis. The oxygen atom of the nitrate ion fills this vacancy with a high degree of interaction, which destabilizes the N-O bond leading to a dissociation of oxygen through proton-electron attacks, generating ammonia and water molecules in the process. This paradigm for increasing nitrate interaction, while simultaneously destabilizing N-O bonding, could provide an efficient catalyst design for ammonia production form the ERN.

In summary, metal oxide materials could prove to be an economically favorable choice with no reliance on PGM materials for upscaled applications. However, studies should consider

comparable conditions for consistent benchmarking of performance. It is important to remark that when defining selectivity of the systems it should be referred to as the simple electrocatalytic performance without integrating the chemical action of chlorine (which can be implemented for any electrode material). Applicability of metal oxide cathodes in real environmental samples has been demonstrated and revealed the balancing act of performance (time efficiency) and energy consumption. The use of dopants to fine tune electron density, surface interactions, and selectivity can be a key aspect in the material engineering for this class of cathodic materials that should be further explored. Finally, the implementation of oxygen vacancies on the metal oxide surface could act as a lock and key approach for increasing nitrate interaction with the surface of electrocatalyst, boosting the overall catalytic process.

3.5 Metal Sulfides as upcoming generation of bio-inspired electrocatalysts

Biomimicry can inspire novel approaches and guide researchers towards unexplored materials and structures. Looking to natural processes of the nitrogen cycle it has been known that various forms of denitrifying bacteria are capable of reducing nitrate to nitrite and dinitrogen gas. These natural bioreduction processes are driven by specific enzymes such as nitrate reductase. Nitrate reductase sourced from *Desulfovibrio desulfuricans* ATCC 27774 (DdNapA) bacteria was isolated and crystalized for investigation of the components of the active catalytic site. Enzyme characterization studies identified that the molybdenum metallic active center of the enzyme was bound to six atoms, of which five were sulfur bonds. Originally the sixth molybdenum bond was thought to be an OH/OH_2 ligand. After the refinement of diffraction analysis parameters, it was concluded that this ligand was actually a sulfur atom. The S-S distance between the sulfur ligand and the Sγ atom of the molybdenum ligand CysA$_{140}$ (2.2-2.85 A°) was shorter than van der Waals

contact distance, indicating a partial disulfide bond.[218] This unexpected reactivity of molybdenum sulfide structures hint researchers towards the possibility of using chalcogenides such as MoS_2 as electrocatalysts. The MoS_2 has been utilized for a wide variety of electrocatalytic reductive applications – oxygen reduction, hydrogen evolution, and even N_2 reduction.[219–221] However, very few accounts of nitrate reduction by MoS_2 or any other metal sulfides have been reported. Metal sulfides, tellurides, and selenides have been heavily utilized for various electrocatalytic processes; therefore chalcogenides could serve as promising class of catalytic materials for the ERN.[222–225] A study by Yamei Li found that electrochemical reduction of nitrate/nitrite by a MoS_2 electrocatalyst lead to the formation of ammonia through a mechanism similar to biological dissimilatory denitrification. The MoS_2 catalyst was able to form ammonia from nitrate/nitrite over a wide pH range (3-11) occurring in a manner consistent with a concerted proton-electron transfer (CPET).[226] Results displayed a direct linear correlation to the necessary overpotential needed to reach a cathodic current density of 1.5 mA cm^{-2} vs the pH of the reaction solution are displayed in Figure 3.8a. This pH dependence confirms that the CPET-induced redox transition plays a key role in the activation of nitrate/nitrate reduction most likely through the formation of hydrogen bonds between the active site and substrate. Figure 3.8b also displays the proposed reduction mechanism for this process ending in either ammonium formation or N_2O . Results gathered from fundamental studies with differential electrochemical mass spectroscopy (DEMS,) determined that NO (m/z=31) began to form at a potential of 0.6 V vs Ag/AgCl, following the reduction of nitrite. As the potential continued to decrease so did the signal for NO accompanied by an increase in detected N_2O (m/z=46) down to a potential of 0.1 V. From 0.1 to -0.4 V ammonia formation prevailed along with the evolution of hydrogen (H_2). The authors found that the excellent activity displayed by the MoS_2 catalyst was comparable to TOF of the extant Mo-dependent nitrate reductases.[226] A

recent account of another metal sulfide (Rh_xS_y/C) electrocatalyst expressed activities greater than both Rh/C (1.6 - 5.6X) and Pt/C (10 - 24X) for the ERN between potentials of 0.05 - 0.15V vs RHE. The authors attributed sulfur vacancies in the Rh_3S_4 (100) facet to have a strong nitrate adsorption energy, and in turn low activation energy for the dissociation of nitrate ions on the aforementioned facet. Effects of chloride associated poisoning was also evaluated through a combination of experimental and calculated strategies. DFT-calculated adsorption energies, and microkinetic modeling, found that species that have a strong interaction for nitrate ions are also strongly attracted to chloride, leading to a competitive adsorption between the species. The Rh_xS_y/C electrocatalyst not only outperformed both the Rh/C and Pt/C competitors, but it also suffered a smaller degree of chloride poisoning, which is a ubiquitous species in many water remediation applications. As the previous metal sulfide example, the rhodium sulfide material expressed excellent catalytic rates for the selective formation of ammonia from the ERN.[227]
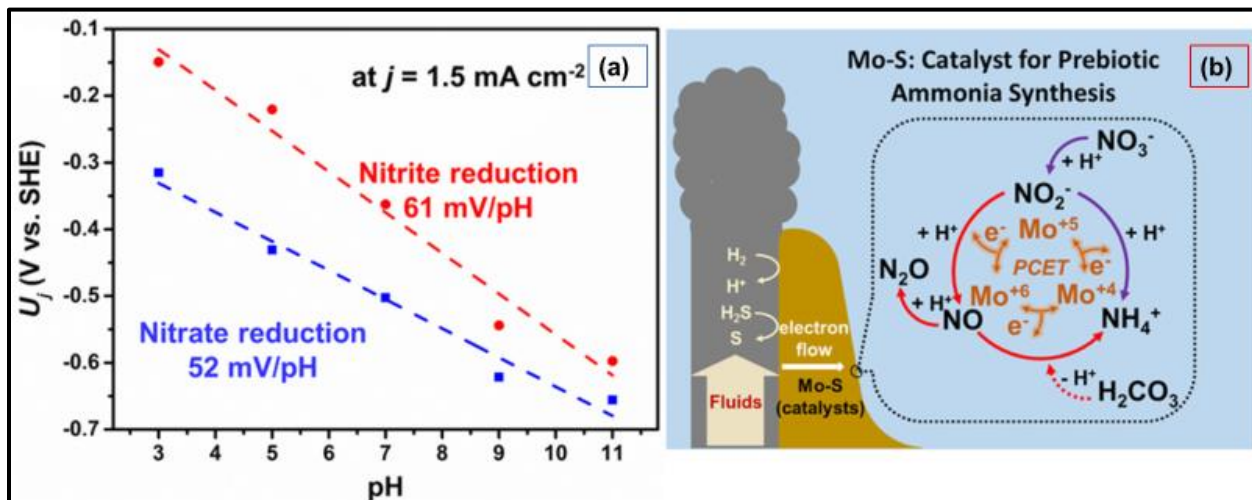
Figure 3.8: Relationship between the necessary overpotential needed to produce a cathodic current density of 1.5 mA cm^{-2} and the pH of the reaction solution (a). Proposed reaction mechanism for ERN gathered by DEMS analysis (b). Reprinted with permission from ref (226). Copyright 2017. American Chemical Society.

With these findings considered, it is clear that metal sulfide catalyst displays much promise for the reduction of nitrate and its intermediates. Exploring the effect of particle size, dopants, and

supportive materials could lead to important findings on the reactivity and product selectivity of the MoS_2 catalyst and other related metal sulfides. It has been known that the edge structures of MoS_2 are where the reductive activity stems from, therefore, nanosized particles could provide higher activity through larger ratios of edge sites to particle sizes.[228] Similar to other semiconductors (i.e., metal oxides), the incorporation of dopants could generate active sites on the basal plane, tune binding energies for nitrate ions and its intermediates, and influence the overall product selectivity.[229] Finally utilizing supports that enhance conductivity and dispersion could lead to synergistic effects boosting the overall capability of the MoS_2 catalyst.[138] In addition, carbon based supports and shells have been known to increase catalyst's resistance to electrochemical oxidation, which could greatly increase the lifetime and stability of the MoS_2 based electrocatalyst.[206,230] The large variety of metal sulfides as well as the vast possibility of combinations by additional metal dopants opens the door of a huge class of materials that could display intriguing characteristics for the ERN.[231] Other unexplored sulfide materials such as pentlandites can present interesting opportunities for nitrate and other oxyanions reduction.

4.0 pH and Coexisting Ions

4.1 The pH as master variable that secretly steers selectivity and productivity

The pH of the reaction solution plays a major role in the overall mechanism for the ERN.[161] Variations in pH of the reaction solution creates different chemical environments, which may be beneficial or harmful to the extent of electrochemical reactions. Species present in the reaction solution compete for adsorption sites on the working electrode, affecting the electrode's catalytic efficiency. In acidic media, H^+ competes with NO_3^- for adsorption sites on the cathodic surface. An effective cathodic material has the ability to accommodate the adsorption of multiple species, which may be necessary for the nitrate reduction mechanism as illustrated by the general

mechanism listed below [232] following adsorption of the nitrate anion from equation (5), (10) dissociation of water molecules, (11) adsorption of atomic hydrogen, and (12) indirect reduction of nitrate to nitrite. This mechanism is relevant when reduction is driven by coexisting catalytic hydrogenation faster than by direct charge transfer.

$$NO_3^-{}_{(aq)} \leftrightharpoons NO_3^-{}_{(ads)} \qquad\qquad Eq\ (5)$$

$$H_2O \leftrightharpoons H^+ + OH^- \qquad\qquad Eq\ (10)$$

$$2H^+ + 2e^- \rightarrow 2H_{(ads)} \qquad\qquad Eq\ (11)$$

$$NO_3^-{}_{(ads)} + 2H_{(ads)} \rightarrow NO_2^-{}_{(ads)} + H_2O \qquad\qquad Eq\ (12)$$
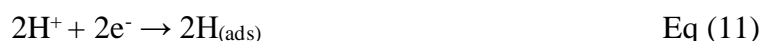
It was found that acidic medium can decrease nitrate electrocatalytic activity for platinum electrodes at low nitrate concentrations and potentials corresponding to hydrogen evolution reaction. The sluggish kinetics was associated to the hindered adsorption of nitrate. However, at high nitrate concentrations the reduction mechanism is impeded by adsorbed NO_3^- due to the lack of adsorption sites for hydrogen, necessary for the reduction of nitrate.[232]

For the competitive nature of hydrogen and nitrate adsorption researchers have conducted ERN experiments in alkaline conditions in order to minimize free hydrogen that could interfere with nitrate adsorption. In addition, it has also been proposed that having a large amount of adsorbed hydrogen affects the product selectivity towards ammonia formation rather than dinitrogen because NH_4^+-N forms easily when NO_2^--N reacts with H^+.[164,188] The surface charge of the catalyst is heavily influenced by the pH of the reaction solution, which directly affects the interactions of the catalyst with the species present in solution. This effect has been also observed in other redox-mediated processes such as nanoscale zero valent iron (nZVI) reduction of nitrate. In the case of nZVI it was found that nitrate reduction was severely impeded at pH's > 9. This inhibition was due to the accumulation of OH^- species on the surface creating a repulsive

interaction with nitrate ions. In addition, the eventual formation of iron hydroxide on the surface created a passivation layer which decreased the reactivity of the electrode interface with surface species.[233] The consumption of protons during electrocatalytic process in the presence of water results in increasing OH^- concentration, which in turn increases the pH of the reaction solution. Therefore, the final pH of the solution would need to be considered for various application of nitrate reduction. Ending at near neutral environment would minimize the need for post chemical treatment for drinking water applications, which can be easily attained by blending treated and untreated water while keeping the concentration of nitrate below MCL. For generating liquid ammonia as a resource recovery, it has been reported that maintaining a near neutral pH sustains produced ammonia in solution while allowing the pH to increase past 11 evolved ammonia gas.[214] For resource recovery maintaining the pH would be advantageous for producing enriched ammonia solutions, while the evolution of ammonia gas could lead to secondary production of ammonia hydroxide by saturating water with gaseous ammonia. Therefore, not only the initial but final pH for electrocatalytic process should be considered for the specific application this electrochemical technique will be utilized in.

4.2 Coexisting Ions

Performance of electrochemical treatment might be significantly affected by various water compositions.[234] While some ions might accelerate reduction kinetics and increase current efficiency, others might drastically inhibit the electrochemical treatment process.[235–237]

Katsounaros et al. reported that the presence of cationic species in 0.1 M X-Cl electrolyte (being X one of the alkali cations Li^+, Na^+, K^+, or Cs^+) increases the nitrate reduction rate in the following order $Li^+ < Na^+ < K^+ < Cs^+$.[236] The obtained data was attributed to the increasing association constants of nitrate with these cations in analogous sequence. The larger association

constants were related to the increased suppression of the electrostatic repulsion forces between nitrate and the cathode surface [157] and, consequently, accelerated kinetics. Ambrosioni et al. observed that the nitrate reduction kinetics in 0.5 M Na-X electrolyte (where X is one of the anions HCO_3^-, SO_4^{2-}, ClO_4^-, Cl^-) increases in the following order $HCO_3^- < SO_4^{2-} < ClO_4^- < Cl^-$. These reported results suggest that chloride is the most favorable electrolyte for nitrate reduction kinetics.[235] Furthermore, with appropriate selection of an anode material, the presence of coexistent chloride anions with nitrate during electrochemical nitrate reduction might be extremely beneficial for the ERN process. In particular, when the objective is to achieve the highest selectivity towards nitrogen gas [214] or disinfection through generation of chlorine active species.[238,239] During electrochemical processes, Cl^- is oxidized on the anode surface according to the reaction (13). The electrogenerated chlorine in aqueous solution disproportionates following reaction (14) yielding hypochlorous acid (HClO). The HClO is then in acid-base equilibrium with hypochlorite (ClO-) according to reaction (15) in function of pH as defined by the reaction pK_a value of 7.5.

$$2\ Cl^- \rightarrow Cl_{2(aq)} + 2e^- \hspace{4cm} \text{Eq (13)}$$

$$Cl_{2(aq)} + H_2O \rightleftharpoons HClO + Cl^- + H^+ \hspace{3cm} \text{Eq (14)}$$

$$HClO \leftrightharpoons ClO^- + H^+, pK_a = 7.5 \hspace{3cm} \text{Eq (15)}$$
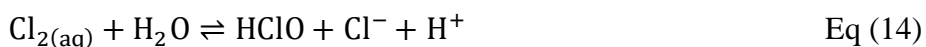
Reaction of chlorine active species with the ammonia containing compounds (including organic matter) leads, in the vast majority of cases, to the generation of chloramines which ultimately degrade resulting in the formation of N_2 and chlorine species.[240,241] When the nitrate reduction objective is the preferential formation of N_2 gas, the electrogeneration of chlorine aids in the oxidation of ammonia through the chlorine breaking point. This break point will only be feasible

when the molar ratio of Cl_2 to NH_3/NH_4^+ is greater than a value of 1.5, leading to generation of free chlorine and in turn active chlorine species as described by Figure 3.9.
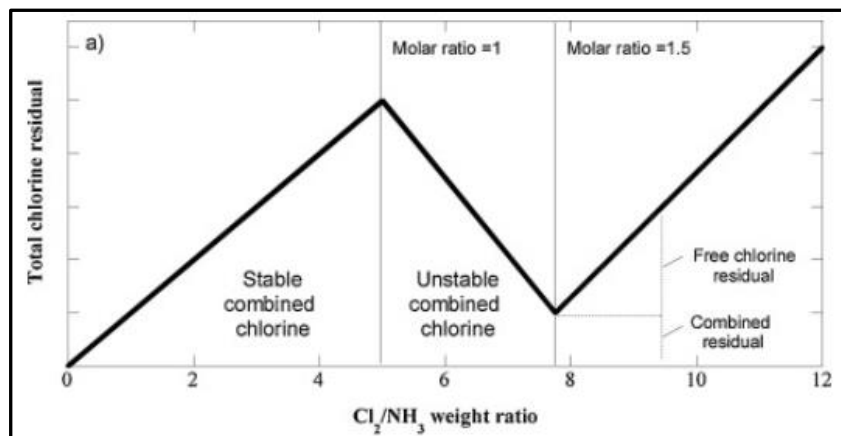
Figure 3.9: The molar ratio dependence of Cl_2 to NH_3 on chlorine breaking point, and the generation of free chlorine, active chlorine, species. Reprinted with permission from ref (242). Copyright 2012. John Wiley & Sons, Inc.

In addition to production of nitrogen, the intermediate stages of chloramines generation may yield disinfecting benefit for water treatment applications. In fact, recent works identify chloramines as a more favorable disinfectant than free chlorine since chloramines produce a smaller amount of undesired carcinogenic disinfection by-products.[242] Reactions (16), (17), and (18) describe the main processes induced by chlorine oxidation when reacting with free ammonia.

$$NH_3 + HOCl \rightarrow NH_2Cl + H_2O \qquad \text{Eq (16)}$$

$$NH_2Cl + HOCl \rightarrow NHCl_2 + H_2O \qquad \text{Eq (17)}$$

$$NHCl_2 + HOCl \rightarrow NCl_3 + H_2O \qquad \text{Eq (18)}$$

If the main objective is to reach the complete abatement of N-species as innocuous nitrogen gas, the chlorine breaking point approach can achieve such goal. As described in Figure 3.9, when optimum ratio of active chlorine species per ammonia content is reached, ammonia is effectively oxidized preferentially to nitrogen gas following general reaction (19). As a result, continued

generation of chlorine active species will easily convert combined chlorine species (i.e., chloramines) into nitrogen gas.[241,243,244]

$$2\ NH_3 + 3\ HOCl \rightarrow N_2 + 3\ HCl + 3\ H_2O \qquad\qquad Eq\ (19)$$
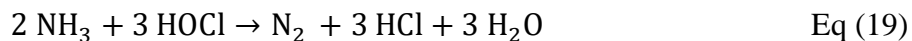
Thus, many electrified processes can benefit from the use of chlorine breaking point to ensure complete removal of nitrate by the consecutive reduction of ammonia and oxidation of chlorine leading to the formation of chloramines, which then induces nitrogen gas production. Please see Figure 3.9.1 for a representation of the concerted electrochlorination method for N_2 formation. On the other side of the coin, one critical aspect that is severely misunderstood when reporting selectivity of an electrocatalytic process is the source of such selectivity for the desired product. Fundamental studies that evaluate selective transformation induced by charge transfer or catalytic hydrogenation at the interface should report selectivity of the products based on the outcome in absence of chlorine. Experiments conducted in chloride media and undivided cells show biased results in terms of selective evolution of N_2. This selectivity is not induced by the catalytic conversion at the interface but rather by the chlorine oxidation in the bulk of the solution. Combination with chlorination is not a novel concept since it has been thoroughly reported in literature but should be clearly differentiated when trying to understand fundamental mechanisms induced at the vicinity of the electrode surface. In addition, recent accounts have found that chloride poisoning is a persistent issue for some platinum group materials (Rh and Pt) in the ERN. In the same study, the chloride poisoning was much less pronounced in the metal sulfide variety (Rh_xS_y) rather than the pure PGM. Considering the ubiquitous nature of chloride in wastewaters this could bring another solid point for the replacement of PGM, with more robust options, in applications of real wastewater remediation.
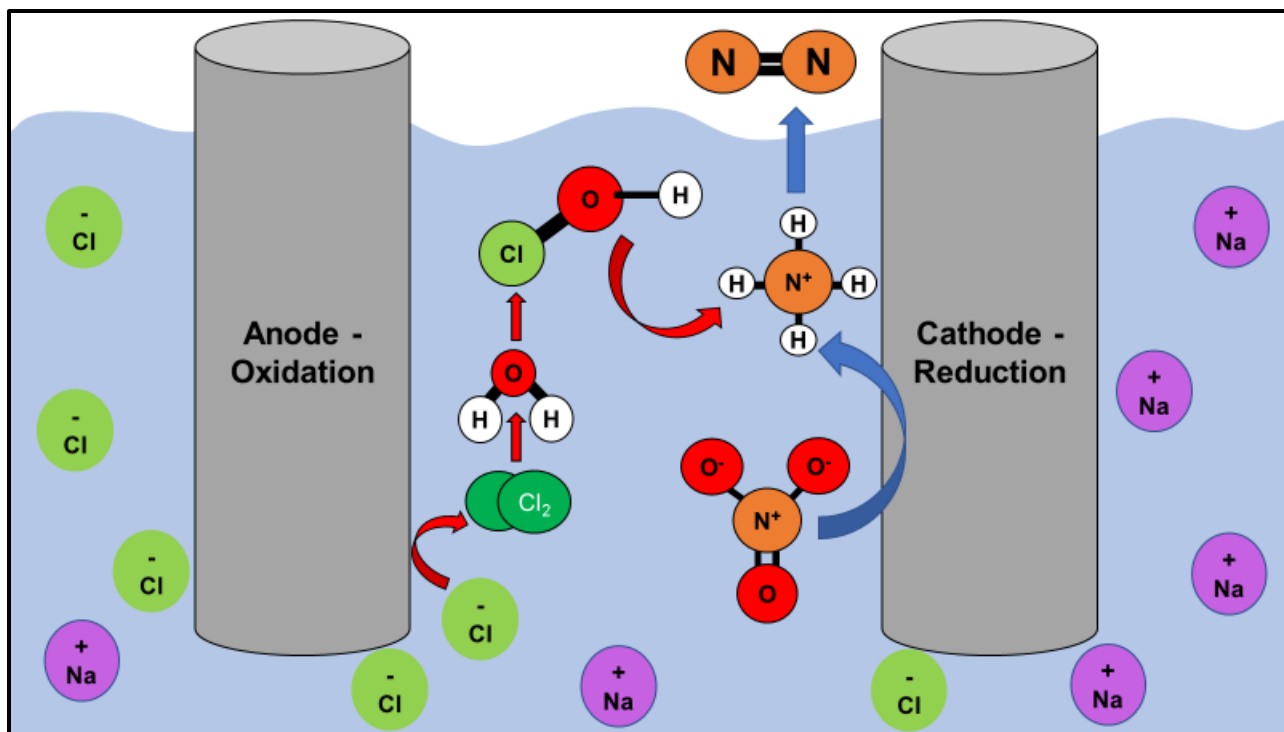
Figure 3.9.1: Condensed electrochlorination mechanism resulting in the formation of dinitrogen from ammonium produced at the cathode reacting with hypochlorous acid produced through oxidation of chloride at the anode.

The produced brine waters after reverse osmosis have high concentrations of both chloride and nitrate.[245] In addition, brine is extremely conductive, which makes it an ideal candidate for electrochemical nitrate reduction. These conditions present an excellent case scenario for electrochemical application. However, brine waters have a significant amount of other ions that may suppress conversion of nitrate into nitrogen gas. The high content of alkaline earth metals, which have affinity to coordinate with species such as hydroxides and carbonates might be a challenging step to overcome in order to succeed in electrochemical treatment. The cathode surface during electrochemical nitrate reduction has a large concentration of hydroxides due to electrolysis of water (10) and the nitrate reduction itself.

$$H_2O \leftrightharpoons H^+ + OH^- \qquad \qquad Eq~(10)$$

Moreover, real waters have a high content of HCO_3^- under neutral pH. Approaching the cathode surface with high hydroxide content, CO_3^{2-} will become the predominant form among carbonate species (20) in the vicinity of the electrode.

$$HCO_3^- + H_2O \leftrightharpoons H_3O^+ + CO_3^{2-}, pK_a = 10.3 \qquad \text{Eq (20)}$$

The coexistence of ions responsible for water hardness such as Ca^{2+} and Mg^{2+} with hydroxides and carbonates unavoidably will produce scaling on the basic cathode surface (21,22).

$$CaCO_3 \rightleftharpoons Ca^{2+} + CO_3^{2-}, pK_{sp} = 8.34 \qquad \text{Eq (21)}$$

$$Mg(OH)_2 \rightleftharpoons Mg^{2+} + 2\ OH^-, pK_{sp} = 10.7 \qquad \text{Eq (22)}$$
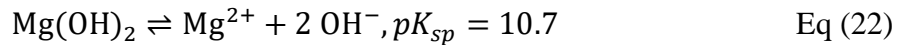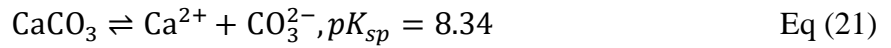
The formation of solid incrustations on the cathode surface may inhibit transport of nitrate towards the electrocatalyst and decrease the transformation rate and performance. Ma et. al. reported that partial removal of Ca^{2+} and Mg^{2+} ions led to elevated removal efficiency for electrochemical nitrate reduction.[237] The water hardness may be an essential water quality parameter to consider when exploring catalytic reduction of nitrate since may affect the long-term performance of any system deployed in real conditions. Electrode polarization inversion can contribute to prevent some undesired scaling due to the interfacial pH acidification during water oxidation reaction. Figure 3.9.2 depicts scaling formed on an electrochemical system after conducting long term treatment of a very hard water under continuous flow operation without inverting electrode polarization.
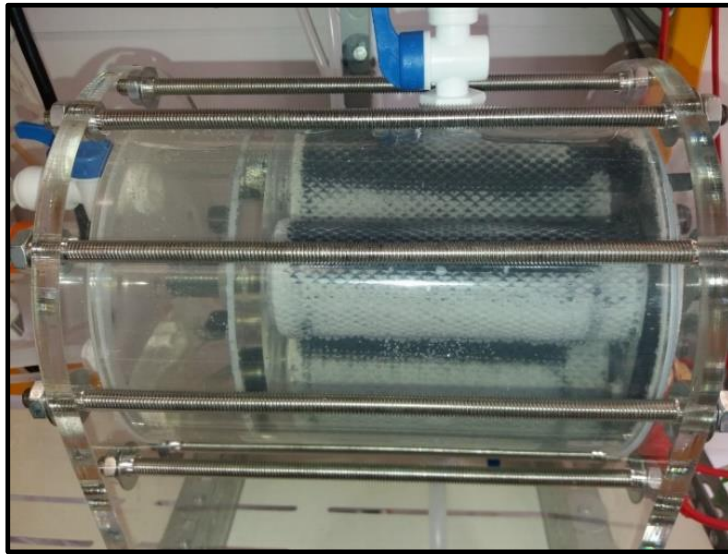
Figure 3.9.2– Precipitation of inorganic salts on the cathode surface under continuous operation to treat a very hard real groundwater (hardness: ~350 mg L^{-1} as CaCO$_3$).

5.0 Electrode Stability – considerations for aging and fouling of cathode materials

Electrocatalytic processes are heavily influenced by the structure and characteristics of the electrode – electrolyte interface. Changes to the nanoscale structures of an electrode can alter the chemical reactions occurring at said interface. Throughout the lifetime of the electrodes changes to surface structures and components may alter reaction mechanisms, product selectivity, and the overall energy metrics for the electrochemical process.[246] Electrode stability normally refers to consistent performance over a pre-determined period. Performance is related to maintaining a consistent energy consumption to produce an equivalent number of products after every catalytic cycle. From a laboratory standpoint, this could entail a 20-cycle analysis to compare performance and structure of the electrode before and after the catalytic cycles. However, for industrial and scaled up applications this stability is in a completely different scale. Considering analogies with electrochemical energy generation systems, the Department of Energy requires at least 5000 hours of stable and consistent performance for cathodes utilized for fuel cells.[247] The resilience of water

treatment systems that are operated non-stop (24/7) should consider similar if not more stringent requirements. Hence, the overall stability of electrocatalysts for the reduction of nitrates is vital to the upscaling of this technology for commercial and industrial water purification.[164,248] The stability of cathodic components will be outlined by distinct, yet related process termed as aging and fouling. The process of electrode aging refers to surface and composition modifications arising from the wear and tear of the electrochemical process, which diminishes performance in an irreversible manner. Fouling is the formation of unwanted materials on the surface of the electrode, which inactivates catalytic sites by isolating the electrode from the target species. This process may be reversible or semi reversible depending on the interaction of the scale and the electrode surface.[217] The following discussion is guided by research for similar electrocatalytic reductive processes, which have developed further understanding of variables and mechanisms leading to the aging and fouling of electrode materials.

5.1 Cathodic Aging

Cathodic aging refers to irreversible changes brought forth to the cathodic material during its lifetime, as the result of wear and tear of electro/chemical reactions. Measuring this process is typically accomplished through monitoring the activity of the electrode or system, but the progression of this aging is notable by changes in structure and composition of the surface of the electrode/catalyst. A common process occurring during the aging of cathodic materials (reductive electrode) is the dissolution of the metals from the electrode surface induced by cathodic corrosion – also termed as metal leaching. This can occur through spontaneous reactions taking place on the surface of the electrode (chemical dissolution) or through reactions driven by an applied potential (electrochemical dissolution). The loss of metal components from the surface of the cathode may exacerbate further changes such as pitting and other various types of corrosion.[249] The degree of

98

metal dissolution depends on the components of the electrode as well as its interaction with the electrolyte and other coexisting ions. Studies have investigated the difference in dissolution behaviour for reductive electrodes in various pH's to elucidate the mechanism for dissolution.

The effect of pH on electrode stability has been thoroughly studied for Co_2P electrodes utilized for hydrogen evolution reaction, researchers reported a difference in material dissolution in acidic (0.5 M H_2SO_4) and alkaline (1.0 M KOH) conditions. Following 2000 cycles of linear sweep voltammetry (LSV), the Co_2P electrodes were analysed by energy dispersive X-ray spectroscopy (EDX) to investigate their elemental ratios. Analysis of pristine Co_2P electrodes resulted in a Co:P ratio of 2.0 ± 0.1, which was consistent with XRD and Raman analysis for the Co_2P phase. This ratio was altered to 1.8 ± 0.1 in acidic and 2.2 ± 0.1 in basic conditions. The authors suggested a higher degree of Co dissolution in acidic rather than basic conditions, yet this material maintained its catalytic activity in acidic conditions. ICP-OES analysis of the reaction solution, following electrochemical test, revealed a stoichiometric level of both Co and P in the 0.5 M H_2SO_4 electrolyte. This led researchers to believe the leaching of Co & P occurred via chemical dissolution in the acidic media. In basic conditions is seemed phosphorous was preferentially dissolved while the exposed Co formed $Co(OH)_2$ in the OH- rich environment, which drastically decreased the HER activity.[250] This decrease in activity arose from the formation of a non-reactive surface layer in a process termed electro passivation. For the same electrochemical reaction (i.e., HER), a nickel – molybdenum electrode showed an opposite trend with pH and metal dissolution. In a KOH electrolyte it was observed that molybdenum expressed appreciable dissolution resulting from interaction with hydroxide to form molybdate through the following reaction:

$$Mo + 2\ OH^- + 2\ H_2O \rightarrow MoO_4^{2-} + 3\ H_2 \qquad\qquad Eq\ (23)$$
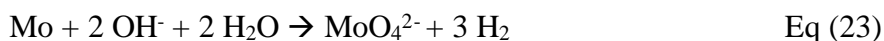
The Mo dissolution led to an increase in surface area through apparent roughening (increased surface roughness). Decreasing the pH of the reaction solution diminished available OH^- species in solution and in turn decreased the amount of Mo leaching during electrochemical testing.[251] In addition to testing the dissolution behaviour in basic vs acidic conditions, researchers tested the effect of various cation pairs for the following bases: KOH, NaOH, and LiOH. Figure 3.9.3 displays data for the XPS analysis of elemental ratios at 660 nm beneath the surface of the Ni-Mo cathode the following 24 h of electrocatalysis in the basic electrolytes. At the initial concentrations of the XPS analysis the elemental ratios of Li, Na, and K was 85%, 47%, and 20%, respectively. These results confirmed that the smallest degree of Mo leaching occurred with LiOH as the electrolyte. It was reasoned that Li^+ ions penetrated the alloy structure the furthest stabilizing the segregation of Mo on the surface of the alloy. The different degree of elemental insertion can be explained by the atomic radios of the alkali metals, being preferentially inserted the one with smallest atomic radii (Li^+), clearly showing the highest cation surface concentration following a full day of electrocatalysis. Figure 3.9.3b displays a schematic representation of surface MoOx species before and after electrocatalytic testing in the various basic electrolytes with LiOH maintaining the highest degree of surface Mo species.
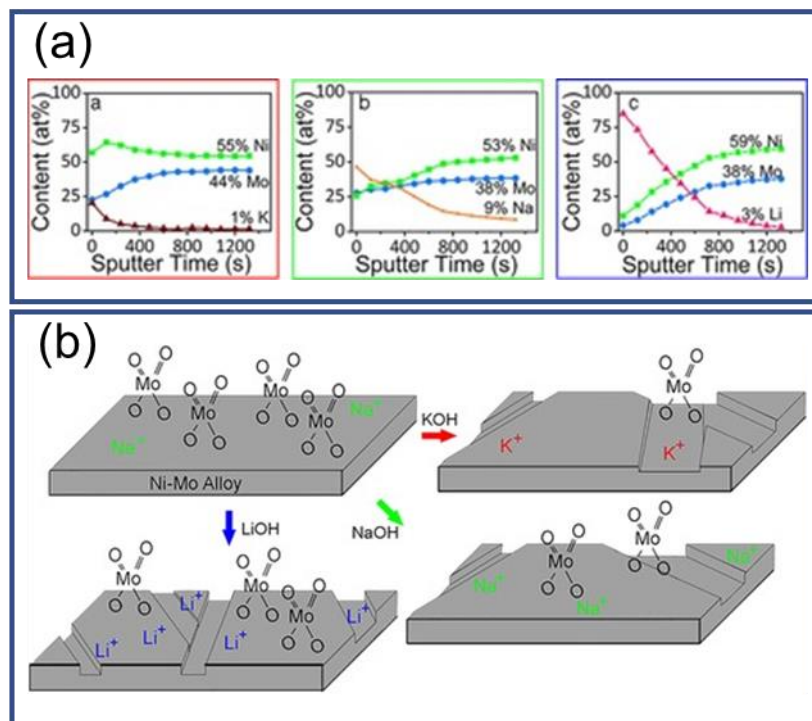
Figure 3.9.3: Elemental ratios at a depth of 660nm into the electrocatalyst surface determined by XPS analysis following 24 hours of electrocatalysis (a). Schematic of Mo leaching from Ni-Mo alloy during HER catalysis – top right is species before and (following the arrow) after catalytic cycling accompanied by the infiltration of monovalent cations (b). Reprinted with permission from ref (251) with added blue borders. Copyright 2019. Wiley-VCH. https://creativecommons.org/licenses/by-nc-nd/4.0/

In addition to metal dissolution another component of cathodic aging includes structural cracking or fracturing which can lead to isolation of the active materials from the applied potential.[252] The insertion of atomic hydrogen into metals and alloys during electrocatalysis can induce damage via recombination of atomic hydrogen into gaseous molecular hydrogen (H_2) which is also known as hydrogen embrittlement. Adsorption of atomic hydrogen occurs at defects at the crack apex resulting in a conversion from atom surface energy into tensile force.[253] The insertion of hydrogen may also occur before electrochemical testing begins during the synthesis of the active cathodic materials. This is due to the fact that hydrogen has a higher solubility in the liquid state rather than the solid state. As the hydrogen species permeate into the lattice of cathodic materials, they tend to accumulate into interstitial defects of the lattice.[254,255] These accumulated atomic hydrogen species may cause structural damage by combining with other adsorbed

101

hydrogen, during electrochemical testing, to form hydrogen gas ($H_2(g)$). Atomic hydrogen can also react with metal ions in cathodic components to form brittle metal hydride species furthering structural instability.[253] In order to mitigate structural damage brought forth by hydrogen permeation such techniques as alloying, microstructural engineering, and shot peening have been reported to increase materials resistance to hydrogen induced damage. Alloyed molybdenum species have reported to express excellent resistance to hydrogen damage via adsorption of molybdate species on its surface. This protective barrier of molybdate species decreased hydrogen insertion and in turn hydrogen induced damage. Microstructure engineering of surfaces is intended to create reversible traps for hydrogen species. These traps are microstructure sites (grain boundaries, vacancies, and interface between the matrix and particles) which concentrate the accumulation of hydrogen in these areas reducing the diffusion of hydrogen throughout all the interstitial lattice sites.[256] Shot peening refers to surface modifications made by controlling the energy of impacts made to the surface of a material. These impacts are thought to create an almost uniform compressive residual stress distribution along the surface of a material, which increases fatigue strength and reduces the likely hood of crack propagation in cathodic materials.[257]

In addition to hydrogen-induced aging, structural damage of cathodic materials may be brought forth during the intercalation/deintercalation of target species and products during electrochemical reactions.[252] This damage results from stress (external force acting on a solid area) leading to the eventual strain of the cathodic materials. The applied strain on the cathodic system may actually dislocate the lattice, seriously changing/damaging the electronic structure of the material.[258] Volume changes at the surface and subsurface of cathodic materials, occurring during the intercalation/deintercalation of ions, is thought to be the driving force of strain occurring during

this process.[259] The aforementioned variables of cathodic aging must be considered when evaluating the overall cathodic stability for electrocatalytic systems.

5.2 Cathodic Fouling

Fouling results from the binding of undesired species on the surface of cathodic materials can generate insulating layers. The fouled layer prevents nitrate ions from interacting with the surface of the electrode and decreases electrocatalytic performance. Preventing the physical contact of the analyte from the electrode surface hinders the electron transfer needed to generate an electrochemical response/reaction.[260] The increased resistance generated from the physical barrier, foulant layer, also increases the electrical cost of operating this technology. The identity of the foulants range from inorganic, organic, and biological means depending on the matrix of the nitrate polluted water.[261] The formation of inorganic salts would be of concern for hard water matrixes containing large amounts of calcium and magnesium ions for the formation of $Mg(OH)_2$ and $Ca(OH)_2$ could severely isolate the cathode from the reaction solution, as previously stated . Formation of other common salts in water remediation would include gypsum ($CaSO_4 \cdot 2H_2O$) and calcite ($CaCO_3$) which could potentially insulate the reactive surface of the cathode.[262] Adsorption of natural organic matter (humic substances, proteins, and polysaccharides) could also contribute to fouling concerns in treatment of waste and natural water sources. In addition to the previous stated classes biofouling would be another major category of harmful fouling induced by the accumulation of microorganism and other biological species.[263] Once microorganisms bind to the surface of a material, they tend to generate biofilms in which cellular communities generate an additional protective layer through the extrusion of an extracellular polymeric matrix.[264] This polymeric matrix makes removal of the foulant even more arduous. Finally, these biofilms can

induce corrosion of the electrode surface by changing the local chemistry near the metals' surface.[265]

These aforementioned foulants deposit onto the electrode surface in specific structural features areas such as grain and edge features where favorable interactions occur between the foulant and the cathode. These interactions include electrostatic, hydrophobic, and hydrophilic interactions, which depend on the chemistry occurring between the cathode surface and the foulant species.[266] Hydrophilic interactions tend to express a higher degree of reversibility than hydrophobic interactions, because hydrophilic and electrostatic interactions are occurring with the solvent, electrode, and analyte simultaneously. Polar solvent such as water will participate in these interactions through hydrogen bonding and electrostatic forces.[267,268] Adversely foulant formation on hydrophobic surfaces tends to occur in an irreversible manner. During electrochemical processes, the binding of foulants to hydrophobic surfaces is entropically favored in aqueous electrolytes. Reason being that water molecules are released from solvation shell allowing for exclusive interactions between the hydrophobic electrode and the foulant species.[268]

In order to combat electrode fouling, such approaches as chemical cleaning and electrode self-cleaning (*in situ*) have been reported in recent years as successful measures against foulant formation on electrode surfaces.[217,269,270] Nonchemical approaches would include physical cleaning by generation of microbubbles or aeration of the electrode surface. Physical cleaning would be an option for reversible foulant formation but would prove ineffective for irreversible fouling.[271] Instead, chemical cleanings and self-cleaning technology would provide a better alternative for irreversible foulant formation. Chemical cleaning has proven effective by addition of chemicals (e.g., HCl, CH_3COOH, NaOCl, etc.) that produce reactive intermediates which degrade foulants, but this requires halting the electrochemical process for modification of the

104

reactor in order to initiate the cleaning process.[272] Self-cleaning approaches seem to stand out as the best route of foulant control for long term or continuous remediation processes. Mechanisms for self-cleaning cathodes would include repulsion of negatively charged foulants, *in situ* generation of radicals, and polarity reversal. In oxygen rich environments the reduction of O_2 can produce oxidating agents (OH^-, H_2O_2) which can degrade organic species on the surface of the cathode. If chloride species are in the vicinity of the anode this could provide break point chlorination producing free chlorine species which can further reduce the concentration of organic materials that could foul the cathodic component of the system.[273] Reversing the polarity of the cathode – anode system has also been reported to reduce fouling on both electrodes, but this approach seems to have conflicting outcomes, which tend to be material dependent. A study by Chow et al. found a great reduction in fouling after polarity reversal on aluminum electrodes utilized for electrocoagulation; yet the same reversal was detrimental to iron electrodes which observed a crash in performance and no change in the degree of fouling. In both cases pitting and corrosion occurred following polarity reversal, catalyzing the aging process for both electrode compositions.[274] Unfortunately, very few studies exist in literature on the understanding and prevention of aging and fouling as it pertains to ERN technologies. The competitiveness of electrochemical systems will depend on the long-term stability of electrodes highlighting the urgent need for these considerations which are vaguely addressed in literature. The placement of electrochemical systems in the process of treating drinking water may also have a major role in the extent of aging and fouling occurring to said system, with a higher propensity for stability in a downstream placement ~ refined matrix.

6. Key Perspectives -

ERN is a promising remediation technology for transformation of nitrate pollution to innocuous or/and added value products. Nitrate can be selectively reduced by electrochemical means to dinitrogen for drinking water applications or ammonia as a resource recovery for industrial applications. Traditional treatment of nitrate ions from water (ion exchange and reverse osmosis) do not remediate these toxic ions, but rather concentrates them to a secondary stream resulting in high operational costs and further environmental risk. In addition, ERN technologies can operate under low operational costs, scalable designs, and can attain highly selective product formation under mild operating conditions. To be considered competitive with existing technologies the development of low-cost high-performance cathodes must be furthered in order to establish ERN as an economically favorable process, and a greener approach to nitrate remediation.

PGM materials were highly utilized in past studies as cathodic components due to their catalytic activity and corrosion resistance, but the price of these metals makes widespread adoption of ERN impossible. Therefore, cheaper and more sustainable alternatives must be identified and stringently tested to give further knowledge over reaction mechanisms and governing variables that could occur in real environmental samples. As a surface-controlled process, the interaction of the nitrate ions and the electrocatalyst surface is paramount for the ERN. The incorporation of vacancies in metal oxides has been a successful approach for increasing this interaction while destabilizing the oxygen-nitrogen bond in nitrate, once absorbed onto the catalyst surface. Bimetallic configurations for ERN cathodes have found that combining specific metals allows for the tuning of surface energies and in turn attraction to pollutants. The modification of Cu surfaces with inclusions of other nano metals (Pd, Pt, and Ni) has been known to tune the d band of the Cu

106

electrocatalyst to have a higher degree of interaction with the nitrate ions. In such an approach the mass requirement for the PGMs can be severely reduced bringing down the overall cost of the electrocatalyst, which is similar approach utilized by graphitic composite cathodes. In these composites the graphitic support acts as a highly conductive scaffold for the effective dispersion of catalytic nanoparticles. This culminates to a catalytic design with low mass requirements for the catalyst, boosted reactive surface area, and typically improved kinetics against the unsupported variety. In addition, graphitic support has been thought to stabilize metal centers from REDOX stresses, while providing increased fluid permeability to maximize interactions with species in the bulk solution. Interaction with other prevalent species such as hydrogen has been another focus for studies looking to optimize electrocatalyst activity for ERN. Specifically, the incorporation of phosphorus dopants in metal oxide catalyst has been recognized to increase the degree of interaction with absorbed hydrogen, which can be utilized for indirect reduction of nitrate. DFT calculations coupled with experimental studies revealed that suppression of HER activity, through increased interaction with *H, led to a greater access of indirect reduction. While both direct and indirect reduction proceeded the P-doped Co_3O_4 mechanism, ammonia was the main product for this process. The straining of metals with minor incorporation of subsurface oxygen has also been known to suppress HER while simultaneously increasing ERN activity. The degree of interaction with *H and the strained surface increases the energy requirements for H_2 dimerization resulting in a catalytic activity greater than the Haber-Bosch process. Finally looking to nature for inspiration molybdenum disulfide has been recognized as another possible candidate for a high-activity, low-cost material. MoS_2 is known to be the active component in catalytic sites found in denitrifying bacteria within the environment. MoS_2 and other metal sulfides (e.g., CoS_2) have been

extensively utilized in other electrocatalytic applications and have also been known to express resistance to various forms of catalytic poisoning.

In addition to the choice in catalyst, the pH and coexistence of ions can have a measurable effect of the rates and selectivity of ERN. Changes in surface charge related to the reaction pH should be highly considered since ERN is a surface-controlled process. Competition for adsorption between hydrogen and nitrate ions has been presented as an issue in previous studies. In either case the production of OH^- species at the cathode results in alkaline conditions during the electrocatalytic process. In hard water formulations(Ca^{2+} & Mg^{2+}) the abundance of hydroxyl species can induce scaling on the cathodic surface through production of $CaCO_3$ and $Mg(OH)_2$, which can insulate the cathode and diminish the electrochemical performance of the system. In addition, the formation of foulants has been known to create a similar effect, through physically separation of the active surface of the cathode from ions in solution. Foulants vary from organic species to microorganisms and depend on the matrix of the nitrate polluted water. Chemical cleaning, physical cleaning, and self-cleaning methods have been known as successful approaches to combat the formation of scalants and foulants. Conversely, chloride ions have been known to have a beneficial effect for undivided cells. The oxidation of chloride at the anode creates active chlorine species that may further react with ammonia produced at the cathode to generate chloramines that eventually decompose into N_2 gas. The added benefit of chloramine production induces disinfecting benefits for water treatment application, which may reduce foulant formation occurring during treatment. The caveat to this added benefit would be the implication of constant generation of active species near metal components. These species could induce irreversible changes such as metal dissolution at the cathode surface referred to as cathodic aging. The dissolution of metals could trigger further aging process such as crack propagation which could

108

isolate certain areas of the cathode or induce further metal loss. In order to combat this such practices as shot peening, alloying, and microstructural engineering have been identified as effective measures to prevent aging and achieve long term electrochemical treatment.

In summary, identifying abundant and low-cost materials for the ERN will be essential in making an economically favorable approach for the remediation of nitrate from polluted waters. The price and longevity of these materials will be crucial as the technology readiness level increases to larger scale applications. Catalyst, which produces rapid and constant formation of NH_3/NH_4^+ and N_2, will be of high importance as various classes of materials are being identified as a successor to PGM. Research advances should focus on alternative material identification and design of operational systems that sustain long term treatment and continuous operation.

Figure 3.9.4 -Graphical representation of applications for the electrocatalytic remediation of nitrate
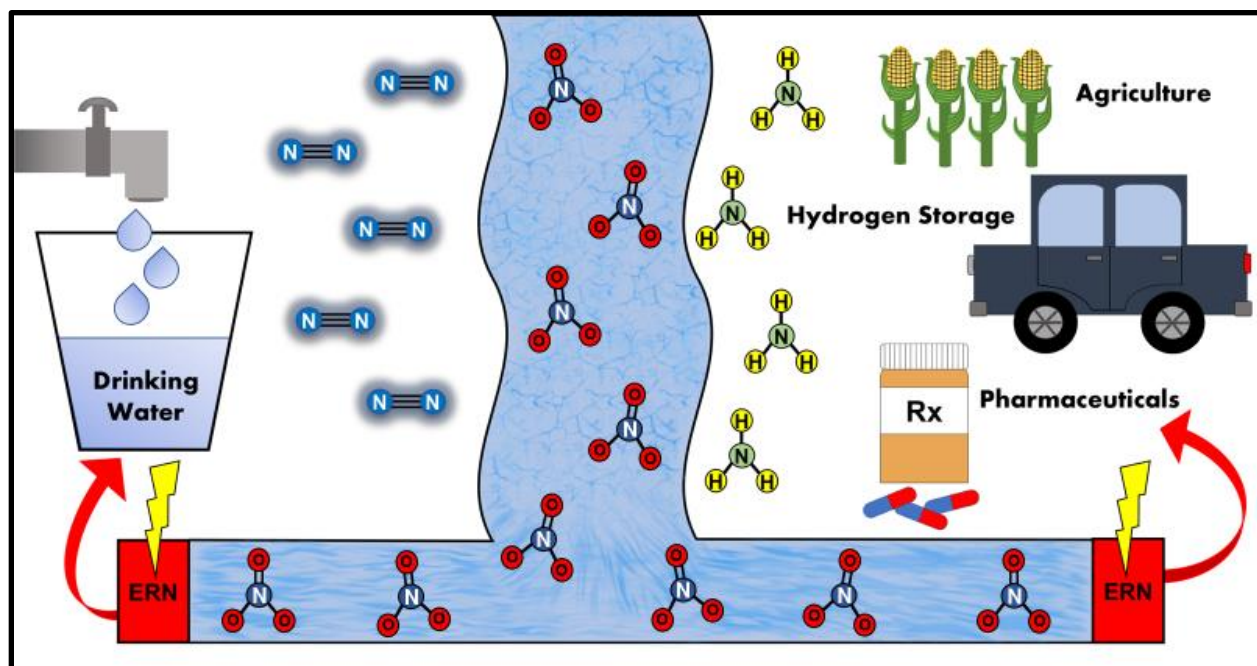
Electrocatalytic reduction of nitrate for drinking water applications via nitrogen gas formation (left), and a resource recovery for agriculture, hydrogen storage, and pharmaceuticals via ammonia formation from nitrate polluted waters (right).

CHAPTER IV

GREEN ELECTROCHEMICAL REMEDIATION OF NITRATE THROUGH BIOINSPIRED MoS$_2$/GO ELECTROCATALYST

Introduction

Nitrate pollution in ground water is an increasing societal issue, endangering both human and environmental health.[275] Such pollution has been known to lead to environmental disasters including eutrophication (algal blooms), decimation of aquatic species, and acid rains. For human health, elevated levels of nitrate ingestion have been linked to methemoglobinemia, gastric cancer, and congenital birth defects.[127,129,276] This increasing occurrence of nitrate pollution is directly related to anthropogenic activity, which ultimately leads to a major imbalance in the natural nitrogen cycle. Sources for nitrate pollution include industrial wastewater discharge, leaching from landfill and animal farms, and the most substantial - fertilizer run off from agricultural lands. It is estimated that approximately half of the nitrogen applied to crops, via fertilizer, will leach out of soil and permeate into surrounding groundwater reservoirs.[124]

The most common forms of nitrate remediation for ground water includes both physiochemical and biological treatment processes.[277] Physiochemical methods encompass ion exchange, reverse osmosis, and electrodialysis. While these techniques are viable in terms of removal capacity, they are energy intensive and generate concentrated secondary pollution streams which require further chemical treatment and additional costs.[278] Biological treatment may be considered a more environmentally friendly alternative, but this is a time-consuming process, which is heavily impacted by reaction conditions including dissolved oxygen and

temperature.[279,280] Therefore, the need for a chemical free, low energy, and rapid remediation technology for nitrate pollution in ground water is evident.

Electrocatalytic reduction of nitrates (ERN) has become an emerging compact technology for combating nitrate pollution.[276] This technology has been championed for selective product formation (N_2/NH_3), ambient operating conditions, and no requirement for additional chemical treatment.[281,282] Technologies capable of selective formation of ammonia can be advantageous for resource recovery, especially in agricultural practices.[199] Nitrate pollution stemming from fertilizer application could be electrochemically converted back into ammonia rich nutrient solutions, which could be reapplied to surrounding crops, slowing the over application of fertilizer, restoring balance to the natural nitrogen cycle.

The choice in electrocatalyst, or cathodic material, plays heavily in the selectivity and cost for such a technology.[276] Metal sulfide catalysts have been recently explored for their high selectivity towards ammonia formation and low overall pricing.[226] Looking to nature for inspiration we find that molybdenum disulfide is an essential component in nitrate reductase enzymes, commonly found in bacteria responsible for denitrification.[283,284] It has been discovered that the edge sites of MoS_2 is the active portion of the metal sulfide towards reductive processes.[285,286]Therefore, we have formulated an electrocatalytic design of nano MoS_2 (increased ratio of edge sites) grown in situ upon conductive graphene oxide (GO) particles to create a hybrid electrocatalyst for the ERN. Characterization of the electrocatalyst powder reveals 77 nm MoS_2 catalytic sites dispersed upon micrometer platelets of graphene oxide. Electrocatalytic ink was then created through dispersion of the MoS_2/GO electrocatalyst in a dilute Nafion 117 ($\approx 5\%$) solution.[287] Finally, the cathodic assembly was completed by depositing said ink upon high purity copper foam to create a highly selective ($\approx 94\%$) 3D cathode for ammonia formation from nitrate

pollution. Following further system optimizations this MoS_2/GO_Cu cathode has much potential for implementation as a resource recovery technology for nitrate pollution.

Methodology

2.1 Synthesis of GO and MoS₂/GO materials

GO was synthesized by the hummers method as described in a previous publication.[288] The hybrid MoS_2/GO material was synthesized by taking various ratios of GO and ammonia tetra thiomolybdate (2:1, 1:1, 1:2) and suspending these materials in ultra-pure MilliQ water ($\Omega=18.2$), followed by bath sonication for a period of one hour. Following sonication, the resulting solids were vacuum filtered and allowed to dry overnight at room temperature. The dried precursor was then heated to 450°C via tube furnace under a gas mixture of (90/10 Ag/H_2) for one hour; the resulting material was the MoS_2/GO electrocatalyst.

2.2 Characterization of MoS₂/GO electrocatalyst and 3D Cathode

X-ray Diffraction (XRD) analysis was conducted on a Bruker D2 Phaser Diffractometer. Diffraction patterns were collected using a Co source Kα 1.789 Å outfitted with a Fe-filter. Data collection was performed between 5–80° in 2θ, with a 0.05° step size and a counting time of two seconds per step. Data analysis was conducted with the Le Bail fitting procedure in Fullprof software referencing existing crystallographic data found in literature[289,290] Scanning electron microscopy was performed using a Nova 200 Nanolab at 5 kV and 1.6 nA.[178] spICP-MS analysis was conducted on a Perkin Elmer Nexion 1000 with a Syngtistix Nano application with a dwell time of 100μs and a scan time of 120s. Stock suspensions of MoS_2/GO were prepared according to a similar preparation method developed in our lab for carbon/metal particles[291] and were diluted down to a concentration of 0.125 ppb for sizing analysis by spICP-MS.

2.3 Preparation of Electrocatalytic Ink and Cathode Assembly

To prepare the electrocatalytic ink 12mg of the MoS_2/GO catalyst was placed in an Eppendorf tube along with 1.5ml of MilliQ H_2O and 75µL of Nafion 117 containing solution. The mixture was briefly vortexed then sonicated via bath sonication for 30 minutes. The resulting electrocatalytic ink was drop casted on 2cm x 2cm x 0.2cm battery grade Cu foam squares which were previously cleaned with acetone, 0.1M HCl, and Milli Q H_2O. The Cu foam decorated with the MoS_2/GO ink was the allowed to dry overnight in an oven at a temperature of 100°C.

2.4 Electrochemical Characterization

Cyclic Voltammetry was conducted on a CH Instruments Electrochemical Workstation Model 660E in a typical three electrode configuration. The Cu foam and MoS_2/GO_Cu foam cathodes were utilized as the working electrodes, a pure Pt coil served as a counter, and a Ag/AgCl electrode served as the reference. The volume of the pristine Cu foam, and electrocatalyst decorated Cu foam, was 2cm x 2cm x 0.2cm and all measurements were normalized according to the electrode geometrical area. A 0.1M Na_2SO_4 electrolyte was utilized for CV testing at a scan rate of 50mV s^{-1}. Additionally, $NaNO_3$ was added in various concentrations (10, 25, 50 mmol) in order to observe the corresponding current density response at potentials indicative of reduction reactions.

2.5 Electrochemical reduction of Nitrate

ERN experiments were conducted galvanostatically on an Extech DC Power Supply (Model – 382200) at 0.2A. Said experiments were performed in undivided cylindrical glass reactors containing 125ml of 100ppm NO_3 solutions with 12.5mmol of Na_2SO_4 (pH=6.3) at room temperature. The 2-electrode system comprised of parallel electrodes with a 1cm gap with dimensions of 2cm x 2cm for the working electrodes (Cu foam & MoS2/GO_Cu foam) and a

5.08cm x 7.62cm Pt coated Ti electrode as the counter. Experiments were conducted at 600rpm of magnetic stirring to ensure transport of species towards/from the electrode surface.

2.6 Analytical Instruments and Procedures

All pH measurements were taken on a Thermo Scientific Orion Star A211 meter. NO_3 and NO_2 concentrations were measured on a ThermoFischer Scientific Dionex Integrion High Pressure Ion Chromatography System (model AS29) outfitted with a Dionex IonPac AS29-fast-4µM column, and a Dionex AERS 500 carbonate suppressor. The mobile phase for the analysis was a 4.5mM Na_2CO_3 / 2.0mM $NaHCO_3$ eluent. NO_3 and NO_2 concentration analysis as conducted at a flow rate of 1 ml/min at a column temperature of 30°C. Ammonia concentrations were measured via UV-VIS spectroscopy method utilizing HACH TNT 832 and 835 kits for ammonia quantification.

Results and Discussion

3.1 Characterization of the MoS2/GO powder, Cu Foam, and MoS₂/GO_Cu Foam Cathodes

XRD analysis was performed on both the MoS_2/GO hybrid and MoS_2 prepared by an identical synthesis method, minus the presence of the GO. As can be seen in Figure 4.1 (a) the MoS_2/GO hybrid greatly minimized the (002) plane of MoS_2 centers, indicating a reduction of vertical stacking in the sulfide structure.[292] The hybrid material maintained both the (006) and (008) planes of MoS_2 which matches pervious reports of a hexagonal structure in the metal sulfide centers.[293,294] Looking at the reflections of the (001) this corresponds to the vertical stacking of graphene sheets in GO indicating multiple layers. Interestingly enough the observation of rGO (002) peak indicates that the introduction of MoS_2 centers seems to have decreased the interlayer

114

spacing of graphene units compared to pure GO, which has been known to increase the materials overall conductivity.[295–297]
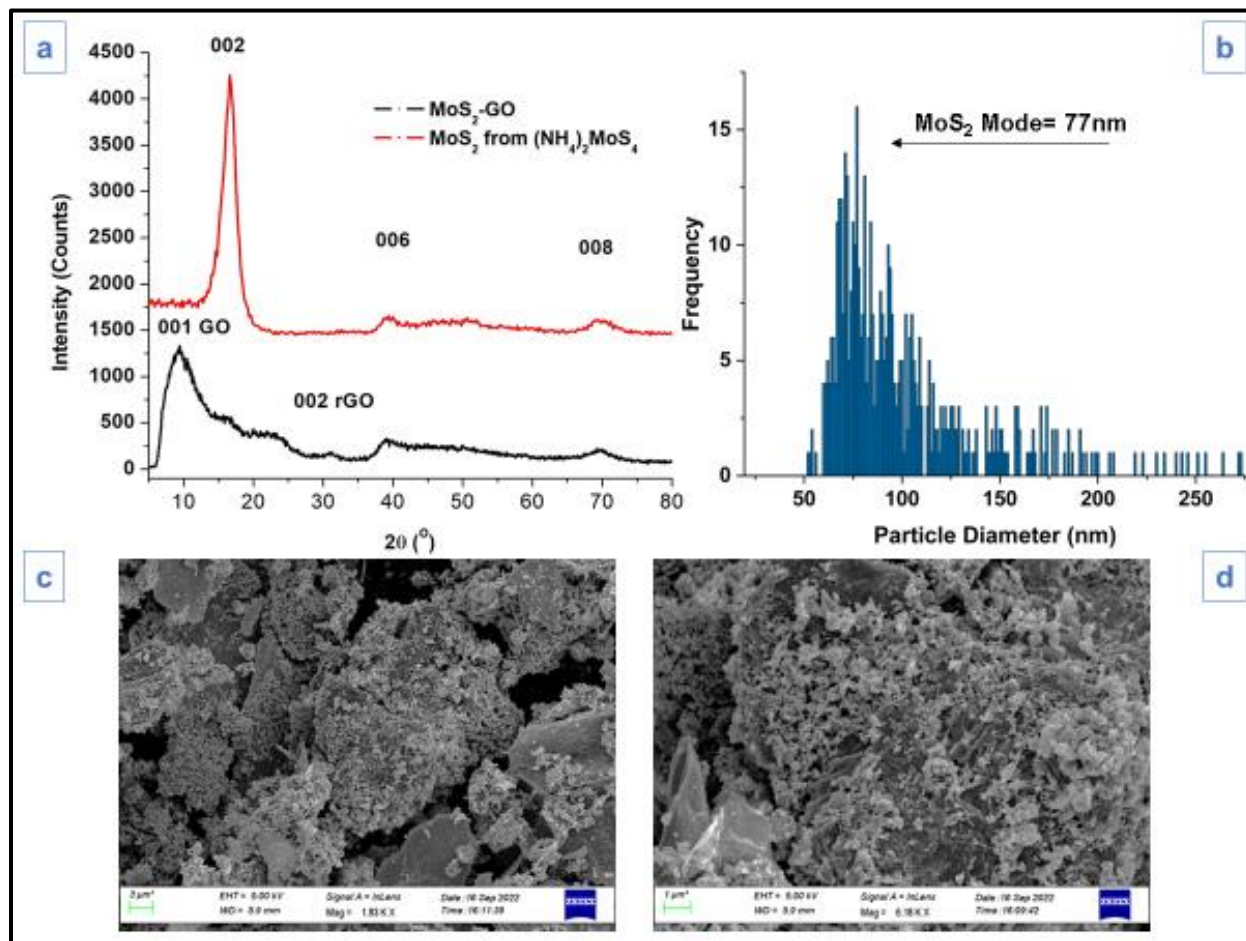
Figure 4.1: Characterization of MoS2/GO particles by XRD analysis (a) spICP-MS (b) SEM at a 1.83 K X magfication (c) and SEM at 6.18 K X magfinicatoin (d).

The size histogram generated from the spICP-MS analysis of the MoS_2/GO particles revealead a mode, or most frequent size, for the MoS_2 centers equal to 77 nm with an overall average size of 101nm. This sizing analysis focused on chacterizing the MoS_2 portion, not the entire hybrid particle; therefor parameters from this analysis include a mass fraction of 61.16%, a particle density of 5.06 g/cm^3, and a analyte mass of 97.905, the most abundant molybdenum isotope.[298,299] Inspection of SEM images of the MoS_2/GO particles, shown in Figure 4.1 (c & d),

reveal dark GO platelets in the μM range decorated with smaller (nm) lighter MoS_2 centers convering a large majority of the outside surface of the GO particles. In the current powder state we believe many of the particles were self agregated. In order to have a better understanding on the distribution of these particles, further SEM analysis was conducted on the Cu foam support before and after the addition of the electrocatalytic ink as seen in Figure 4.2.
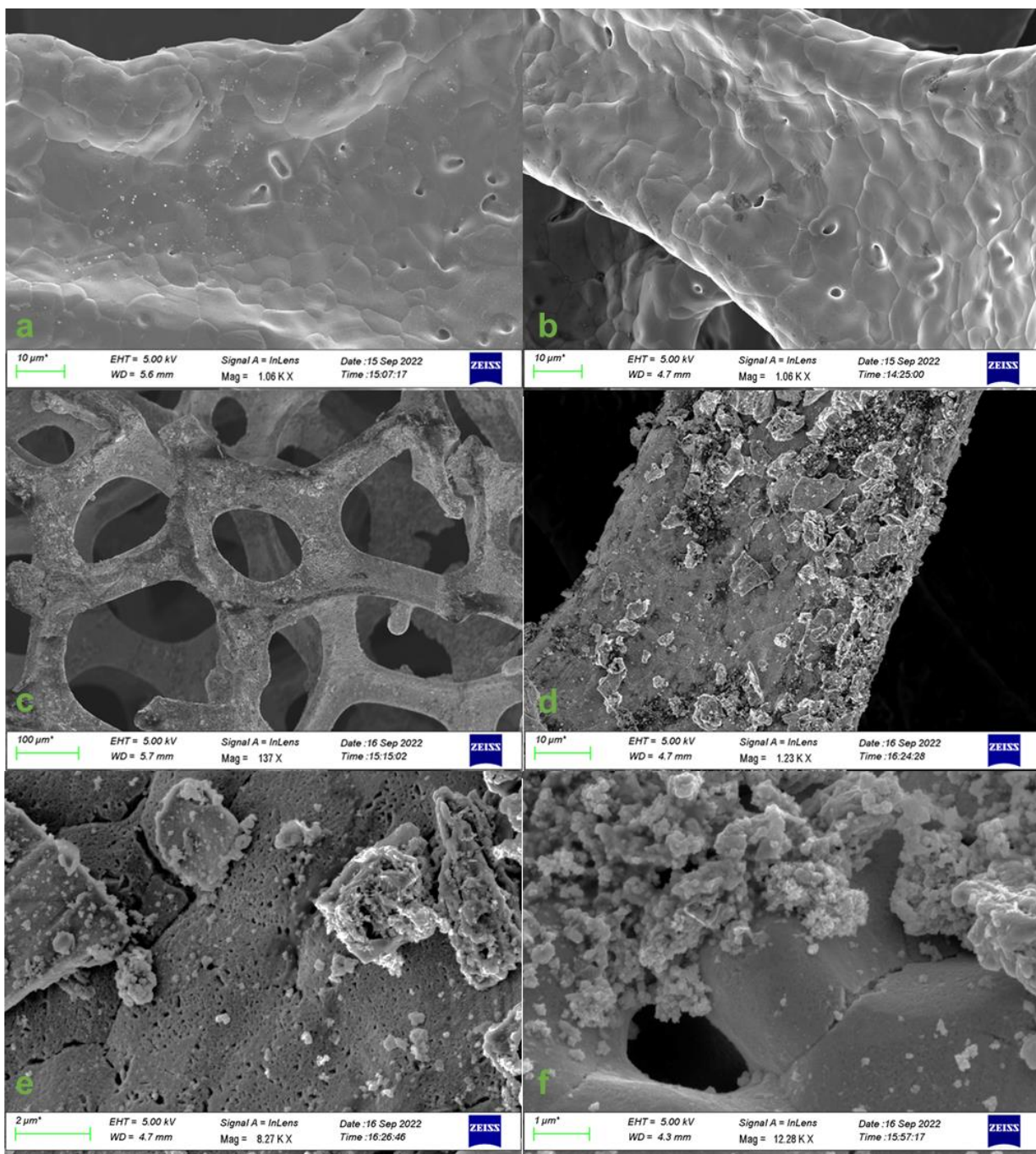
Figure 4.2: Pristine surface of Cu foam (a&b) MoS$_2$/GO decorated surface of Cu foam (c,d,e,f).

In Figure 4.2 (a&b) we observe that the pristine Cu foam is comprised of smooth Cu channels creating a porous 3D cathode. After the anchroing of the MoS$_2$/GO particles, as seen in Figure 4.2 (c&d), it is evedient that surface roughing has occurred on a large degree of the channels and

networks comprising this porous material. In portions e & d of this same figure we get a better represenation of inividiual particles bound to the Cu channels. At this perspective we can see that the MoS_2/GO particles appear to have dimensions in the (2-4µm) range, with a non-homogenous distribution of nano MoS_2 centers covering micrometer sized GO platelets. Based on the sizing data from the spICP-MS analysis we believe that we have a large amount of small MoS_2 nanoclusters adding up to a mass equivalent of a single 77 nm cluster per platelet of GO.

3.2 Electrochemical Characterization of Cu Foam and MoS₂/GO_Cu Foam

In order to characterize the electrochemical response of both pristine and MoS_2/GO decorated Cu foam, cyclic voltammetry was conducted in the prescence of 0.1M Na_2SO_4 between a potential of 0.25V and -1.5V vs an Ag/AgCl reference elecrode, at a scan rate of 50 mV s^{-1}. This reponse can be found in Figure 4.3 below denoted as the black lines shown in both portion a & b of this figure. Similar shape CV have been observed in related studies.[178] In order to compare the response of the cathodes in the plain electrolyte, to reaction solutions containing the NO_3 analyte in the same electrolyte, various concentrations were spiked into the CV solutions (10, 25, 50 mmol of $NaNO_3$) in order to identify reduction peaks associated to the nitrate reduction mechansim. These CV results can be found in Figure 4.3 as well denoted by red (10mmol), blue (25mmol), and green (50mmol) spectras. In both cathode varities we can identify three reduction peaks growing with increasing nitrate concentrations denoted at R1, R2, and R3. At futher inspection we verfied a direct linear response for increasing current density with increasing spiked concentrations of nitrate.
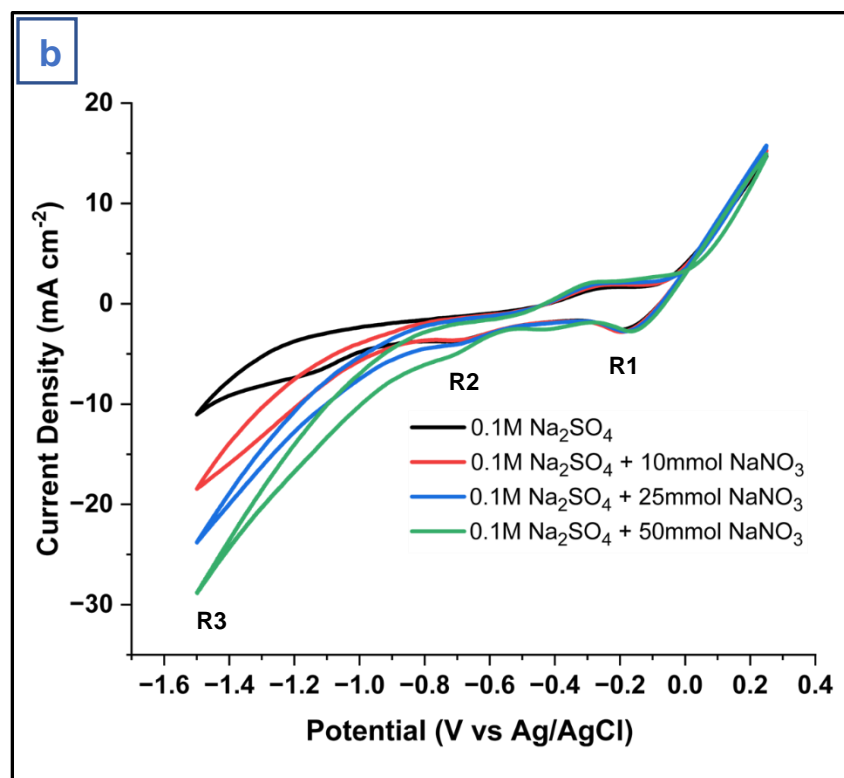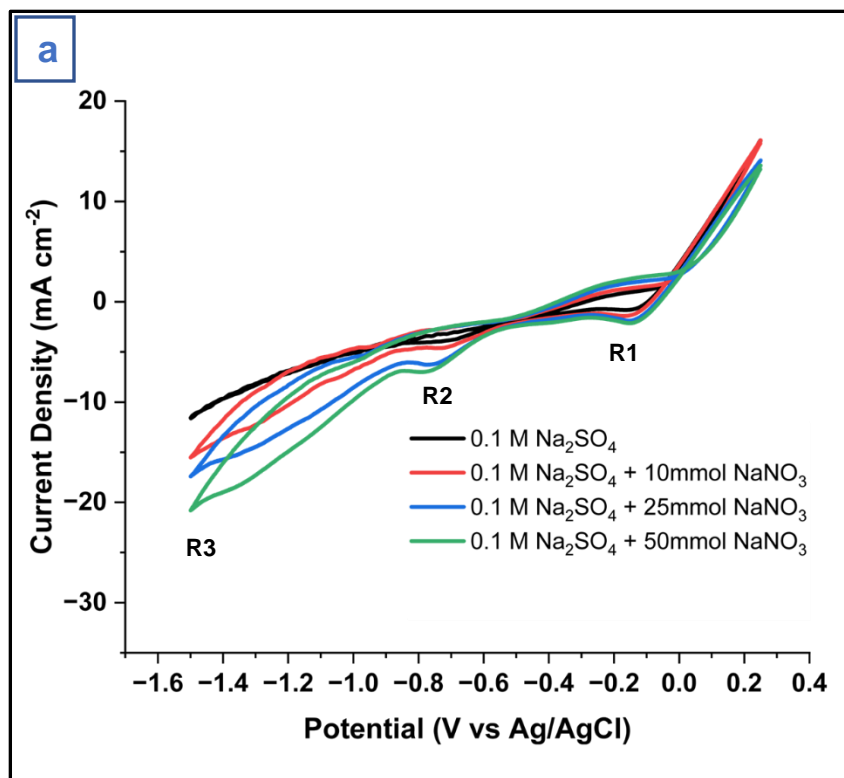
Figure 4.3: Cyclic Voltametery in 0.1M Na_2SO_4 with additions of 10, 25, 50mmol $NaNO_3$ for Cu Foam (a) and MoS_2/GO_Cu Foam (b).

Table 4.1: Potential and linearity of current peaks generated from CV at spikes of 10, 25, 50mmol of NaNO$_3$ added to 0.1M Na$_2$SO$_4$.

Cathode	RP	Potential(V)	R^2
Cu foam	R1	-0.12	0.958
	R2	-0.83	0.937
	R3	-1.5	0.999
MoS$_2$/GO_Cu foam	R1	-0.12	0.996
	R2	-0.682	0.998
	R3	-1.5	0.975

Table 4.1 one above illustrates the corresponding R$_2$ values for these linear correlations with greater linearality observed for the MoS$_2$/GO variety. It was also observed that the second reduction peak (R2) had shifted to slighlty more positive values possible indicating a possibly more effiencey reduction pathway. In either case we observe greater current density's for the MoS$_2$/GO variety, especially at potenials less negative than -0.855V vs Ag/AgCl. At a potential of -1.5V vs Ag/AgCl we see approaxiamtely 1.5X the current density for the MoS$_2$/GO variety compared to that of the pristine cathode. We would also like to mention that at a potential of -0.42 V vs Ag/AgCl we found a linear trend for current density and nitrate concentration that was apparent in both varities, but is not easily observed in Figure 4.3's current perspective.

Further testing for the ERN effeciency of the afformentioned cathodes will be conducted in galvanostatic mode, for this is the more portable, economic, and scalable approach for the ERN.[157,276] With that said the collected CV analysis could be extremely helpful in determining applied potential / product selectivity trends in various reaction conditions. By comparing the CV or linear sweep voltammetry of nitrate spiked vs nitrite spiked solutions this could help resolve which of the reduction peaks is associated with the rate limiting step of the reduction mechanism, the initial reduction of nitrate to nitrite.[277,300]

3.3 Loading of Electrocatalytic Ink and Corresponding Performance for ERN

In order to optimize the MoS_2/GO catalytic efficiency for the ERN, various loadings (100, 300, 500, 700µL) of electrocatalytic ink were drop casted on 2cm x 2cm x 0.2cm Cu foam cathodes. The performance of these cathodes were tested in 125ml of 100 ppm NO_3 solutions for a period of two hours of galvanostatic electrolysis at an applied potential of 0.2A. Their percent nitrate removal can be seen in Figure 4.4 below, with pure Cu foam denoted as 0 µL loading.
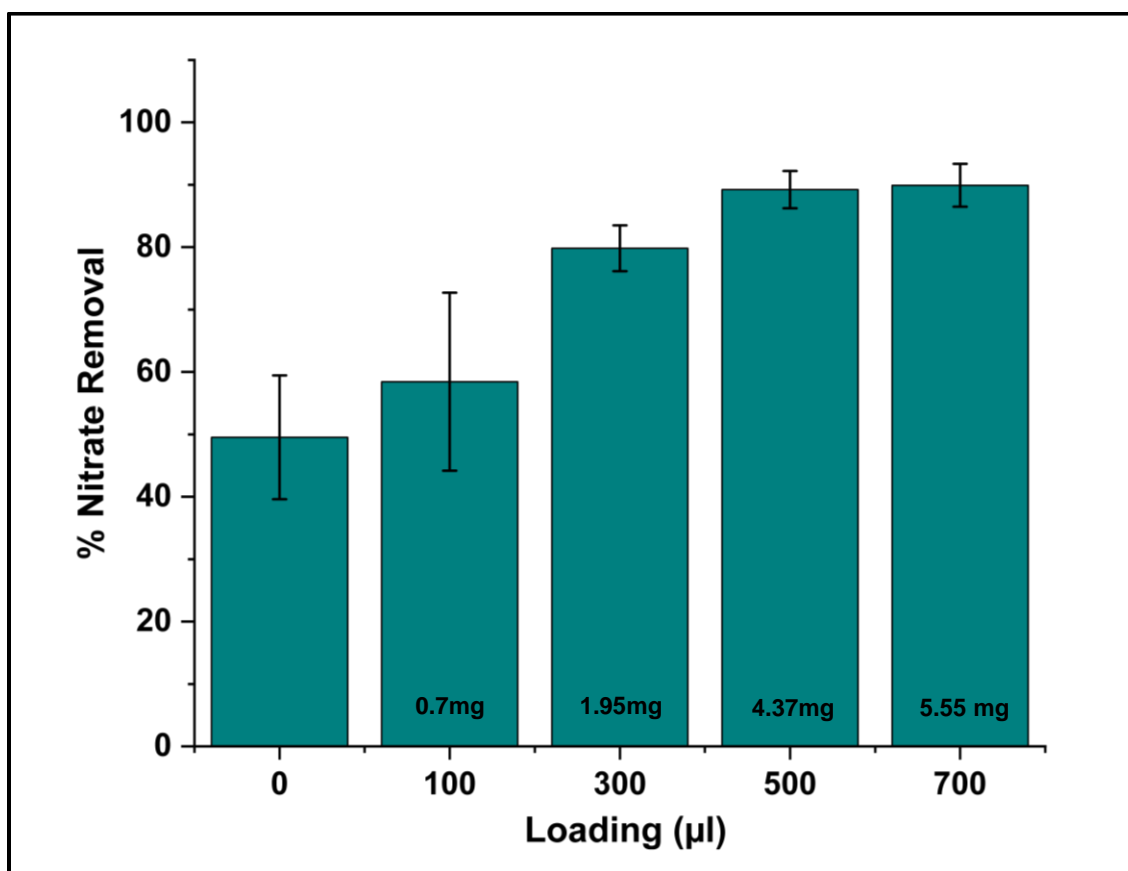
Figure 4.4: Percent Nitrate Removal for various µL loadings of MoS_2/GO electrocatalytic ink.

As can be seen by the performance of the pristine Cu foam cathode, the staring material displayed substantial activity for nitrate reduction, with nearly 50% of nitrate removed in two hours of electrolysis. For this reason, Cu has been regarded as a special monometallic cathode for the reduction of not only nitrate, but other oxyanions species as well.[301–303] From this point the

efficiency for nitrate reduction was steadily increased, with increasing loadings of the electrocatalytic ink up to 500µL with 89.2% of nitrate removed. Conversely with the 700 µL loading a negligible increase (0.7%) was observed, therefore 500 µL loading was considered optimal for all following studies. As can be seen above, the µL loadings in Figure 4.4, the corresponding mass of electrocatalyst added is denoted in mass of milligrams. Considering the average mass of the 2cm x 2cm x 0.2cm Cu Foam was ≈ 260mg, the minor addition of 4.37 mg of the MoS_2/GO electrocatalyst nearly doubled the ERN activity exemplifying the utility of this bioinspired nanocatalyst.

Figure 4.5 below shows the remaining nitrate concentration in mg/L in solution during two hours of electrolysis, utilizing the MoS_2/GO cathode, at an applied current of 0.2A. As can be seen here, nearly half the nitrate concentration is removed within the first fifteen minutes of treatment and approximately 85% was removed by 120 minutes of treatment.
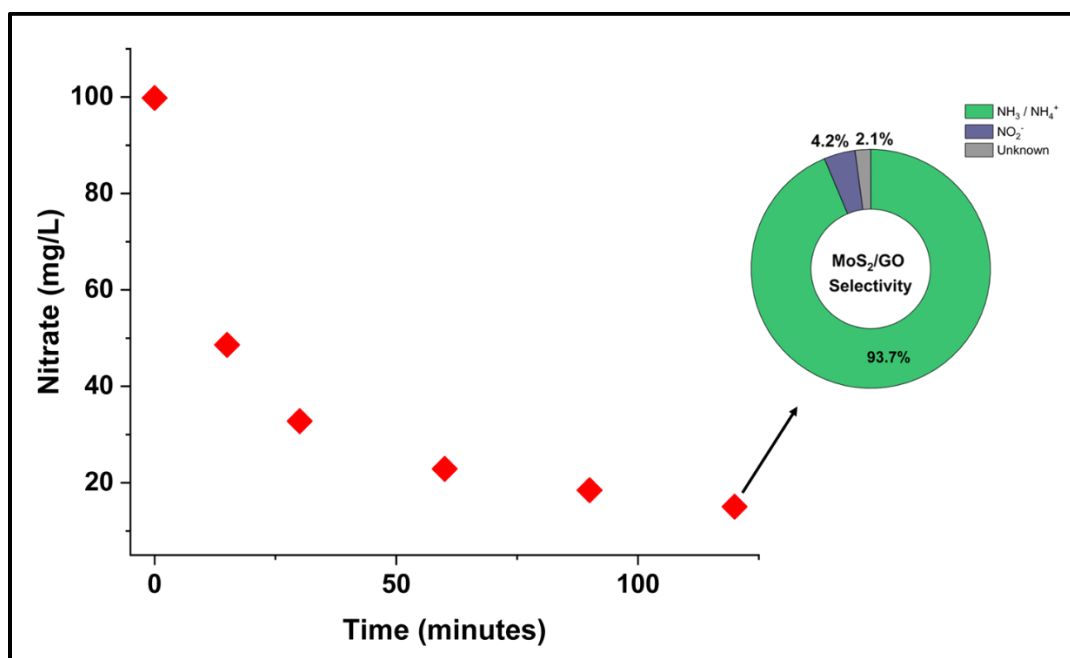
Figure 4.5: Concentration of NO_3 remaining in solution during 120 minutes of electrolysis, corresponding selectivity of last point displayed in donut chart.

At 120 minutes of electrolysis, nearly 94% of reduced species had been converted to NH_3/NH_4^+, 4.2% NO_2^-, and 2.1% of unknown species. With the aforementioned product distributions, the MoS$_2$/GO_Cu foam cathode shows much promise for applications geared towards ammonia production, as a resource recovery from nitrate pollution. As can be seen in distribution of data in Figure 4.5, a zeroth order or [NO$_3^-$] vs time plot does not create a very linear trend; therefore, we compared a 0th, 1st, and 2nd order plots[304] in order to determine the most appropriate fitting for this initial kinetics experiment, as can be seen in Figure 4.6 below. Clearly the 2nd order fitting, or $\frac{1}{[NO_3]}$ vs time, produced the most linear trend with an $R^2=0.985$. If this is in fact a 2nd order reaction, it would be advantageous to establish a reactant order, to better understand the significant parameters affecting the ERN when utilizing the MoS$_2$/GO_Cu Foam cathodes.
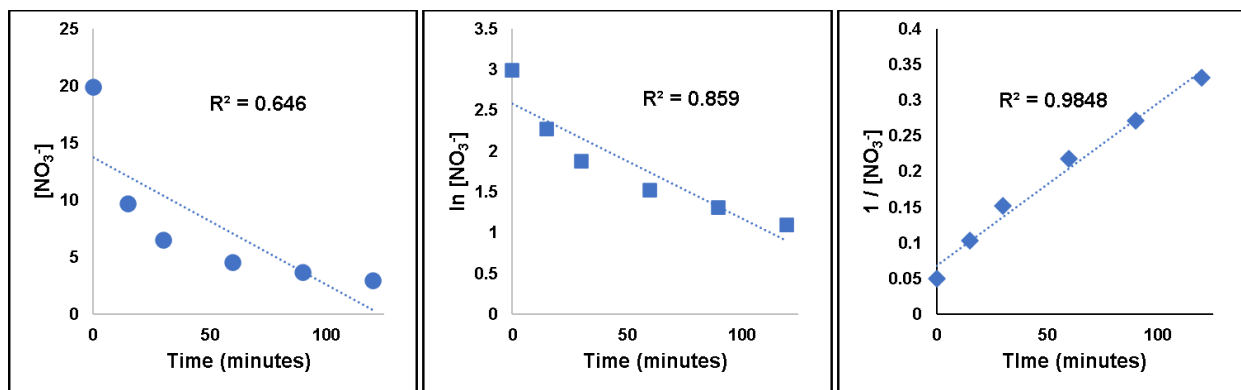
Figure 4.6: 0th, 1st, and 2nd order plots for the remaining nitrate in solution during the ERN utilizing MoS$_2$/GO_Cu foam as working electrode.

4.0 Application Focus and Future Works

Considering the substantial selectivity of the MoS_2/GO_Cu foam towards ammonia formation, we intend to gear this remediation technology towards resource recovery applications, rather than a drinking water focus (N_2 formation). This would be advantageous for industrial and agricultural processes. Considering that overapplication of fertilizers is the leading cause in nitrate pollution in ground water, we believe this should be the focus of our remediation technology. Being able to covert nitrate pollution back into ammonia could act as nutrient solutions to be reapplied to crop areas in order to reduce the overapplication of fertilizers. In this fashion we could create a circular loop in nitrogen cycle management that could reduce overall nitrate pollution. In order to gear our technology towards this we intend to optimize electrocatalytic performance by varying such parameters as initial nitrate concentration, pH of reaction solution, and applied current to study their overall contribution to the reaction rate. In such fashion we could establish a reaction order for reactants (e-, H^+, $[NO_3^-]$) to understand how these variable affect the conversion of nitrate to NH_3/NH_4^+ over specific period of ERN.

CHAPTER V

CONCLUDING PERSPECTIVES

As the applications and uses of engineered nanomaterials continues to grow so will the accumulation of these materials in different environmental sectors. spICP-MS will continue to act as an invaluable nanoanalytical tool for monitoring the stability and accumulation of nanomaterials in various aqueous media. With rising accumulation of nanomaterials in groundwater sources, this increases our possible risk for exposure, which could result in various outcomes depending on the identity, size, and concentrations of said species. Therefore, developing sensitive and reliable means to detect these particles becomes extremely important for the utilization of nanotechnology in drinking water purification.

As displayed within the second chapter of this work, we developed a novel detection/quantification method for CB particles in water, through utilization of nano lanthanum impurities as analytical tracers. This approach culminated to a reliable and sensitive means for detecting/quantifying CB particle in solution of known metal contents. Compared to conventional techniques for the detection of these particles in water, this spICP-MS based approach is superior in terms of sensitivity (LOD: 64 µg/L) and specificity (mode: 18.4nm). In addition to CB detection, such a technique could serve for monitoring other nano and micron sized graphitic particles, containing metal impurities, to ensure their proper utilization in nanotechnology driven water treatment.

Aside from the development and utilization of proper nanoanalytical tools, further large-scale surveying of nanoparticles must be completed to better understand nanomaterials accumulation in different drinking water sources. An additional study, directly related to

occurrence of nanomaterials in drinking water sources, at a large geographic scale, may be found at the following citation.[305] In this study samples were taken from 35 different drinking water sources, in five different EPA regions, across the United States over a period of six to nine months. Findings revealed there was much temporal variability within the same sampling locations, with no apparent correlation to geographical trends. Ultimately these findings suggest that flow conditions, precipitations, and point-source release strongly impact NP concentrations found in many different drinking water sources across the US.

As nitrate pollution continues to persist in ground water sources, the need for a reliable, efficient, and low-cost remediation technology for these species is imperative. The electrocatalytic reduction of nitrate could serve as a prime candidate for this technology. This approach has been known to be selective for both N_2 and NH_3 formation, which could be favorable for different applications. Considering that the overapplication of fertilizers, in agricultural regions, is the leading contributor to nitrate pollution it could be advantageous to apply the ERN in ground water sources surrounding crop areas. In this fashion nitrate pollution could be converted in ammonia rich nutrient solutions that could be reapplied to surrounding crops, in order to reduce the amount of fertilizers needed throughout the growing seasons. Herein we developed a bioinspired electrocatalyst for the ERN through the growth of nano MoS_2 centers (mode: 77nm) upon conductive micron sized graphene oxide particles. This hybrid material was then formulated in an electrocatalytic ink that was applied to porous battery grade Cu foam (2cm x 2cm x 0.2cm) to create a highly selective 3D cathode for the formation of ammonia ($\approx$94%) from nitrate pollution. After further optimizations including applied current, pH of reaction solution, and initial nitrate concentrations this technology will have much potential as a remediation technology for nitrate polluted waters in agricultural regions.

REFERENCES

(1) Petersen, E. J.; Flores-Cervantes, D. X.; Bucheli, T. D.; Elliott, L. C. C.; Fagan, J. A.; Gogos, A.; Hanna, S.; Kägi, R.; Mansfield, E.; Bustos, A. R. M.; Plata, D. L.; Reipa, V.; Westerhoff, P.; Winchester, M. R. Quantification of Carbon Nanotubes in Environmental Matrices: Current Capabilities, Case Studies, and Future Prospects. *Environ. Sci. Technol.* **2016**, *50* (9), 4587–4605. https://doi.org/10.1021/acs.est.5b05647.

(2) Vance, M. E.; Kuiken, T.; Vejerano, E. P.; McGinnis, S. P.; Jr, M. F. H.; Rejeski, D.; Hull, M. S. Nanotechnology in the Real World: Redeveloping the Nanomaterial Consumer Products Inventory. *Beilstein J. Nanotechnol.* **2015**, *6* (1), 1769–1780. https://doi.org/10.3762/bjnano.6.181.

(3) Montaño, M. D.; Majestic, B. J.; Jämting, Å. K.; Westerhoff, P.; Ranville, J. F. Methods for the Detection and Characterization of Silica Colloids by Microsecond SpICP-MS. *Anal. Chem.* **2016**, *88* (9), 4733–4741. https://doi.org/10.1021/acs.analchem.5b04924.

(4) Laborda, F.; Bolea, E.; Jiménez-Lamana, J. Single Particle Inductively Coupled Plasma Mass Spectrometry: A Powerful Tool for Nanoanalysis. *Anal. Chem.* **2014**, *86* (5), 2270–2278. https://doi.org/10.1021/ac402980q.

(5) Kawaguchi, H.; Fukasawa, N.; Mizuike, A. Investigation of Airborne Particles by Inductively Coupled Plasma Emission Spectrometry Calibrated with Monodisperse Aerosols. *Spectrochim. Acta Part B At. Spectrosc.* **1986**, *41* (12), 1277–1286. https://doi.org/10.1016/0584-8547(86)80006-4.

(6) Stephan, C.; Neubauer, K.; Shelton, C. Single Particle Inductively Coupled Plasma Mass Spectrometry: Understanding How and Why. *PerkinElmer White Pap.* **2014**.

(7) Peters, R.; Herrera-Rivera, Z.; Undas, A.; Lee, M. van der; Marvin, H.; Bouwmeester, H.; Weigel, S. Single Particle ICP-MS Combined with a Data Evaluation Tool as a Routine Technique for the Analysis of Nanoparticles in Complex Matrices. *J. Anal. At. Spectrom.* **2015**, *30* (6), 1274–1285. https://doi.org/10.1039/C4JA00357H.

(8) Pace, H. E.; Rogers, N. J.; Jarolimek, C.; Coleman, V. A.; Higgins, C. P.; Ranville, J. F. Determining Transport Efficiency for the Purpose of Counting and Sizing Nanoparticles via Single Particle Inductively Coupled Plasma Mass Spectrometry. *Anal. Chem.* **2011**, *83* (24), 9361–9369. https://doi.org/10.1021/ac201952t.

(9) Hochella, M. F.; Mogk, D. W.; Ranville, J.; Allen, I. C.; Luther, G. W.; Marr, L. C.; McGrail, B. P.; Murayama, M.; Qafoku, N. P.; Rosso, K. M.; Sahai, N.; Schroeder, P. A.; Vikesland, P.; Westerhoff, P.; Yang, Y. Natural, Incidental, and Engineered Nanomaterials and Their Impacts on the Earth System. *Science* **2019**, *363* (6434), eaau8299. https://doi.org/10.1126/science.aau8299.

(10) Johnson, M. E.; Hanna, S.; Bustos, A. R. M.; Nelson, B. C.; Petersen, E. J.; Yu, L. L. Using Single Particle ICP-MS as a Tool for Understanding Metallic Nanoparticle Transformation during Nanotoxicity Assays | NIST; 2014.

(11) Bao, D.; Oh, Z. G.; Chen, Z. Characterization of Silver Nanoparticles Internalized by Arabidopsis Plants Using Single Particle ICP-MS Analysis. *Front. Plant Sci.* **2016**, *7*. https://doi.org/10.3389/fpls.2016.00032.

(12) Witzler, M.; Küllmer, F.; Günther, K. Validating a Single-Particle ICP-MS Method to Measure Nanoparticles in Human Whole Blood for Nanotoxicology. *Anal. Lett.* **2018**, *51* (4), 587–599. https://doi.org/10.1080/00032719.2017.1327538.

(13) Malysheva, A.; Lombi, E.; Voelcker, N. H. Bridging the Divide between Human and Environmental Nanotoxicology. *Nat. Nanotechnol.* **2015**, *10* (10), 835–844. https://doi.org/10.1038/nnano.2015.224.

(14) Lee, S.; Bi, X.; Reed, R. B.; Ranville, J. F.; Herckes, P.; Westerhoff, P. Nanoparticle Size Detection Limits by Single Particle ICP-MS for 40 Elements. *Environ. Sci. Technol.* **2014**, *48* (17), 10291–10300. https://doi.org/10.1021/es502422v.

(15) Afrand, M.; Toghraie, D.; Ruhani, B. Effects of Temperature and Nanoparticles Concentration on Rheological Behavior of Fe3O4–Ag/EG Hybrid Nanofluid: An Experimental Study. *Exp. Therm. Fluid Sci.* **2016**, *77*, 38–44. https://doi.org/10.1016/j.expthermflusci.2016.04.007.

(16) Tiede, K.; Hassellöv, M.; Breitbarth, E.; Chaudhry, Q.; Boxall, A. B. A. Considerations for Environmental Fate and Ecotoxicity Testing to Support Environmental Risk Assessments for Engineered Nanoparticles. *J. Chromatogr. A* **2009**, *1216* (3), 503–509. https://doi.org/10.1016/j.chroma.2008.09.008.

(17) Bolea-Fernandez, E.; Leite, D.; Rua-Ibarz, A.; Liu, T.; Woods, G.; Aramendia, M.; Resano, M.; Vanhaecke, F. On the Effect of Using Collision/Reaction Cell (CRC) Technology in Single-Particle ICP-Mass Spectrometry (SP-ICP-MS). *Anal. Chim. Acta* **2019**, *1077*, 95–106. https://doi.org/10.1016/j.aca.2019.05.077.

(18) Praetorius, A.; Gundlach-Graham, A.; Goldberg, E.; Fabienke, W.; Navratilova, J.; Gondikas, A.; Kaegi, R.; Günther, D.; Hofmann, T.; Kammer, F. von der. Single-Particle Multi-Element Fingerprinting (SpMEF) Using Inductively-Coupled Plasma Time-of-Flight Mass Spectrometry (ICP-TOFMS) to Identify Engineered Nanoparticles against the Elevated Natural Background in Soils. *Environ. Sci. Nano* **2017**, *4* (2), 307–314. https://doi.org/10.1039/C6EN00455E.

(19) Maynard, A. D.; Aitken, R. J.; Butz, T.; Colvin, V.; Donaldson, K.; Oberdörster, G.; Philbert, M. A.; Ryan, J.; Seaton, A.; Stone, V.; Tinkle, S. S.; Tran, L.; Walker, N. J.; Warheit, D. B. Safe Handling of Nanotechnology. *Nature* **2006**, *444* (7117), 267–269. https://doi.org/10.1038/444267a.

(20) Maynard, A. D.; Aitken, R. J. "Safe Handling of Nanotechnology" Ten Years On. *Nat. Nanotechnol.* **2016**, *11*, 998–1000. https://doi.org/10.1038/nnano.2016.270.

(21) Warheit, D. B. Hazard and Risk Assessment Strategies for Nanoparticle Exposures: How Far Have We Come in the Past 10 Years? *F1000Research* **2018**, *7*. https://doi.org/10.12688/f1000research.12691.1.

(22) Adeleye, A. S.; Oranu, E. A.; Tao, M.; Keller, A. A. Release and Detection of Nanosized Copper from a Commercial Antifouling Paint. *Water Res.* **2016**, *102*, 374–382. https://doi.org/10.1016/j.watres.2016.06.056.

(23) Auffan, M.; Rose, J.; Bottero, J.-Y.; Lowry, G. V.; Jolivet, J.-P.; Wiesner, M. R. Towards a Definition of Inorganic Nanoparticles from an Environmental, Health and Safety Perspective. *Nat. Nanotechnol.* **2009**, *4* (10), 634–641. https://doi.org/10.1038/nnano.2009.242.

(24) Mitrano, D. M.; Lombi, E.; Dasilva, Y. A. R.; Nowack, B. Unraveling the Complexity in the Aging of Nanoenhanced Textiles: A Comprehensive Sequential Study on the Effects of Sunlight and Washing on Silver Nanoparticles. *Environ. Sci. Technol.* **2016**, *50* (11), 5790–5799. https://doi.org/10.1021/acs.est.6b01478.

(25) Wagener, S.; Dommershausen, N.; Jungnickel, H.; Laux, P.; Mitrano, D.; Nowack, B.; Schneider, G.; Luch, A. Textile Functionalization and Its Effects on the Release of Silver

Nanoparticles into Artificial Sweat. *Environ. Sci. Technol.* **2016**, *50* (11), 5927–5934. https://doi.org/10.1021/acs.est.5b06137.

(26) Strenge, I.; Engelhard, C. Capabilities of Fast Data Acquisition with Microsecond Time Resolution in Inductively Coupled Plasma Mass Spectrometry and Identification of Signal Artifacts from Millisecond Dwell Times during Detection of Single Gold Nanoparticles. *J. Anal. At. Spectrom.* **2016**, *31* (1), 135–144. https://doi.org/10.1039/C5JA00177C.

(27) Mackevica, A.; Olsson, M. E.; Hansen, S. F. Quantitative Characterization of TiO2 Nanoparticle Release from Textiles by Conventional and Single Particle ICP-MS. *J. Nanoparticle Res.* **2017**, *20* (1), 6. https://doi.org/10.1007/s11051-017-4113-2.

(28) Bocca, B.; Caimi, S.; Senofonte, O.; Alimonti, A.; Petrucci, F. ICP-MS Based Methods to Characterize Nanoparticles of TiO2 and ZnO in Sunscreens with Focus on Regulatory and Safety Issues. *Sci. Total Environ.* **2018**, *630*, 922–930. https://doi.org/10.1016/j.scitotenv.2018.02.166.

(29) Dan, Y.; Shi, H.; Stephan, C.; Liang, X. Rapid Analysis of Titanium Dioxide Nanoparticles in Sunscreens Using Single Particle Inductively Coupled Plasma–Mass Spectrometry. *Microchem. J.* **2015**, *122*, 119–126. https://doi.org/10.1016/j.microc.2015.04.018.

(30) de la Calle, I.; Menta, M.; Klein, M.; Séby, F. Screening of TiO2 and Au Nanoparticles in Cosmetics and Determination of Elemental Impurities by Multiple Techniques (DLS, SP-ICP-MS, ICP-MS and ICP-OES). *Talanta* **2017**, *171*, 291–306. https://doi.org/10.1016/j.talanta.2017.05.002.

(31) Aznar, R.; Barahona, F.; Geiss, O.; Ponti, J.; José Luis, T.; Barrero-Moreno, J. Quantification and Size Characterisation of Silver Nanoparticles in Environmental Aqueous Samples and Consumer Products by Single Particle-ICPMS. *Talanta* **2017**, *175*, 200–208. https://doi.org/10.1016/j.talanta.2017.07.048.

(32) Goetz, N. von; Fabricius, L.; Glaus, R.; Weitbrecht, V.; Günther, D.; Hungerbühler, K. Migration of Silver from Commercial Plastic Food Containers and Implications for Consumer Exposure Assessment. *Food Addit. Contam. Part A* **2013**, *30* (3), 612–620. https://doi.org/10.1080/19440049.2012.762693.

(33) Mackevica, A.; Olsson, M. E.; Hansen, S. F. Silver Nanoparticle Release from Commercially Available Plastic Food Containers into Food Simulants. *J. Nanoparticle Res.* **2016**, *18* (1), 5. https://doi.org/10.1007/s11051-015-3313-x.

(34) Ramos, K.; Gómez-Gómez, M. M.; Cámara, C.; Ramos, L. Silver Speciation and Characterization of Nanoparticles Released from Plastic Food Containers by Single Particle ICPMS. *Talanta* **2016**, *151*, 83–90. https://doi.org/10.1016/j.talanta.2015.12.071.

(35) Folens, K.; Van Acker, T.; Bolea-Fernandez, E.; Cornelis, G.; Vanhaecke, F.; Du Laing, G.; Rauch, S. Identification of Platinum Nanoparticles in Road Dust Leachate by Single Particle Inductively Coupled Plasma-Mass Spectrometry. *Sci. Total Environ.* **2018**, *615*, 849–856. https://doi.org/10.1016/j.scitotenv.2017.09.285.

(36) Montaño, M. D.; Olesik, J. W.; Barber, A. G.; Challis, K.; Ranville, J. F. Single Particle ICP-MS: Advances toward Routine Analysis of Nanomaterials. *Anal. Bioanal. Chem.* **2016**, *408* (19), 5053–5074. https://doi.org/10.1007/s00216-016-9676-8.

(37) Merrifield, R. C.; Stephan, C.; Lead, J. Determining the Concentration Dependent Transformations of Ag Nanoparticles in Complex Media: Using SP-ICP-MS and Au@Ag Core-Shell Nanoparticles as Tracers. *Environ. Sci. Technol.* **2017**, *51* (6), 3206–3213. https://doi.org/10.1021/acs.est.6b05178.

(38) Yang, Y.; Long, C. L.; Li, H. P.; Wang, Q.; Yang, Z. G. Analysis of Silver and Gold Nanoparticles in Environmental Water Using Single Particle-Inductively Coupled Plasma-Mass Spectrometry. *Sci. Total Environ.* **2016**, *563–564* (392), 996–1007. https://doi.org/10.1016/j.scitotenv.2015.12.150.

(39) Azodi, M.; Sultan, Y.; Ghoshal, S. Dissolution Behavior of Silver Nanoparticles and Formation of Secondary Silver Nanoparticles in Municipal Wastewater by Single-Particle ICP-MS. *Environ. Sci. Technol.* **2016**, *50* (24), 13318–13327. https://doi.org/10.1021/acs.est.6b03957.

(40) Azimzada, A.; Tufenkji, N.; Wilkinson, K. J. Transformations of Silver Nanoparticles in Wastewater Effluents: Links to Ag Bioavailability. *Environ. Sci. Nano* **2017**, *4* (6), 1339–1349. https://doi.org/10.1039/c7en00093f.

(41) Newman, K.; Metcalfe, C.; Martin, J.; Hintelmann, H.; Shaw, P.; Donard, A. Improved Single Particle ICP-MS Characterization of Silver Nanoparticles at Environmentally Relevant Concentrations. *J. Anal. At. Spectrom.* **2016**, *31* (10), 2069–2077. https://doi.org/10.1039/c6ja00221h.

(42) Tuoriniemi, J.; Jürgens, M. D.; Hassellöv, M.; Cornelis, G. Size Dependence of Silver Nanoparticle Removal in a Wastewater Treatment Plant Mesocosm Measured by FAST Single Particle ICP-MS. *Environ. Sci. Nano* **2017**, *4* (5), 1189–1197. https://doi.org/10.1039/c6en00650g.

(43) Donovan, A. R.; Adams, C. D.; Ma, Y.; Stephan, C.; Eichholz, T.; Shi, H. Detection of Zinc Oxide and Cerium Dioxide Nanoparticles during Drinking Water Treatment by Rapid Single Particle ICP-MS Methods. *Anal. Bioanal. Chem.* **2016**, *408* (19), 5137–5145. https://doi.org/10.1007/s00216-016-9432-0.

(44) Proulx, K.; Hadioui, M.; Wilkinson, K. J. Separation, Detection and Characterization of Nanomaterials in Municipal Wastewaters Using Hydrodynamic Chromatography Coupled to ICPMS and Single Particle ICPMS. *Anal. Bioanal. Chem.* **2016**, *408* (19), 5147–5155. https://doi.org/10.1007/s00216-016-9451-x.

(45) Yang, Y.; Luo, L.; Li, H. P.; Wang, Q.; Yang, Z. G.; Qu, Z. P.; Ding, R. Analysis of Metallic Nanoparticles and Their Ionic Counterparts in Complex Matrix by Reversed-Phase Liquid Chromatography Coupled to ICP-MS. *Talanta* **2018**, *182* (January), 156–163. https://doi.org/10.1016/j.talanta.2018.01.077.

(46) Lu, S.; Tan, Z.; Liu, P.; Zhao, H.; Liu, D.; Yu, S.; Cheng, P.; Win, M. S.; Hu, J.; Tian, L.; Wu, M.; Yonemochi, S.; Wang, Q. Single Particle Aerosol Mass Spectrometry of Coal Combustion Particles Associated with High Lung Cancer Rates in Xuanwei and Fuyuan, China. *Chemosphere* **2017**, *186*, 278–286. https://doi.org/10.1016/j.chemosphere.2017.07.161.

(47) Ma, L.; Li, M.; Zhang, H.; Li, L.; Huang, Z.; Gao, W.; Chen, D.; Fu, Z.; Nian, H.; Zou, L.; Gao, J.; Chai, F.; Zhou, Z. Comparative Analysis of Chemical Composition and Sources of Aerosol Particles in Urban Beijing during Clear, Hazy, and Dusty Days Using Single Particle Aerosol Mass Spectrometry. *J. Clean. Prod.* **2016**, *112*, 1319–1329. https://doi.org/10.1016/j.jclepro.2015.04.054.

(48) Arndt, J.; Deboudt, K.; Anderson, A.; Blondel, A.; Eliet, S.; Flament, P.; Fourmentin, M.; Healy, R. M.; Savary, V.; Setyan, A.; Wenger, J. C. Scanning Electron Microscopy-Energy Dispersive X-Ray Spectrometry (SEM-EDX) and Aerosol Time-of-Flight Mass Spectrometry (ATOFMS) Single Particle Analysis of Metallurgy Plant Emissions. *Environ. Pollut.* **2016**, *210*, 9–17. https://doi.org/10.1016/j.envpol.2015.11.019.

(49) Hadri, H. E.; M. Louie, S.; A. Hackley, V. Assessing the Interactions of Metal Nanoparticles in Soil and Sediment Matrices – a Quantitative Analytical Multi-Technique Approach. *Environ. Sci. Nano* **2018**, *5* (1), 203–214. https://doi.org/10.1039/C7EN00868F.

(50) Mahdi, K. N. M.; Peters, R. J. B.; Klumpp, E.; Bohme, S.; Ploeg, M. van der; Ritsema, C.; Geissen, V. Silver Nanoparticles in Soil: Aqueous Extraction Combined with Single-Particle ICP-MS for Detection and Characterization. *Environ. Nanotechnol. Monit. Manag.* **2017**, *7*, 24–33. https://doi.org/10.1016/j.enmm.2016.12.002.

(51) Hadri, H. E.; A. Hackley, V. Investigation of Cloud Point Extraction for the Analysis of Metallic Nanoparticles in a Soil Matrix. *Environ. Sci. Nano* **2017**, *4* (1), 105–116. https://doi.org/10.1039/C6EN00322B.

(52) Hsiao, I.-L.; Bierkandt, F. S.; Reichardt, P.; Luch, A.; Huang, Y.-J.; Jakubowski, N.; Tentschert, J.; Haase, A. Quantification and Visualization of Cellular Uptake of TiO2 and Ag Nanoparticles: Comparison of Different ICP-MS Techniques. *J. Nanobiotechnology* **2016**, *14* (1), 50. https://doi.org/10.1186/s12951-016-0203-z.

(53) Campagnolo, L.; Massimiani, M.; Vecchione, L.; Piccirilli, D.; Toschi, N.; Magrini, A.; Bonanno, E.; Scimeca, M.; Castagnozzi, L.; Buonanno, G.; Stabile, L.; Cubadda, F.; Aureli, F.; Fokkens, P. H. B.; Kreyling, W. G.; Cassee, F. R.; Pietroiusti, A. Silver Nanoparticles Inhaled during Pregnancy Reach and Affect the Placenta and the Foetus. *Nanotoxicology* **2017**, *11* (5), 687–698. https://doi.org/10.1080/17435390.2017.1343875.

(54) Vidmar, J.; Buerki-Thurnherr, T.; Loeschner, K. Comparison of the Suitability of Alkaline or Enzymatic Sample Pre-Treatment for Characterization of Silver Nanoparticles in Human Tissue by Single Particle ICP-MS. *J. Anal. At. Spectrom.* **2018**, *33* (5), 752–761. https://doi.org/10.1039/c7ja00402h.

(55) Gallocchio, F.; Biancotto, G.; Cibin, V.; Losasso, C.; Belluco, S.; Peters, R.; Van Bemmel, G.; Cascio, C.; Weigel, S.; Tromp, P.; Gobbo, F.; Catania, S.; Ricci, A. Transfer Study of Silver Nanoparticles in Poultry Production. *J. Agric. Food Chem.* **2017**, *65* (18), 3767–3774. https://doi.org/10.1021/acs.jafc.7b00670.

(56) Heringa, M. B.; Peters, R. J. B.; Bleys, R. L. A. W.; van der Lee, M. K.; Tromp, P. C.; van Kesteren, P. C. E.; van Eijkeren, J. C. H.; Undas, A. K.; Oomen, A. G.; Bouwmeester, H. Detection of Titanium Particles in Human Liver and Spleen and Possible Health Implications. *Part. Fibre Toxicol.* **2018**, *15* (1), 15. https://doi.org/10.1186/s12989-018-0251-7.

(57) Vidmar, J.; Loeschner, K.; Correia, M.; Larsen, E. H.; Manser, P.; Wichser, A.; Boodhia, K.; Al-Ahmady, Z. S.; Ruiz, J.; Astruc, D.; Buerki-Thurnherr, T. Translocation of Silver Nanoparticles in the: Ex Vivo Human Placenta Perfusion Model Characterized by Single Particle ICP-MS. *Nanoscale* **2018**, *10* (25), 11980–11991. https://doi.org/10.1039/c8nr02096e.

(58) Makama, S.; Piella, J.; Undas, A.; Dimmers, W. J.; Peters, R.; Puntes, V. F.; van den Brink, N. W. Properties of Silver Nanoparticles Influencing Their Uptake in and Toxicity to the Earthworm Lumbricus Rubellus Following Exposure in Soil. *Environ. Pollut.* **2016**, *218*, 870–878. https://doi.org/10.1016/j.envpol.2016.08.016.

(59) Kollander, B.; Widemo, F.; Ågren, E.; Larsen, E. H.; Loeschner, K. Detection of Lead Nanoparticles in Game Meat by Single Particle ICP-MS Following Use of Lead-Containing Bullets. *Anal. Bioanal. Chem.* **2017**, *409* (7), 1877–1885. https://doi.org/10.1007/s00216-016-0132-6.

(60) Keller, A. A.; Huang, Y.; Nelson, J. Detection of Nanoparticles in Edible Plant Tissues Exposed to Nano-Copper Using Single-Particle ICP-MS. **2018**.

(61) Kińska, K.; Jiménez-Lamana, J.; Kowalska, J.; Krasnodębska-Ostręga, B.; Szpunar, J. Study of the Uptake and Bioaccumulation of Palladium Nanoparticles by Sinapis Alba Using Single Particle ICP-MS. *Sci. Total Environ.* **2018**, *615*, 1078–1085. https://doi.org/10.1016/j.scitotenv.2017.09.203.

(62) Jiménez-Lamana, J.; Wojcieszek, J.; Jakubiak, M.; Asztemborska, M.; Szpunar, J. Single Particle ICP-MS Characterization of Platinum Nanoparticles Uptake and Bioaccumulation by: Lepidium Sativum and Sinapis Alba Plants. *J. Anal. At. Spectrom.* **2016**, *31* (11), 2321–2329. https://doi.org/10.1039/c6ja00201c.

(63) Dan, Y.; Ma, X.; Zhang, W.; Liu, K.; Stephan, C.; Shi, H. Single Particle ICP-MS Method Development for the Determination of Plant Uptake and Accumulation of CeO 2 Nanoparticles. *Anal. Bioanal. Chem.* **2016**, *408* (19), 5157–5167. https://doi.org/10.1007/s00216-016-9565-1.

(64) Li, C. C.; Dang, F.; Li, M.; Zhu, M.; Zhong, H.; Hintelmann, H.; Zhou, D. M. Effects of Exposure Pathways on the Accumulation and Phytotoxicity of Silver Nanoparticles in Soybean and Rice. *Nanotoxicology* **2017**, *11* (5), 699–709. https://doi.org/10.1080/17435390.2017.1344740.

(65) la Calle, I. De; Pérez-Rodríguez, P.; Soto-Gómez, D.; López-Periago, J. E. Detection and Characterization of Cu-Bearing Particles in Throughfall Samples from Vine Leaves by DLS, AF4-MALLS (-ICP-MS) and SP-ICP-MS. *Microchem. J.* **2017**, *133*, 293–301. https://doi.org/10.1016/j.microc.2017.03.034.

(66) Bettini, S.; Boutet-Robinet, E.; Cartier, C.; Coméra, C.; Gaultier, E.; Dupuy, J.; Naud, N.; Taché, S.; Grysan, P.; Reguer, S.; Thieriet, N.; Réfrégiers, M.; Thiaudière, D.; Cravedi, J.-P.; Carrière, M.; Audinot, J.-N.; Pierre, F. H.; Guzylack-Piriou, L.; Houdeau, E. Food-Grade TiO 2 Impairs Intestinal and Systemic Immune Homeostasis, Initiates Preneoplastic Lesions and Promotes Aberrant Crypt Development in the Rat Colon. *Sci. Rep.* **2017**, *7* (1), 1–13. https://doi.org/10.1038/srep40373.

(67) Schoon, J.; Geißler, S.; Traeger, J.; Luch, A.; Tentschert, J.; Perino, G.; Schulze, F.; Duda, G. N.; Perka, C.; Rakow, A. Multi-Elemental Nanoparticle Exposure after Tantalum Component Failure in Hip Arthroplasty: In-Depth Analysis of a Single Case. *Nanomedicine Nanotechnol. Biol. Med.* **2017**, *13* (8), 2415–2423. https://doi.org/10.1016/j.nano.2017.08.004.

(68) Ramos, K.; Ramos, L.; Gómez-Gómez, M. M. Simultaneous Characterisation of Silver Nanoparticles and Determination of Dissolved Silver in Chicken Meat Subjected to in Vitro Human Gastrointestinal Digestion Using Single Particle Inductively Coupled Plasma Mass Spectrometry. *Food Chem.* **2017**, *221*, 822–828. https://doi.org/10.1016/j.foodchem.2016.11.091.

(69) Hussain, S. M.; Hess, K. L.; Gearhart, J. M.; Geiss, K. T.; Schlager, J. J. In Vitro Toxicity of Nanoparticles in BRL 3A Rat Liver Cells. *Toxicol. In Vitro* **2005**, *19* (7), 975–983. https://doi.org/10.1016/j.tiv.2005.06.034.

(70) Malysheva, A.; Ivask, A.; Hager, C.; Brunetti, G.; Marzouk, E. R.; Lombi, E.; Voelcker, N. H. Sorption of Silver Nanoparticles to Laboratory Plastic during (Eco)Toxicological Testing. *Nanotoxicology* **2016**, *10* (4), 385–390. https://doi.org/10.3109/17435390.2015.1084059.

(71)   Roman, M.; Rigo, C.; Castillo-Michel, H.; Munivrana, I.; Vindigni, V.; Mičetić, I.; Benetti, F.; Manodori, L.; Cairns, W. R. L. Hydrodynamic Chromatography Coupled to Single-Particle ICP-MS for the Simultaneous Characterization of AgNPs and Determination of Dissolved Ag in Plasma and Blood of Burn Patients. *Anal. Bioanal. Chem.* **2016**, *408* (19), 5109–5124. https://doi.org/10.1007/s00216-015-9014-6.

(72)   Proulx, K.; Hadioui, M.; Wilkinson, K. J. Separation , Detection and Characterization of Nanomaterials in Municipal Wastewaters Using Hydrodynamic Chromatography Coupled to ICPMS and Single Particle ICPMS. *Anal. Bioanal. Chem.* **2016**, 5147–5155. https://doi.org/10.1007/s00216-016-9451-x.

(73)   Mozhayeva, D.; Strenge, I.; Engelhard, C. Implementation of Online Preconcentration and Microsecond Time Resolution to Capillary Electrophoresis Single Particle Inductively Coupled Plasma Mass Spectrometry (CE-SP-ICP-MS) and Its Application in Silver Nanoparticle Analysis. *Anal. Chem.* **2017**, *89* (13), 7152–7159. https://doi.org/10.1021/acs.analchem.7b01185.

(74)   Tan, J.; Liu, J.; Li, M.; El Hadri, H.; Hackley, V. A.; Zachariah, M. R. Electrospray-Differential Mobility Hyphenated with Single Particle Inductively Coupled Plasma Mass Spectrometry for Characterization of Nanoparticles and Their Aggregates. *Anal. Chem.* **2016**, *88* (17), 8548–8555. https://doi.org/10.1021/acs.analchem.6b01544.

(75)   Lee, W.-C.; Lee, B.-T.; Lee, S.; Hwang, Y. S.; Jo, E.; Eom, I.-C.; Lee, S.-W.; Kim, S.-O. Optimisation, Evaluation and Application of Asymmetrical Flow Field-Flow Fractionation with Single Particle Inductively Coupled Plasma Mass Spectrometry (SP-ICP-MS) to Characterise Silver Nanoparticles in Environmental Media. *Microchem. J.* **2016**, *129*, 219–230. https://doi.org/10.1016/j.microc.2016.06.030.

(76)   Naasz, S.; Weigel, S.; Borovinskaya, O.; Serva, A.; Cascio, C.; Undas, A. K.; Simeone, F. C.; Marvin, H. J. P.; Peters, R. J. B. Multi-Element Analysis of Single Nanoparticles by ICP-MS Using Quadrupole and Time-of-Flight Technologies. *J. Anal. At. Spectrom.* **2018**, *33* (5), 835–845. https://doi.org/10.1039/C7JA00399D.

(77)   Lamsal, R. P.; Jerkiewicz, G.; Beauchemin, D. Flow Injection Single Particle Inductively Coupled Plasma Mass Spectrometry: An Original Simple Approach for the Characterization of Metal-Based Nanoparticles. *Anal. Chem.* **2016**, *88* (21), 10552–10558. https://doi.org/10.1021/acs.analchem.6b02656.

(78)   Benešová, I.; Dlabková, K.; Zelenák, F.; Vaculovič, T.; Kanický, V.; Preisler, J. Direct Analysis of Gold Nanoparticles from Dried Droplets Using Substrate-Assisted Laser Desorption Single Particle-ICPMS. *Anal. Chem.* **2016**, *88* (5), 2576–2582. https://doi.org/10.1021/acs.analchem.5b02421.

(79)   Miyashita, S.; Mitsuhashi, H.; Fujii, S.; Takatsu, A.; Inagaki, K.; Fujimoto, T. High Transport Efficiency of Nanoparticles through a Total-Consumption Sample Introduction System and Its Beneficial Application for Particle Size Evaluation in Single-Particle ICP-MS. *Anal. Bioanal. Chem.* **2017**, *409* (6), 1531–1545. https://doi.org/10.1007/s00216-016-0089-5.

(80)   Aghaei, M.; Bogaerts, A. Particle Transport through an Inductively Coupled Plasma Torch: Elemental Droplet Evaporation. *J. Anal. At. Spectrom.* **2016**, *31* (3), 631–641.

(81)   Kálomista, I.; Kéri, A.; Galbács, G. On the Applicability and Performance of the Single Particle ICP-MS Nano-Dispersion Characterization Method in Cases Complicated by Spectral Interferences. *J. Anal. At. Spectrom.* **2016**, *31* (5), 1112–1122. https://doi.org/10.1039/C5JA00501A.

(82)   Kálomista, I.; Kéri, A.; Ungor, D.; Csapó, E.; Dékány, I.; Prohaska, T.; Galbács, G. Dimensional Characterization of Gold Nanorods by Combining Millisecond and Microsecond Temporal Resolution Single Particle ICP-MS Measurements. *J. Anal. At. Spectrom.* **2017**, *32* (12), 2455–2462. https://doi.org/10.1039/C7JA00306D.

(83)   A. Sötebier, C.; J. Kutscher, D.; Rottmann, L.; Jakubowski, N.; Panne, U.; Bettmer, J. Combination of Single Particle ICP-QMS and Isotope Dilution Analysis for the Determination of Size, Particle Number and Number Size Distribution of Silver Nanoparticles. *J. Anal. At. Spectrom.* **2016**, *31* (10), 2045–2052. https://doi.org/10.1039/C6JA00137H.

(84)   Hetzer, B.; Burcza, A.; Gräf, V.; Walz, E.; Greiner, R. Online-Coupling of AF4 and Single Particle-ICP-MS as an Analytical Approach for the Selective Detection of Nanosilver Release from Model Food Packaging Films into Food Simulants. *Food Control* **2017**, *80*, 113–124. https://doi.org/10.1016/j.foodcont.2017.04.040.

(85)   Candás-Zapico, S.; Kutscher, D. J.; Montes-Bayón, M.; Bettmer, J. Single Particle Analysis of TiO2 in Candy Products Using Triple Quadrupole ICP-MS. *Talanta* **2018**, *180*, 309–315. https://doi.org/10.1016/j.talanta.2017.12.041.

(86)   Khodabakhshi, S.; Fulvio, P. F.; Andreoli, E. Carbon Black Reborn: Structure and Chemistry for Renewable Energy Harnessing. *Carbon* **2020**, *162*, 604–649. https://doi.org/10.1016/j.carbon.2020.02.058.

(87)   CHEAP TUBES. *Graphene Nanoplatelets*. CHEAP TUBES. https://www.cheaptubes.com/product/graphene-nanoplatelets/.

(88)   CHEAP TUBES. *Multi Walled Carbon Nanotubes*. CHEAP TUBES. https://www.cheaptubes.com/product-category/multi-walled-carbon-nanotubes/.

(89)   CHEAP TUBES. *Carbon Fullerenes C60*. CHEAP TUBES. https://www.cheaptubes.com/product/carbon-fullerenes-c60/.

(90)   Said, I. A.; Fuentes, N.; He, Z.; Xin, R.; Zuo, K.; Li, Q. Low-Cost Desalination of Seawater and Hypersaline Brine Using Nanophotonics Enhanced Solar Energy Membrane Distillation. *Environ. Sci. Water Res. Technol.* **2020**, *6* (8), 2180–2196. https://doi.org/10.1039/D0EW00254B.

(91)   Huang, X.; Yue, H.; Attia, A.; Yang, Y. Preparation and Properties of Manganese Oxide/Carbon Composites by Reduction of Potassium Permanganate with Acetylene Black. *J. Electrochem. Soc.* **2006**, 9.

(92)   Zhang, L.; Zhang, M.; Wang, Y.; Zhang, Z.; Kan, G.; Wang, C.; Zhong, Z.; Su, F. Graphitized Porous Carbon Microspheres Assembled with Carbon Black Nanoparticles as Improved Anode Materials in Li-Ion Batteries. *J. Mater. Chem. A* **2014**, *2* (26), 10161. https://doi.org/10.1039/c4ta00356j.

(93)   Long, C. M.; Nascarella, M. A.; Valberg, P. A. Carbon Black vs. Black Carbon and Other Airborne Materials Containing Elemental Carbon: Physical and Chemical Distinctions. *Environ. Pollut.* **2013**, *181*, 271–286. https://doi.org/10.1016/j.envpol.2013.06.009.

(94)   *Carbon Black User's Guide*; International Carbon Black Association (ICBA), 2018. http://www.carbon-black.org/index.php/carbon-black-uses (accessed 2021-03-25).

(95)   Marsh, H.; Rodriguez-Reinoso, F. CHAPTER 2 - Activated Carbon (Origins). *Act. Carbon* **2006**, 13–86.

(96)   Kiciński, W.; Dyjak, S. Transition Metal Impurities in Carbon-Based Materials: Pitfalls, Artifacts and Deleterious Effects. *Carbon* **2020**, *168*, 748–845. https://doi.org/10.1016/j.carbon.2020.06.004.

(97) Lepri, F. G.; Borges, D. L. G.; Araujo, R. G. O.; Welz, B.; Wendler, F.; Krieg, M.; Becker-Ross, H. Determination of Heavy Metals in Activated Charcoals and Carbon Black for Lyocell Fiber Production Using Direct Solid Sampling High-Resolution Continuum Source Graphite Furnace Atomic Absorption and Inductively Coupled Plasma Optical Emission Spectrometry. *Talanta* **2010**, *81* (3), 980–987. https://doi.org/10.1016/j.talanta.2010.01.050.

(98) Doudrick, K.; Herckes, P.; Westerhoff, P. Detection of Carbon Nanotubes in Environmental Matrices Using Programmed Thermal Analysis. *Environ. Sci. Technol.* **2012**, *46* (22), 12246–12253. https://doi.org/10.1021/es300804f.

(99) Pace, H. E.; Rogers, N. J.; Jarolimek, C.; Coleman, V. A.; Higgins, C. P.; Ranville, J. F. Determining Transport Efficiency for the Purpose of Counting and Sizing Nanoparticles via Single Particle Inductively Coupled Plasma Mass Spectrometry. *Anal. Chem.* **2011**, *83* (24), 9361–9369. https://doi.org/10.1021/ac201952t.

(100) Hadioui, M.; Knapp, G.; Azimzada, A.; Jreije, I.; Frechette-Viens, L.; Wilkinson, K. J. Lowering the Size Detection Limits of Ag and TiO_2 Nanoparticles by Single Particle ICP-MS. *Anal. Chem.* **2019**, *91* (20), 13275–13284. https://doi.org/10.1021/acs.analchem.9b04007.

(101) Kidd, J.; Bi, Y.; Hanigan, D.; Herckes, P.; Westerhoff, P. Yttrium Residues in MWCNT Enable Assessment of MWCNT Removal during Wastewater Treatment. *Nanomaterials* **2019**, *9* (5), 670. https://doi.org/10.3390/nano9050670.

(102) Lim, J.-H.; Bairi, V. G.; Fong, A. Quantification of Impurities in Carbon Nanotubes: Development of ICP-MS Sample Preparation Methods. *Mater. Chem. Phys.* **2017**, *198*, 324–330. https://doi.org/10.1016/j.matchemphys.2017.06.014.

(103) Reed, R. B.; Goodwin, D. G.; Marsh, K. L.; Capracotta, S. S.; Higgins, C. P.; Fairbrother, D. H.; Ranville, J. F. Detection of Single Walled Carbon Nanotubes by Monitoring Embedded Metals. *Env. Sci Process. Impacts* **2013**, *15* (1), 204–213. https://doi.org/10.1039/C2EM30717K.

(104) ICP-OES & MS Detection Limit Guidance, 2007. http://www.nanoscience.co.jp/surface_analysis/pdf/icp-oes-ms-detection-limit-guidance-BR023.pdf (accessed 2021-04-07).

(105) May, T.; Weidmeyer, R. Table of Polyatomic Interferences in ICP-MS. *At. Spectrosc.* **1998**, *19* (5), 150–155.

(106) PubChem. PubChem Element Summary for AtomicNumber 57, Lanthanum. https://pubchem.ncbi.nlm.nih.gov/element/Lanthanum. (accessed 2022-02-09).

(107) Yang, C. Calcium and Magnesium in Drinking Water and the Risk of Death from Hypertension. *Am. J. Hypertens.* **1999**, *12* (9), 894–899. https://doi.org/10.1016/S0895-7061(99)00065-5.

(108) Donovan, A. R.; Adams, C. D.; Ma, Y.; Stephan, C.; Eichholz, T.; Shi, H. Single Particle ICP-MS Characterization of Titanium Dioxide, Silver, and Gold Nanoparticles during Drinking Water Treatment. *Chemosphere* **2016**, *144*, 148–153. https://doi.org/10.1016/j.chemosphere.2015.07.081.

(109) Mackevica, A.; Olsson, M. E.; Hansen, S. F. Quantitative Characterization of $TiO2$ Nanoparticle Release from Textiles by Conventional and Single Particle ICP-MS. *J. Nanoparticle Res.* **2018**, *20* (1), 6. https://doi.org/10.1007/s11051-017-4113-2.

(110) Proulx, K.; Wilkinson, K. J. Separation, Detection and Characterisation of Engineered Nanoparticles in Natural Waters Using Hydrodynamic Chromatography and Multi-

Method Detection (Light Scattering, Analytical Ultracentrifugation and Single Particle ICP-MS). *Environ. Chem.* **2014**, *11* (4), 392. https://doi.org/10.1071/EN13232.

(111) Fernández-Trujillo, S.; Jiménez-Moreno, M.; Ríos, Á.; Martín-Doimeadios, R. del C. R. A Simple Analytical Methodology for Platinum Nanoparticles Control in Complex Clinical Matrices via SP-ICP-MS. *Talanta* **2021**, *231*, 122370. https://doi.org/10.1016/j.talanta.2021.122370.

(112) Roman, M.; Rigo, C.; Castillo-Michel, H.; Munivrana, I.; Vindigni, V.; Mičetić, I.; Benetti, F.; Manodori, L.; Cairns, W. R. L. Hydrodynamic Chromatography Coupled to Single-Particle ICP-MS for the Simultaneous Characterization of AgNPs and Determination of Dissolved Ag in Plasma and Blood of Burn Patients. *Anal. Bioanal. Chem.* **2016**, *408* (19), 5109–5124. https://doi.org/10.1007/s00216-015-9014-6.

(113) Shrivastava, A.; Gupta, V. Methods for the Determination of Limit of Detection and Limit of Quantitation of the Analytical Methods. *Chron. Young Sci.* **2011**, *2* (1), 21. https://doi.org/10.4103/2229-5186.79345.

(114) Armbruster, D. A.; Pry, T. Limit of Blank, Limit of Detection and Limit of Quantitation. *Clin. Biochem. Rev.* **2008**, *29 Suppl 1*, S49-52.

(115) Currie, L. A. Nomenclature in Evaluation of Analytical Methods Including Detection and Quantification Capabilities (IUPAC Recommendations 1995). *Pure Appl. Chem.* **1995**, *67* (10), 1699–1723. https://doi.org/10.1351/pac199567101699.

(116) Hem, J. D. *Study and Interpretation of the Chemical Characterstics of Natural Waters*; U.S Geological Survey Water-Supply Paper 2254; Department of the Interior, 1985.

(117) USGS. *Ground-Water Quality*; United States Geological Survey. https://pubs.usgs.gov/wri/wri024045/htms/report2.htm (accessed 2022-07-05).

(118) USGS. *Quality Assurance and Quality Control*; appendix table 1; United States Geological Survey. https://pubs.usgs.gov/wri/wri024045/htms/apptable.htm (accessed 2022-07-05).

(119) Quattrini, S. Natural Mineral Waters: Chemical Characteristics and Health Effects. *Clin. Cases Miner. Bone Metab.* **2016**. https://doi.org/10.11138/ccmbm/2016.13.3.173.

(120) Montaño, M. D.; Badiei, H. R.; Bazargan, S.; Ranville, J. F. Improvements in the Detection and Characterization of Engineered Nanoparticles Using SpICP-MS with Microsecond Dwell Times. *Env. Sci Nano* **2014**, *1* (4), 338–346. https://doi.org/10.1039/C4EN00058G.

(121) Groffman, P. M.; Rosi, E. J.; Fulweiler, R. W. The Nitrogen Cycle. In *Fundamentals of Ecosystem Science*; Elsevier, 2021; pp 161–188. https://doi.org/10.1016/B978-0-12-812762-9.00008-3.

(122) Lehnert, N.; Musselman, B. W.; Seefeldt, L. C. Grand Challenges in the Nitrogen Cycle. *Chem. Soc. Rev.* **2021**, *50* (6), 3640–3646. https://doi.org/10.1039/D0CS00923G.

(123) Wiren, N. von; Gazzarrini, S.; Frommer, W. B. Regulation of Mineral Nitrogen Uptake in Plants. *Plant Soil 196*, 191–199.

(124) Galloway, J. N.; Cowling, E. B. Reactive Nitrogen and The World: 200 Years of Change. *AMBIO J. Hum. Environ.* **2002**, *31* (2), 64–71. https://doi.org/10.1579/0044-7447-31.2.64.

(125) Be´langer, G.; Ziadi, N.; Walsh, J. R.; Richards, J. E.; Milburn, P. H. Residual Soil Nitrate after Potato Harvest. *J. Enviromental Qual.* **2003**, *32*, 607–612.

(126) Peel, J. W.; Reddy, K. J.; Sullivan, B. P.; Bowen, J. M. Electrocatalytic Reduction of Nitrate in Water. *Water Res.* **2003**, *37*, 2512–2519.

(127) Kross, B. C. NITRATE TOXICITY AND DRINKING WATER STANDARDS – A REVIEW. 8.

(128) Curry, S. Methemoglobinemia. *Ann. Emerg. Med.* **1982**, *11* (4), 214–221.

(129) Majumdar, D.; Gupta, N. Nitrate Pollution of Groundwater and Associated Human Health Disorders. *Indian J. Environ. Health* **2000**, 12.

(130) Beard, J. C.; Swager, T. M. An Organic Chemist's Guide to *N* -Nitrosamines: Their Structure, Reactivity, and Role as Contaminants. *J. Org. Chem.* **2021**, *86* (3), 2037–2057. https://doi.org/10.1021/acs.joc.0c02774.

(131) Ward, M.; Jones, R.; Brender, J.; de Kok, T.; Weyer, P.; Nolan, B.; Villanueva, C.; van Breda, S. Drinking Water Nitrate and Human Health: An Updated Review. *Int. J. Environ. Res. Public. Health* **2018**, *15* (7), 1557. https://doi.org/10.3390/ijerph15071557.

(132) Espejo-Herrera, N.; Gràcia-Lavedan, E.; Boldo, E.; Aragonés, N.; Pérez-Gómez, B.; Pollán, M.; Molina, A. J.; Fernández, T.; Martín, V.; La Vecchia, C.; Bosetti, C.; Tavani, A.; Polesel, J.; Serraino, D.; Gómez Acebo, I.; Altzibar, J. M.; Ardanaz, E.; Burgui, R.; Pisa, F.; Fernández-Tardón, G.; Tardón, A.; Peiró, R.; Navarro, C.; Castaño-Vinyals, G.; Moreno, V.; Righi, E.; Aggazzotti, G.; Basagaña, X.; Nieuwenhuijsen, M.; Kogevinas, M.; Villanueva, C. M. Colorectal Cancer Risk and Nitrate Exposure through Drinking Water and Diet: Risk of CRC Associated with Nitrate Exposure. *Int. J. Cancer* **2016**, *139* (2), 334–346. https://doi.org/10.1002/ijc.30083.

(133) Schullehner, J.; Hansen, B.; Thygesen, M.; Pedersen, C. B.; Sigsgaard, T. Nitrate in Drinking Water and Colorectal Cancer Risk: A Nationwide Population-Based Cohort Study: Nitrate in Drinking Water and CRC. *Int. J. Cancer* **2018**, *143* (1), 73–79. https://doi.org/10.1002/ijc.31306.

(134) Tada, K.; Kawaguchi, T.; Shimazu, K. High Electrocatalytic Performance of Pd/Sn/Au Electrodes for Nitrate Reduction. *J. Electroanal. Chem.* **2004**, *572*, 93–99.

(135) Rezvani, F.; Sarrafzadeh, M.-H.; Ebrahimi, S.; Oh, H.-M. Nitrate Removal from Drinking Water with a Focus on Biological Methods: A Review. *Environ. Sci. Pollut. Res.* **2019**, *26* (2), 1124–1141. https://doi.org/10.1007/s11356-017-9185-0.

(136) Bhatnagar, A.; Sillanpää, M. A Review of Emerging Adsorbents for Nitrate Removal from Water. *Chem. Eng. J.* **2011**, *168* (2), 493–504. https://doi.org/10.1016/j.cej.2011.01.103.

(137) Tucker, P. M.; Waite, M. J.; Hayden, B. E. Electrocatalytic Reduction of Nitrate on Activated Rhodium Electrode Surfaces. *J. Appl. Electrochem.* **2004**, *34* (8), 781–796. https://doi.org/10.1023/B:JACH.0000035607.19248.b6.

(138) Teng, W.; Bai, N.; Liu, Y.; Liu, Y.; Fan, J.; Zhang, W. Selective Nitrate Reduction to Dinitrogen by Electrocatalysis on Nanoscale Iron Encapsulated in Mesoporous Carbon. *Environ. Sci. Technol.* **2018**, *52* (1), 230–236. https://doi.org/10.1021/acs.est.7b04775.

(139) Shen, Z.; Liu, D.; Peng, G.; Ma, Y.; Li, J.; Shi, J.; Peng, J.; Ding, L. Electrocatalytic Reduction of Nitrate in Water Using Cu/Pd Modified Ni Foam Cathode: High Nitrate Removal Efficiency and N2-Selectivity. *Sep. Purif. Technol.* **2020**, *241*, 116743. https://doi.org/10.1016/j.seppur.2020.116743.

(140) Su, J. F.; Kuan, W.-F.; Liu, H. L.; Huang, C. P. Mode of Electrochemical Deposition on the Structure and Morphology of Bimetallic Electrodes and Its Effect on Nitrate Reduction toward Nitrogen Selectivity. *Appl. Catal. B Enviromental* **2019**, *257*.

(141) Heck, K. N.; Garcia-Segura, S.; Westerhoff, P.; Wong, M. S. Catalytic Converters for Water Treatment. *Acc. Chem. Res.* **2019**, *52* (4), 906–915. https://doi.org/10.1021/acs.accounts.8b00642.

(142) Elgrishi, N.; Rountree, K. J.; McCarthy, B. D.; Rountree, E. S.; Eisenhart, T. T.; Dempsey, J. L. A Practical Beginner's Guide to Cyclic Voltammetry. *J. Chem. Educ.* **2018**, *95* (2), 197–206. https://doi.org/10.1021/acs.jchemed.7b00361.

(143) Boudart, M. Turnover Rates in Heterogeneous Catalysis. *Chem. Rev.* **1995**, *95* (3), 661–666. https://doi.org/10.1021/cr00035a009.

(144) Brazier, J. B.; Hellgardt, K.; Hii, K. K. (Mimi). Catalysis in Flow: O_2 Effect on the Catalytic Activity of $Ru(OH)_x$ /γ-Al_2O_3 during the Aerobic Oxidation of an Alcohol. *React. Chem. Eng.* **2017**, *2* (1), 60–67. https://doi.org/10.1039/C6RE00208K.

(145) Bagotskiĭ, V. S. *Fundamentals of Electrochemistry*, 2nd ed.; The Electrochemical Society series; Wiley-Interscience: Hoboken, N.J, 2006.

(146) Brett, C. M. A.; Brett, A. M. O. *Electrochemistry: Principles, Methods, and Applications*; Oxford science publications; Oxford University Press: Oxford ; New York, 1993.

(147) Deng, X.; Yang, Y.; Wang, L.; Fu, X.; Luo, J. Metallic Co Nanoarray Catalyzes Selective NH_3 Production from Electrochemical Nitrate Reduction at Current Densities Exceeding 2 A Cm^{-2}. *Adv. Sci.* **2021**, *8* (7), 2004523. https://doi.org/10.1002/advs.202004523.

(148) Wang, Z.; Young, S. D.; Goldsmith, B. R.; Singh, N. Increasing Electrocatalytic Nitrate Reduction Activity by Controlling Adsorption through PtRu Alloying. *J. Catal.* **2021**, *395*, 143–154. https://doi.org/10.1016/j.jcat.2020.12.031.

(149) Fajardo, A. S.; Westerhoff, P.; Sanchez-Sanchez, C. M.; Garcia-Segura, S. Earth-Abundant Elements a Sustainable Solution for Electrocatalytic Reduction of Nitrate. *Appl. Catal. B Environ.* **2021**, *281*, 119465. https://doi.org/10.1016/j.apcatb.2020.119465.

(150) Jonoush, Z. A. Electrocatalytic Nitrate Reduction Using Fe0/Fe3O4 Nanoparticles Immobilized on Nickel Foam: Selectivity and Energy Consumption Studies. *J. Clean. Prod.* **2020**, 12.

(151) Brett, C. M. A. Electrochemistry. In *Reference Module in Chemistry, Molecular Sciences and Chemical Engineering*; Elsevier, 2014; p B9780124095472108000. https://doi.org/10.1016/B978-0-12-409547-2.10742-5.

(152) Zhang, L.; Wei, Z.; Thanneeru, S.; Meng, M.; Kruzyk, M.; Ung, G.; Liu, B.; He, J. A Polymer Solution To Prevent Nanoclustering and Improve the Selectivity of Metal Nanoparticles for Electrocatalytic CO_2 Reduction. *Angew. Chem. Int. Ed.* **2019**, *58* (44), 15834–15840. https://doi.org/10.1002/anie.201909069.

(153) Li, Y.; Xiao, S.; Li, X.; Chang, C.; Xie, M.; Xu, J.; Yang, Z. A Robust Metal-Free Electrocatalyst for Nitrate Reduction Reaction to Synthesize Ammonia. *Mater. Today Phys.* **2021**, *19*, 100431. https://doi.org/10.1016/j.mtphys.2021.100431.

(154) Ling, C.; Zhang, Y.; Li, Q.; Bai, X.; Shi, L.; Wang, J. New Mechanism for N_2 Reduction: The Essential Role of Surface Hydrogenation. *J. Am. Chem. Soc.* **2019**, *141* (45), 18264–18270. https://doi.org/10.1021/jacs.9b09232.

(155) Wang, F.; Cannon, A. T.; Bhattacharya, M.; Baumgarten, R.; VanderLinden, R. T.; Saouma, C. T. Hydrogenation and Electrocatalytic Reduction of Carbon Dioxide to Formate with a Single Co Catalyst. *Chem. Commun.* **2020**, *56* (81), 12142–12145. https://doi.org/10.1039/D0CC04310A.

(156) Roessler, A.; Dossenbach, O.; Rys, P. Electrocatalytic Hydrogenation of Indigo: Process Optimization and Scale-Up in a Flow Cell. *J. Electrochem. Soc.* **2003**, *150* (1), D1. https://doi.org/10.1149/1.1521757.

(157) Segura, S. G.; Lopes, M. L.; Hristovski, K.; Westerhoff, P. Electrocatalytic Reduction of Nitrate: Fundamentals to Full-Scale Water Treatment Applications. *Appl. Catal. B Enviromental* **2018**, *236*, 546–568.

(158) Sheets, B. L.; Botte, G. G. Electrochemical Nitrogen Reduction to Ammonia under Mild Conditions Enabled by a Polymer Gel Electrolyte. *Chem. Commun.* **2018**, *54* (34), 4250–4253. https://doi.org/10.1039/C8CC00657A.

(159) Boerner, L. K. Industrial Ammonia Production Emits More CO2 than Any Other Chemical-Making Reaction. Chemists Want to Change That. *Chem. Eng. News* **2019**, *97* (24).

(160) Yao, Q.; Chen, J.; Xiao, S.; Zhang, Y.; Zhou, X. Selective Electrocatalytic Reduction of Nitrate to Ammonia with Nickel Phosphide. *ACS Appl. Mater. Interfaces* **2021**, *13* (26), 30458–30467. https://doi.org/10.1021/acsami.0c22338.

(161) Martinez, J.; Ortiz, A.; Ortiz, I. State of the Art and Perspectives of the Catalytic and Electrocatalytic Reduction of Aqueous Nitrates.Pdf. *Appl. Catal. B Enviromental* **2017**, *207*, 42–59.

(162) Zhang, X.; Wang, Y.; Liu, C.; Yu, Y.; Lu, S.; Zhang, B. Recent Advances in Non-Noble Metal Electrocatalysts for Nitrate Reduction. *Chem. Eng. J.* **2021**, *403*, 126269. https://doi.org/10.1016/j.cej.2020.126269.

(163) Duca, M.; Koper, M. T. M. Powering Denitrification: The Perspectives of Electrocatalytic Nitrate Reduction. *Energy Environ. Sci.* **2012**, *5* (12), 9726. https://doi.org/10.1039/c2ee23062c.

(164) Wang, Z.; Richards, D.; Singh, N. Recent Discoveries in the Reaction Mechanism of Heterogeneous Electrocatalytic Nitrate Reduction. *Catal. Sci. Technol.* **2021**, *11* (3), 705–725. https://doi.org/10.1039/D0CY02025G.

(165) da Cunha, M. C. P. M.; Weber, M.; Nart, F. C. On the Adsorption and Reduction of NO3− Ions at Au and Pt Electrodes Studied by in Situ FTIR Spectroscopy. *J. Electroanal. Chem.* **1996**, *414* (2), 163–170. https://doi.org/10.1016/0022-0728(96)04697-9.

(166) Vooys, A. C. A. de; Santen, R. A. van; Veen, J. A. R. van. Electrocatalytic Reduction of NO3- Palladium/Copper Electrodes. *J. Mol. Catal.* **2000**, *154*, 203–215.

(167) Szymczyk, A.; Labbez, C.; Fievet, P.; Vidonne, A.; Foissy, A.; Pagetti, J. Contribution of Convection, Diffusion and Migration to Electrolyte Transport through Nanofiltration Membranes. *Adv. Colloid Interface Sci.* **2003**, *103* (1), 77–94. https://doi.org/10.1016/S0001-8686(02)00094-5.

(168) Dima, G. E.; de Vooys, A. C. A.; Koper, M. T. M. Electrocatalytic Reduction of Nitrate at Low Concentration on Coinage and Transition-Metal Electrodes in Acid Solutions. *J. Electroanal. Chem.* **2003**, *554–555*, 15–23. https://doi.org/10.1016/S0022-0728(02)01443-2.

(169) Li, J.; Zhan, G.; Yang, J.; Quan, F.; Mao, C.; Liu, Y.; Wang, B.; Lei, F.; Li, L.; Chan, A. W. M.; Xu, L.; Shi, Y.; Du, Y.; Hao, W.; Wong, P. K.; Wang, J.; Dou, S.-X.; Zhang, L.; Yu, J. C. Efficient Ammonia Electrosynthesis from Nitrate on Strained Ruthenium Nanoclusters. *J. Am. Chem. Soc.* **2020**, *142* (15), 7036–7046. https://doi.org/10.1021/jacs.0c00418.

(170) da Cunha, M. C. P. M.; De Souza, J. P. I.; Nart, F. C. Reaction Pathways for Reduction of Nitrate Ions on Platinum, Rhodium, and Platinum−Rhodium Alloy Electrodes. *Langmuir* **2000**, *16* (2), 771–777. https://doi.org/10.1021/la990638s.

(171) Lim, J.; Liu, C.-Y.; Park, J.; Liu, Y.-H.; Senftle, T. P.; Lee, S. W.; Hatzell, M. C. Structure Sensitivity of Pd Facets for Enhanced Electrochemical Nitrate Reduction to Ammonia. *ACS Catal.* **2021**, *11* (12), 7568–7577. https://doi.org/10.1021/acscatal.1c01413.

(172) American Chemical Society. *Endangered Elements*. Green Chemistry. https://www.acs.org/content/acs/en/greenchemistry/research-innovation/endangered-elements.html.

(173) Chaplin, B. P.; Reinhard, M.; Schneider, W. F.; Schüth, C.; Shapley, J. R.; Strathmann, T. J.; Werth, C. J. Critical Review of Pd-Based Catalytic Treatment of Priority Contaminants in Water. *Environ. Sci. Technol.* **2012**, *46* (7), 3655–3670. https://doi.org/10.1021/es204087q.

(174) Chirik, P.; Morris, R. Getting Down to Earth: The Renaissance of Catalysis with Abundant Metals. *Acc. Chem. Reserach* **2015**, *48* (9). https://doi.org/10.1021/acs.accounts.5b00385.

(175) Choe, J. K.; Bergquist, A. M.; Jeong, S.; Guest, J. S.; Werth, C. J.; Strathmann, T. J. Performance and Life Cycle Environmental Benefits of Recycling Spent Ion Exchange Brines by Catalytic Treatment of Nitrate. *Water Res.* **2015**, *80*, 267–280. https://doi.org/10.1016/j.watres.2015.05.007.

(176) Esposito, D. V.; Chen, J. G. Monolayer Platinum Supported on Tungsten Carbides as Low-Cost Electrocatalysts: Opportunities and Limitations. *Energy Environ. Sci.* **2011**, *4* (10), 3900. https://doi.org/10.1039/c1ee01851e.

(177) Stirling, R.; Walker, W. S.; Westerhoff, P.; Garcia-Segura, S. Techno-Economic Analysis to Identify Key Innovations Required for Electrochemical Oxidation as Point-of-Use Treatment Systems. *Electrochimica Acta* **2020**, *338*, 135874. https://doi.org/10.1016/j.electacta.2020.135874.

(178) Cerrón-Calle, G. A.; Fajardo, A. S.; Sánchez-Sánchez, C. M.; Garcia-Segura, S. Highly Reactive Cu-Pt Bimetallic 3D-Electrocatalyst for Selective Nitrate Reduction to Ammonia. *Appl. Catal. B Environ.* **2022**, *302*, 120844. https://doi.org/10.1016/j.apcatb.2021.120844.

(179) Werth, C. J.; Yan, C.; Troutman, J. P. Factors Impeding Replacement of Ion Exchange with (Electro)Catalytic Treatment for Nitrate Removal from Drinking Water. *ACS EST Eng.* **2021**, *1* (1), 6–20. https://doi.org/10.1021/acsestengg.0c00076.

(180) Lim, J.; Fernández, C. A.; Lee, S. W.; Hatzell, M. C. Ammonia and Nitric Acid Demands for Fertilizer Use in 2050. *ACS Energy Lett.* **2021**, *6* (10), 3676–3685. https://doi.org/10.1021/acsenergylett.1c01614.

(181) *Metallurgy*. Encyclopædia Britannica. https://www.britannica.com/science/metallurgy (accessed 2020-09-04).

(182) Wang, J.; Teng, W.; Ling, L.; Fan, J.; Zhang, W.; Deng, Z. Nanodenitrification with Bimetallic Nanoparticles Confined in N-Doped Mesoporous Carbon. *Environ. Sci. Nano* **2020**, *7* (5), 1496–1506. https://doi.org/10.1039/D0EN00087F.

(183) Simpson, B. K.; Johnson, D. C. Electrocatalysis of Nitrate Reduction at Copper-Nickel Alloy Electrodes in Acidic Media. *Electroanalysis* **2004**, *16* (7), 532–538.

(184) Arora, N.; Thangavelu, K.; Karanikolos, G. N. Bimetallic Nanoparticles for Antimicrobial Applications. *Front. Chem.* **2020**, *8*, 412. https://doi.org/10.3389/fchem.2020.00412.

(185) Sagoff, J. *Two Metals Are Better than One*; Press Release; Argonne National Laboratory, 2014. https://www.anl.gov/article/two-metals-are-better-than-one.

(186) Huang, W.-H.; Li, X.-M.; Yu, D.-Y.; Yang, X.-F.; Wang, L.-F.; Liu, P.-B.; Zhang, J. CoMo-Bimetallic N-Doped Porous Carbon Materials Embedded with Highly Dispersed Pt Nanoparticles as PH-Universal Hydrogen Evolution Reaction Electrocatalysts. *Nanoscale* **2020**, *12* (38), 19804–19813. https://doi.org/10.1039/D0NR04418K.

(187) Bae, S.-E.; Stewart, K. L.; Gewirth, A. A. Nitrate Adsorption and Reduction on Cu(100) in Acidic Solution. *J. Am. Chem. Soc.* **2007**, *129* (33), 10171–10180. https://doi.org/10.1021/ja071330n.

(188) Zhang, Y.; Zhao, Y.; Chen, Z.; Wang, L.; Wu, P.; Wang, F. Electrochemical Reduction of Nitrate via Cu/Ni Composite Cathode Paired with Ir-Ru/Ti Anode: High Efficiency and N2 Selectivity. *Electrochimica Acta* **2018**, *291*, 151–160. https://doi.org/10.1016/j.electacta.2018.08.154.

(189) Rosca, V.; Duca, M.; de Groot, M. T.; Koper, M. T. M. Nitrogen Cycle Electrocatalysis. *Chem. Rev.* **2009**, *109* (6), 2209–2244. https://doi.org/10.1021/cr8003696.

(190) Wang, Y.; Zhou, W.; Jia, R.; Yu, Y.; Zhang, B. Unveiling the Activity Origin of a Copper-based Electrocatalyst for Selective Nitrate Reduction to Ammonia. *Angew. Chem.* **2020**, *132* (13), 5388–5392. https://doi.org/10.1002/ange.201915992.

(191) Wang, S.; Ichihara, F.; Pang, H.; Chen, H.; Ye, J. Nitrogen Fixation Reaction Derived from Nanostructured Catalytic Materials. *Adv. Funct. Mater.* **2018**, *28* (50), 1803309. https://doi.org/10.1002/adfm.201803309.

(192) Li, L.; Tang, C.; Yao, D.; Zheng, Y.; Qiao, S.-Z. Electrochemical Nitrogen Reduction: Identification and Elimination of Contamination in Electrolyte. *ACS Energy Lett.* **2019**, *4* (9), 2111–2116. https://doi.org/10.1021/acsenergylett.9b01573.

(193) Xu, Y.; Ren, K.; Ren, T.; Wang, M.; Liu, M.; Wang, Z.; Li, X.; Wang, L.; Wang, H. Cooperativity of Cu and Pd Active Sites in CuPd Aerogels Enhances Nitrate Electroreduction to Ammonia. *Chem. Commun.* **2021**, *57* (61), 7525–7528. https://doi.org/10.1039/D1CC02105B.

(194) Su, L.; Han, D.; Zhu, G.; Xu, H.; Luo, W.; Wang, L.; Jiang, W.; Dong, A.; Yang, J. Tailoring the Assembly of Iron Nanoparticles in Carbon Microspheres toward High-Performance Electrocatalytic Denitrification. *Nano Lett.* **2019**, *19* (8), 5423–5430. https://doi.org/10.1021/acs.nanolett.9b01925.

(195) Hu, Y.; Wu, P.; Yin, Y.; Zhang, H.; Cai, C. Effects of Structure, Composition, and Carbon Support Properties on the Electrocatalytic Activity of Pt-Ni-Graphene Nanocatalysts for the Methanol Oxidation. *Appl. Catal. B Environ.* **2012**, *111–112*, 208–217. https://doi.org/10.1016/j.apcatb.2011.10.001.

(196) Reddy, K. Nitrate Removal from Groundwater Using Catalytic Reduction. *Water Res.* **2000**, *34* (3), 995–1001. https://doi.org/10.1016/S0043-1354(99)00227-4.

(197) Sun, C.; Li, F.; An, H.; Li, Z.; Bond, A. M.; Zhang, J. Facile Electrochemical Co-Deposition of Metal (Cu, Pd, Pt, Rh) Nanoparticles on Reduced Graphene Oxide for Electrocatalytic Reduction of Nitrate/Nitrite. *Electrochimica Acta* **2018**, *269*, 733–741. https://doi.org/10.1016/j.electacta.2018.03.005.

(198) Wang, Y.; Qu, J.; Wu, R.; Lei, P. The Electrocatalytic Reduction of Nitrate in Water on Pd/Sn-Modified Activated Carbon Fiber Electrode. *Water Res.* **2006**, *40* (6), 1224–1232.

(199) Marcos-Hernández, M.; Antonio Cerrón-Calle, G.; Ge, Y.; Garcia-Segura, S.; Sánchez-Sánchez, C. M.; Fajardo, A. S.; Villagrán, D. Effect of Surface Functionalization of Fe3O4 Nano-Enabled Electrodes on the Electrochemical Reduction of Nitrate. *Sep. Purif. Technol.* **2022**, *282*, 119771. https://doi.org/10.1016/j.seppur.2021.119771.

(200) Teng, W.; Bai, N.; Liu, Y.; Liu, Y.; Fan, J.; Zhang, W. Selective Nitrate Reduction to Dinitrogen by Electrocatalysis on Nanoscale Iron Encapsulated in Mesoporous Carbon. *Environ. Sci. Technol.* **2018**, *52* (1), 230–236. https://doi.org/10.1021/acs.est.7b04775.

(201) Duan, W.; Li, G.; Lei, Z.; Zhu, T.; Xue, Y.; Wei, C.; Feng, C. Highly Active and Durable Carbon Electrocatalyst for Nitrate Reduction Reaction. *Water Res.* **2019**, *161*, 126–135. https://doi.org/10.1016/j.watres.2019.05.104.

(202) Yang, Y.; Shin, J.; Jasper, J. T.; Hoffmann, M. R. Multilayer Heterojunction Anodes for Saline Wastewater Treatment: Design Strategies and Reactive Species Generation Mechanisms. *Environ. Sci. Technol.* **2016**, *50* (16), 8780–8787. https://doi.org/10.1021/acs.est.6b00688.

(203) Yang, Y.; Hoffmann, M. R. Synthesis and Stabilization of Blue-Black TiO $_2$ Nanotube Arrays for Electrochemical Oxidant Generation and Wastewater Treatment. *Environ. Sci. Technol.* **2016**, *50* (21), 11888–11894. https://doi.org/10.1021/acs.est.6b03540.

(204) Zhang, C.; He, D.; Ma, J.; Waite, T. D. Active Chlorine Mediated Ammonia Oxidation Revisited: Reaction Mechanism, Kinetic Modelling and Implications. *Water Res.* **2018**, *145*, 220–230. https://doi.org/10.1016/j.watres.2018.08.025.

(205) Garcia-Segura, S.; Mostafa, E.; Baltruschat, H. Electrogeneration of Inorganic Chloramines on Boron-Doped Diamond Anodes during Electrochemical Oxidation of Ammonium Chloride, Urea and Synthetic Urine Matrix. *Water Res.* **2019**, *160*, 107–117. https://doi.org/10.1016/j.watres.2019.05.046.

(206) Shao, Y.; Yin, G.; Gao, Y.; Shi, P. Durability Study of Pt∕C and Pt∕CNTs Catalysts under Simulated PEM Fuel Cell Conditions. *J. Electrochem. Soc.* **2006**, *153* (6), A1093. https://doi.org/10.1149/1.2191147.

(207) Chen, H.; Müller, M. B.; Gilmore, K. J.; Wallace, G. G.; Li, D. Mechanically Strong, Electrically Conductive, and Biocompatible Graphene Paper. *Adv. Mater.* **2008**, *20* (18), 3557–3561. https://doi.org/10.1002/adma.200800757.

(208) Rao, S.; Simha, T. G. A.; Roa, K. P.; Kumar, R. Carbon Composites Are Becoming Competitive And Cost Effective. *Infosys* **2018**, 12.

(209) Sheng, Z.-H.; Shao, L.; Chen, J.-J.; Bao, W.-J.; Wang, F.-B.; Xia, X.-H. Catalyst-Free Synthesis of Nitrogen-Doped Graphene *via* Thermal Annealing Graphite Oxide with Melamine and Its Excellent Electrocatalysis. *ACS Nano* **2011**, *5* (6), 4350–4358. https://doi.org/10.1021/nn103584t.

(210) Fei, H.; Ye, R.; Ye, G.; Gong, Y.; Peng, Z.; Fan, X.; Samuel, E. L. G.; Ajayan, P. M.; Tour, J. M. Boron- and Nitrogen-Doped Graphene Quantum Dots/Graphene Hybrid Nanoplatelets as Efficient Electrocatalysts for Oxygen Reduction. *ACS Nano* **2014**, *8* (10), 10837–10843. https://doi.org/10.1021/nn504637y.

(211) Gao, J.; Jiang, B.; Ni, C.; Qi, Y.; Bi, X. Enhanced Reduction of Nitrate by Noble Metal-Free Electrocatalysis on P Doped Three-Dimensional Co3O4 Cathode: Mechanism Exploration from Both Experimental and DFT Studies. *Chem. Eng. J.* **2020**, *382*, 123034. https://doi.org/10.1016/j.cej.2019.123034.

(212) Hammer, B.; Nørskov, J. K. Theoretical Surface Science and Catalysis—Calculations and Concepts. In *Advances in Catalysis*; Elsevier, 2000; Vol. 45, pp 71–129. https://doi.org/10.1016/S0360-0564(02)45013-4.

(213) Liu, L.; Zhao, Q.; Liu, R.; Zhu, L. Hydrogen Adsorption-Induced Catalytic Enhancement over Cu Nanoparticles Immobilized by Layered Ti3C2 MXene. *Appl. Catal. B Environ.* **2019**, *252*, 198–204. https://doi.org/10.1016/j.apcatb.2019.04.026.

(214) Li, C.; Li, K.; Chen, C.; Tang, Q.; Sun, T.; Jia, J. Electrochemical Removal of Nitrate Using a Nanosheet Structured Co3O4/Ti Cathode: Effects of Temperature, Current and PH Adjusting. *Sep. Purif. Technol.* **2020**, *237*, 116485. https://doi.org/10.1016/j.seppur.2019.116485.

(215) Yang, M.; Wang, J.; Shuang, C.; Li, A. The Improvement on Total Nitrogen Removal in Nitrate Reduction by Using a Prepared CuO–Co3O4/Ti Cathode. *Chemosphere* **2020**, *255*, 126970. https://doi.org/10.1016/j.chemosphere.2020.126970.

(216) Liu, F.; Liu, K.; Li, M.; Hu, S.; Li, J.; Lei, X.; Liu, X. Fabrication and Characterization of a Ni-TNTA Bimetallic Nanoelectrode to Electrochemically Remove Nitrate from Groundwater. *Chemosphere* **2019**, *223*, 560–568. https://doi.org/10.1016/j.chemosphere.2019.02.028.

(217) Garcia-Segura, S. Opportunities for Nanotechnology to Enhance Electrochemical Treatment of Pollutants in Potable Water and Industrial Wastewater – a Perspective. *Environ. Sci.* **2020**, 18.

(218) Najmudin, S.; González, P. J.; Trincão, J.; Coelho, C.; Mukhopadhyay, A.; Cerqueira, N. M. F. S. A.; Romão, C. C.; Moura, I.; Moura, J. J. G.; Brondino, C. D.; Romão, M. J. Periplasmic Nitrate Reductase Revisited: A Sulfur Atom Completes the Sixth Coordination of the Catalytic Molybdenum. *JBIC J. Biol. Inorg. Chem.* **2008**, *13* (5), 737–753. https://doi.org/10.1007/s00775-008-0359-6.

(219) Li, X.; Li, T.; Ma, Y.; Wei, Q.; Qiu, W.; Guo, H.; Shi, X.; Zhang, P.; Asiri, A. M.; Chen, L.; Tang, B.; Sun, X. Boosted Electrocatalytic N_2 Reduction to NH_3 by Defect-Rich MoS$_2$ Nanoflower. *Adv. Energy Mater.* **2018**, *8* (30), 1801357. https://doi.org/10.1002/aenm.201801357.

(220) Li, Z.; Dai, X.; Du, K.; Ma, Y.; Liu, M.; Sun, H.; Ma, X.; Zhang, X. Reduced Graphene Oxide/O-MWCNT Hybrids Functionalized with p-Phenylenediamine as High-Performance MoS$_2$ Electrocatalyst Support for Hydrogen Evolution Reaction. *J. Phys. Chem. C* **2016**, *120* (3), 1478–1487. https://doi.org/10.1021/acs.jpcc.5b09523.

(221) Zhao, K.; Gu, W.; Zhao, L.; Zhang, C.; Peng, W.; Xian, Y. MoS2/Nitrogen-Doped Graphene as Efficient Electrocatalyst for Oxygen Reduction Reaction. *Electrochimica Acta* **2015**, *169*, 142–149. https://doi.org/10.1016/j.electacta.2015.04.044.

(222) De Silva, U.; Masud, J.; Zhang, N.; Hong, Y.; Liyanage, W. P. R.; Asle Zaeem, M.; Nath, M. Nickel Telluride as a Bifunctional Electrocatalyst for Efficient Water Splitting in Alkaline Medium. *J. Mater. Chem. A* **2018**, *6* (17), 7608–7622. https://doi.org/10.1039/C8TA01760C.

(223) Sadaqat, M.; Nisar, L.; Babar, N.-U.-A.; Hussain, F.; Ashiq, M. N.; Shah, A.; Ehsan, M. F.; Najam-Ul-Haq, M.; Joya, K. S. Zinc-Telluride Nanospheres as an Efficient Water Oxidation Electrocatalyst Displaying a Low Overpotential for Oxygen Evolution. *J. Mater. Chem. A* **2019**, *7* (46), 26410–26420. https://doi.org/10.1039/C9TA07171G.

(224) Xia, X.; Wang, L.; Sui, N.; Colvin, V. L.; Yu, W. W. Recent Progress in Transition Metal Selenide Electrocatalysts for Water Splitting. *Nanoscale* **2020**, *12* (23), 12249–12262. https://doi.org/10.1039/D0NR02939D.

(225) Zhang, K.; Li, Y.; Deng, S.; Shen, S.; Zhang, Y.; Pan, G.; Xiong, Q.; Liu, Q.; Xia, X.; Wang, X.; Tu, J. Molybdenum Selenide Electrocatalysts for Electrochemical Hydrogen Evolution Reaction. *ChemElectroChem* **2019**, *6* (14), 3530–3548. https://doi.org/10.1002/celc.201900448.

(226) Li, Y.; Yamaguchi, A.; Yamamoto, M.; Takai, K.; Nakamura, R. Molybdenum Sulfide: A Bioinspired Electrocatalyst for Dissimilatory Ammonia Synthesis with Geoelectrical Current. *J. Phys. Chem. C* **2017**, *121* (4), 2154–2164. https://doi.org/10.1021/acs.jpcc.6b08343.

(227) Richards, D.; Young, S. D.; Goldsmith, B. R.; Singh, N. Electrocatalytic Nitrate Reduction on Rhodium Sulfide Compared to Pt and Rh in the Presence of Chloride. *Catal. Sci. Technol.* **2021**, *11* (22), 7331–7346. https://doi.org/10.1039/D1CY01369F.

(228) Guo, Y.; Park, T.; Yi, J. W.; Henzie, J.; Kim, J.; Wang, Z.; Jiang, B.; Bando, Y.; Sugahara, Y.; Tang, J.; Yamauchi, Y. Nanoarchitectonics for Transition-Metal-Sulfide-Based Electrocatalysts for Water Splitting. *Adv. Mater.* **2019**, *31* (17), 1807134. https://doi.org/10.1002/adma.201807134.

(229) Kang, Y. Interplay between Transition-Metal Dopants and Sulfur Vacancies in MoS2 Electrocatalyst. *Surf. Sci.* **2021**, *704*, 121759. https://doi.org/10.1016/j.susc.2020.121759.

(230) Marks, R.; Schranck, A.; Stillwell, R.; Doudrick, K. Stability of 2H- and 1T-MoS$_2$ in the Presence of Aqueous Oxidants and Its Protection by a Carbon Shell. *RSC Adv.* **2020**, *10* (16), 9324–9334. https://doi.org/10.1039/D0RA00788A.

(231) RAO, C. N. R.; Pisharody, K. P. R. TRANSITION METAL SULFIDES. 64.

(232) de Groot, M. T.; Koper, M. T. M. The Influence of Nitrate Concentration and Acidity on the Electrocatalytic Reduction of Nitrate on Platinum. *J. Electroanal. Chem.* **2004**, *562* (1), 81–94. https://doi.org/10.1016/j.jelechem.2003.08.011.

(233) Kim, D.-G.; Hwang, Y.-H.; Shin, H.-S.; Ko, S.-O. Kinetics of Nitrate Adsorption and Reduction by Nano-Scale Zero Valent Iron (NZVI): Effect of Ionic Strength and Initial PH. *KSCE J. Civ. Eng.* **2016**, *20* (1), 175–187. https://doi.org/10.1007/s12205-015-0464-3.

(234) Garcia-Segura, S.; Nienhauser, A. B.; Fajardo, A. S.; Bansal, R.; Conrad, C. L.; Fortner, J. D.; Marcos-Hernández, M.; Rogers, T.; Villagran, D.; Wong, M. S.; Westerhoff, P. Disparities between Experimental and Environmental Conditions: Research Steps toward Making Electrochemical Water Treatment a Reality. *Curr. Opin. Electrochem.* **2020**, *22*, 9–16. https://doi.org/10.1016/j.coelec.2020.03.001.

(235) Ambrosioni, B.; Barthelemy, A.; Bejan, D.; Bunce, N. J. Electrochemical Reduction of Aqueous Nitrate Ion at Tin Cathodes. *Can. J. Chem.* **2014**, *92* (3), 228–233. https://doi.org/10.1139/cjc-2013-0406.

(236) Katsounaros, I.; Kyriacou, G. Influence of the Concentration and the Nature of the Supporting Electrolyte on the Electrochemical Reduction of Nitrate on Tin Cathode. *Electrochimica Acta* **2007**, *52* (23), 6412–6420. https://doi.org/10.1016/j.electacta.2007.04.050.

(237) Ma, X.; Li, M.; Feng, C.; He, Z. Electrochemical Nitrate Removal with Simultaneous Magnesium Recovery from a Mimicked RO Brine Assisted by in Situ Chloride Ions. *J. Hazard. Mater.* **2020**, *388*, 122085. https://doi.org/10.1016/j.jhazmat.2020.122085.

(238) Cano, A.; Cañizares, P.; Barrera-Díaz, C.; Sáez, C.; Rodrigo, M. A. Use of Conductive-Diamond Electrochemical-Oxidation for the Disinfection of Several Actual Treated Wastewaters. *Chem. Eng. J.* **2012**, *211–212*, 463–469. https://doi.org/10.1016/j.cej.2012.09.071.

(239) Choi, J.; Shim, S.; Yoon, J. Design and Operating Parameters Affecting an Electrochlorination System. *J. Ind. Eng. Chem.* **2013**, *19* (1), 215–219. https://doi.org/10.1016/j.jiec.2012.08.004.

(240) Saunier, B. M.; Selleck, R. E. The Kinetics of Breakpoint Chlorination in Continuous Flow Systems. *J. - Am. Water Works Assoc.* **1979**, *71* (3), 164–172. https://doi.org/10.1002/j.1551-8833.1979.tb04322.x.

(241) Briggs, A. G.; Norrish, R. G. W. The Decomposition of Nitrogen Trichloride Photosensitized by Chlorine. *Proc. R. Soc. Lond. Ser. Math. Phys. Sci.* **1964**, *278* (1372), 27–34. https://doi.org/10.1098/rspa.1964.0043.

(242) *MWH's Water Treatment: Principles and Design*, 3rd ed.; Crittenden, J. C., Montgomery Watson Harza (Firm), Eds.; John Wiley & Sons: Hoboken, N.J, 2012.

(243) Mostafa, E.; Reinsberg, P.; Garcia-Segura, S.; Baltruschat, H. Chlorine Species Evolution during Electrochlorination on Boron-Doped Diamond Anodes: In-Situ Electrogeneration of Cl2, Cl2O and ClO2. *Electrochimica Acta* **2018**, *281*, 831–840. https://doi.org/10.1016/j.electacta.2018.05.099.

(244) Szpyrkowicz, L.; Daniele, S.; Radaelli, M.; Specchia, S. Removal of NO3− from Water by Electrochemical Reduction in Different Reactor Configurations. *Appl. Catal. B Environ.* **2006**, *66* (1–2), 40–50. https://doi.org/10.1016/j.apcatb.2006.02.020.

(245) Maxwell, B.; Díaz-García, C.; Martínez-Sánchez, J. J.; Álvarez-Rogel, J. Increased Brine Concentration Increases Nitrate Reduction Rates in Batch Woodchip Bioreactors Treating Brine from Desalination. *Desalination* **2020**, *495*, 114629. https://doi.org/10.1016/j.desal.2020.114629.

(246) Wu, B. Surface and Interface Control of Noble Metal Nanocrystals for Catalytic and Electrocatalytic Applications. *Nano Today* **2013**, *8*, 168–197.

(247) Sasaki, K.; Naohara, H.; Cai, Y.; Choi, Y. M.; Liu, P.; Vukmirovic, M. B.; Wang, J. X.; Adzic, R. R. Core-Protected Platinum Monolayer Shell High-Stability Electrocatalysts for Fuel-Cell Cathodes. *Angew Chem* **2010**, 6.

(248) van Langevelde, P. H.; Katsounaros, I.; Koper, M. T. M. Electrocatalytic Nitrate Reduction for Sustainable Ammonia Production. *Joule* **2021**, *5* (2), 290–294. https://doi.org/10.1016/j.joule.2020.12.025.

(249) Koh, S.; Leisch, J.; Toney, M. F.; Strasser, P. Structure-Activity-Stability Relationships of Pt−Co Alloy Electrocatalysts in Gas-Diffusion Electrode Layers. *J. Phys. Chem. C* **2007**, *111* (9), 3744–3752. https://doi.org/10.1021/jp067269a.

(250) Zhang, Y.; Gao, L.; Hensen, E. J. M.; Hofmann, J. P. Evaluating the Stability of Co 2 P Electrocatalysts in the Hydrogen Evolution Reaction for Both Acidic and Alkaline Electrolytes. *ACS Energy Lett.* **2018**, *3* (6), 1360–1365. https://doi.org/10.1021/acsenergylett.8b00514.

(251) Wijten, J. H. J.; Riemersma, R. L.; Gauthier, J.; Mandemaker, L. D. B.; Verhoeven, M. W. G. M. (Tiny); Hofmann, J. P.; Chan, K.; Weckhuysen, B. M. Electrolyte Effects on the Stability of Ni−Mo Cathodes for the Hydrogen Evolution Reaction. *ChemSusChem* **2019**, *12* (15), 3491–3500. https://doi.org/10.1002/cssc.201900617.

(252) Lin, C.; Tang, A.; Mu, H.; Wang, W.; Wang, C. Aging Mechanisms of Electrode Materials in Lithium-Ion Batteries for Electric Vehicles. *J. Chem.* **2015**, *2015*, 1–11. https://doi.org/10.1155/2015/104673.

(253) Popov, B. N.; Lee, J.-W.; Djukic, M. B. Hydrogen Permeation and Hydrogen-Induced Cracking. In *Handbook of Environmental Degradation of Materials*; Elsevier, 2018; pp 133–162. https://doi.org/10.1016/B978-0-323-52472-8.00007-1.

(254) Djukic, M. B.; Zeravcic, V. S.; Bakic, G.; Sedmak, A.; Rajicic, B. Hydrogen Embrittlement of Low Carbon Structural Steel. *Procedia Mater. Sci.* **2014**, *3*, 1167–1172. https://doi.org/10.1016/j.mspro.2014.06.190.

(255) Djukic, M. B.; Sijacki Zeravcic, V.; Bakic, G. M.; Sedmak, A.; Rajicic, B. Hydrogen Damage of Steels: A Case Study and Hydrogen Embrittlement Model. *Eng. Fail. Anal.* **2015**, *58*, 485–498. https://doi.org/10.1016/j.engfailanal.2015.05.017.

(256) Liu, Q.; Atrens, A. Reversible Hydrogen Trapping in a 3.5NiCrMoV Medium Strength Steel. *Corros. Sci.* **2015**, *96*, 112–120. https://doi.org/10.1016/j.corsci.2015.04.011.

(257) Kobayashi, M.; Matsui, T.; Murakami, Y. Mechanism of Creation of Compressive Residual Stress by Shot Peening. 7.

(258) You, B.; Tang, M. T.; Tsai, C.; Abild-Pedersen, F.; Zheng, X.; Li, H. Enhancing Electrocatalytic Water Splitting by Strain Engineering. *Adv. Mater.* **2019**, *31* (17), 1807001. https://doi.org/10.1002/adma.201807001.

(259) Garrick, T. R.; Kanneganti, K.; Huang, X.; Weidner, J. W. Modeling Volume Change Due to Intercalation into Porous Electrodes. *J. Electrochem. Soc.* **2014**, *161* (8), E3297–E3301. https://doi.org/10.1149/2.030408jes.

(260) Muna, G. W.; Partridge, M.; Sirhan, H.; VerVaet, B.; Guerra, N.; Garner, H. Electrochemical Detection of Steroid Hormones Using a Nickel-Modified Glassy Carbon Electrode. *Electroanalysis* **2014**, *26* (10), 2145–2151. https://doi.org/10.1002/elan.201400361.

(261) Bell, D.; Sengpiel, R.; Wessling, M. Metallized Hollow Fiber Membranes for Electrochemical Fouling Control. *J. Membr. Sci.* **2020**, *594*, 117397. https://doi.org/10.1016/j.memsci.2019.117397.

(262) Chen, S. C.; Wan, C. F.; Chung, T.-S. Enhanced Fouling by Inorganic and Organic Foulants on Pressure Retarded Osmosis (PRO) Hollow Fiber Membranes under High Pressures. *J. Membr. Sci.* **2015**, *479*, 190–203. https://doi.org/10.1016/j.memsci.2015.01.037.

(263) Bixler, G. D.; Bhushan, B. Biofouling: Lessons from Nature. *Philos. Trans. R. Soc. Math. Phys. Eng. Sci.* **2012**, *370* (1967), 2381–2417. https://doi.org/10.1098/rsta.2011.0502.

(264) Díez, B.; Amariei, G.; Rosal, R. Electrospun Composite Membranes for Fouling and Biofouling Control. *Ind. Eng. Chem. Res.* **2018**, *57* (43), 14561–14570. https://doi.org/10.1021/acs.iecr.8b04011.

(265) Geesey, G. G. *Biofouling and Biocorrosion in Industrial Water Systems*; Taylor & Francis, 1994.

(266) Hanssen, B. L.; Siraj, S.; Wong, D. K. Y. Recent Strategies to Minimise Fouling in Electrochemical Detection Systems. *Rev. Anal. Chem.* **2016**, *35* (1), 1–28. https://doi.org/10.1515/revac-2015-0008.

(267) Thevenot, P.; Hu, W.; Tang, L. SURFACE CHEMISTRY INFLUENCE IMPLANT BIOCOMPATIBILITY. **2011**, 21.

(268) Wilson, C. J.; Clegg, R. E.; Leavesley, D. I.; Pearcy, M. J. Mediation of Biomaterial–Cell Interactions by Adsorbed Proteins: A Review. *Tissue Eng.* **2005**, *11* (1–2), 1–18. https://doi.org/10.1089/ten.2005.11.1.

(269) Rice, D.; Rajwade, K.; Zuo, K.; Bansal, R.; Li, Q.; Garcia-Segura, S.; Perreault, F. Electrochemically-Active Carbon Nanotube Coatings for Biofouling Mitigation: Cleaning Kinetics and Energy Consumption for Cathodic and Anodic Regimes. *J. Colloid Interface Sci.* **2021**, *603*, 391–397. https://doi.org/10.1016/j.jcis.2021.06.090.

(270) Rice, D.; Westerhoff, P.; Perreault, F.; Garcia-Segura, S. Electrochemical Self-Cleaning Anodic Surfaces for Biofouling Control during Water Treatment. *Electrochem. Commun.* **2018**, *96*, 83–87. https://doi.org/10.1016/j.elecom.2018.10.002.

(271) Lee, E.-J.; Kim, Y.-H.; Lee, C.-H.; Kim, H.-S.; Kim, H.-S. Effect of Different Physical Conditions on Fouling Control in In-Situ Chemical Cleaning in Place (CIP) for Flat Sheet Membranes Fouled by Secondary Effluents. *Chem. Eng. J.* **2016**, *302*, 128–136. https://doi.org/10.1016/j.cej.2016.05.039.

(272) Weng, Z.; Zhang, X.; Wu, Y.; Huo, S.; Jiang, J.; Liu, W.; He, G.; Liang, Y.; Wang, H. Self-Cleaning Catalyst Electrodes for Stabilized CO_2 Reduction to Hydrocarbons. *Angew. Chem.* **2017**, *129* (42), 13315–13319. https://doi.org/10.1002/ange.201707478.

(273) Chung, C. M.; Tobino, T.; Cho, K.; Yamamoto, K. Alleviation of Membrane Fouling in a Submerged Membrane Bioreactor with Electrochemical Oxidation Mediated by In-Situ Free Chlorine Generation. *Water Res.* **2016**, *96*, 52–61. https://doi.org/10.1016/j.watres.2016.03.041.

(274) Chow, H.; Pham, A. L.-T. Mitigating Electrode Fouling in Electrocoagulation by Means of Polarity Reversal: The Effects of Electrode Type, Current Density, and Polarity Reversal Frequency. *Water Res.* **2021**, *197*, 117074. https://doi.org/10.1016/j.watres.2021.117074.

(275) Sun, J.; Gao, W.; Fei, H.; Zhao, G. Efficient and Selective Electrochemical Reduction of Nitrate to N2 by Relay Catalytic Effects of Fe-Ni Bimetallic Sites on MOF-Derived Structure. *Appl. Catal. B Environ.* **2022**, *301*, 120829. https://doi.org/10.1016/j.apcatb.2021.120829.

(276) Flores, K.; Cerrón-Calle, G. A.; Valdes, C.; Atrashkevich, A.; Castillo, A.; Morales, H.; Parsons, J. G.; Garcia-Segura, S.; Gardea-Torresdey, J. L. Outlining Key Perspectives for the Advancement of Electrocatalytic Remediation of Nitrate from Polluted Waters. *ACS EST Eng.* **2022**, *2* (5), 746–768. https://doi.org/10.1021/acsestengg.2c00052.

(277) Xu, H.; Ma, Y.; Chen, J.; Zhang, W.; Yang, J. Electrocatalytic Reduction of Nitrate – a Step towards a Sustainable Nitrogen Cycle. *Chem. Soc. Rev.* **2022**, *51* (7), 2710–2758. https://doi.org/10.1039/D1CS00857A.

(278) Zhao, Y.; Liu, Y.; Zhang, Z.; Mo, Z.; Wang, C.; Gao, S. Flower-like Open-Structured Polycrystalline Copper with Synergistic Multi-Crystal Plane for Efficient Electrocatalytic Reduction of Nitrate to Ammonia. *Nano Energy* **2022**, *97*, 107124. https://doi.org/10.1016/j.nanoen.2022.107124.

(279) Gao, J.; Jiang, B.; Ni, C.; Qi, Y.; Zhang, Y.; Oturan, N.; Oturan, M. A. Non-Precious Co3O4-TiO2/Ti Cathode Based Electrocatalytic Nitrate Reduction: Preparation, Performance and Mechanism. *Appl. Catal. B Environ.* **2019**, *254*, 391–402. https://doi.org/10.1016/j.apcatb.2019.05.016.

(280) Archna; Sharma, S. K.; Sobti, R. C. Nitrate Removal from Ground Water: A Review. *E-J. Chem.* **2012**, *9* (4), 1667–1675. https://doi.org/10.1155/2012/154616.

(281) He, L.; Yao, F.; Zhong, Y.; Tan, C.; Hou, K.; Pi, Z.; Chen, S.; Li, X.; Yang, Q. Achieving High-Performance Electrocatalytic Reduction of Nitrate by N-Rich Carbon-Encapsulated Ni-Cu Bimetallic Nanoparticles Supported Nickel Foam Electrode. *J. Hazard. Mater.* **2022**, *436*, 129253. https://doi.org/10.1016/j.jhazmat.2022.129253.

(282) Feng, T.; Wang, J.; Wang, Y.; Yu, C.; Zhou, X.; Xu, B.; László, K.; Li, F.; Zhang, W. Selective Electrocatalytic Reduction of Nitrate to Dinitrogen by Cu2O Nanowires with

Mixed Oxidation-State. *Chem. Eng. J.* **2022**, *433*, 133495. https://doi.org/10.1016/j.cej.2021.133495.

(283) Thorgersen, M. P.; Lancaster, W. A.; Vaccaro, B. J.; Poole, F. L.; Rocha, A. M.; Mehlhorn, T.; Pettenato, A.; Ray, J.; Waters, R. J.; Melnyk, R. A.; Chakraborty, R.; Hazen, T. C.; Deutschbauer, A. M.; Arkin, A. P.; Adams, M. W. W. Molybdenum Availability Is Key to Nitrate Removal in Contaminated Groundwater Environments. *Appl. Environ. Microbiol.* **2015**, *81* (15), 4976–4983. https://doi.org/10.1128/AEM.00917-15.

(284) Bae, M.; Oh, J. K.; Liu, S.; Nagabandi, N.; Yegin, Y.; DeFlorio, W.; Cisneros-Zevallos, L.; Scholar, E. M. A. Nanotoxicity of 2D Molybdenum Disulfide, MoS2, Nanosheets on Beneficial Soil Bacteria, Bacillus Cereus and Pseudomonas Aeruginosa. *Nanomaterials* **2021**, *11* (6), 1453. https://doi.org/10.3390/nano11061453.

(285) Benck, J. D.; Hellstern, T. R.; Kibsgaard, J.; Chakthranont, P.; Jaramillo, T. F. Catalyzing the Hydrogen Evolution Reaction (HER) with Molybdenum Sulfide Nanomaterials. *ACS Catal.* **2014**, *4* (11), 3957–3971. https://doi.org/10.1021/cs500923c.

(286) Abbasi, P.; Asadi, M.; Liu, C.; Sharifi-Asl, S.; Sayahpour, B.; Behranginia, A.; Zapol, P.; Shahbazian-Yassar, R.; Curtiss, L. A.; Salehi-Khojin, A. Tailoring the Edge Structure of Molybdenum Disulfide toward Electrocatalytic Reduction of Carbon Dioxide. *ACS Nano* **2017**, *11* (1), 453–460. https://doi.org/10.1021/acsnano.6b06392.

(287) Geng, X.; Zhang, H.; Ye, W.; Ma, Y.; Zhong, H. Ni–Pt/C as Anode Electrocatalyst for a Direct Borohydride Fuel Cell. *J. Power Sources* **2008**, *185* (2), 627–632. https://doi.org/10.1016/j.jpowsour.2008.09.010.

(288) Flores, K.; Valdes, C.; Ramirez, D.; Eubanks, T. M.; Lopez, J.; Hernandez, C.; Alcoutlabi, M.; Parsons, J. G. The Effect of Hybrid Zinc Oxide/Graphene Oxide (ZnO/GO) Nano-Catalysts on the Photocatalytic Degradation of Simazine. *Chemosphere* **2020**, *259*, 127414. https://doi.org/10.1016/j.chemosphere.2020.127414.

(289) Howe, J. Y.; Rawn, C. J.; Jones, L. E.; Ow, H. Improved Crystallographic Data for Graphite. *Powder Diffr.* **2003**, *18* (2), 150–154. https://doi.org/10.1154/1.1536926.

(290) Le Bail, A.; Duroy, H.; Fourquet, J. L. Ab-Initio Structure Determination of LiSbWO6 by X-Ray Powder Diffraction. *Mater. Res. Bull.* **1988**, *23* (3), 447–452. https://doi.org/10.1016/0025-5408(88)90019-0.

(291) Flores, K.; Rand, L. N.; Valdes, C.; Castillo, A.; Cantu, J. M.; Parsons, J. G.; Westerhoff, P.; Gardea-Torresdey, J. L. Targeting Metal Impurities for the Detection and Quantification of Carbon Black Particles in Water via SpICP-MS. *Environ. Sci. Technol.* **2022**, *56* (19), 13719–13727. https://doi.org/10.1021/acs.est.2c03130.

(292) Shang, X.; Hu, W.-H.; Li, X.; Dong, B.; Liu, Y.-R.; Han, G.-Q.; Chai, Y.-M.; Liu, C.-G. Oriented Stacking along Vertical (002) Planes of MoS2: A Novel Assembling Style to Enhance Activity for Hydrogen Evolution. *Electrochimica Acta* **2017**, *224*, 25–31. https://doi.org/10.1016/j.electacta.2016.12.027.

(293) Qin, S.; Lei, W.; Liu, D.; Chen, Y. In-Situ and Tunable Nitrogen-Doping of MoS2 Nanosheets. *Sci. Rep.* **2015**, *4* (1), 7582. https://doi.org/10.1038/srep07582.

(294) Mohammed, M. M. M.; Chun, D.-M. All-Solid-State Supercapacitor Based on MoS2–Graphite Composite Prepared by the Vacuum Kinetic Spray Method. *J. Therm. Spray Technol.* **2019**, *28* (5), 963–973. https://doi.org/10.1007/s11666-019-00875-z.

(295) Gupta, V.; Sharma, N.; Singh, U.; Arif, Mohd.; Singh, A. Higher Oxidation Level in Graphene Oxide. *Optik* **2017**, *143*, 115–124. https://doi.org/10.1016/j.ijleo.2017.05.100.

(296) Thakur, A.; Kumar, S.; Rangra, V. S. Synthesis of Reduced Graphene Oxide (RGO) via Chemical Reduction; Shimla, India, 2015; p 080032. https://doi.org/10.1063/1.4915423.

(297) Guex, L. G.; Sacchi, B.; Peuvot, K. F.; Andersson, R. L.; Pourrahimi, A. M.; Ström, V.; Farris, S.; Olsson, R. T. Experimental Review: Chemical Reduction of Graphene Oxide (GO) to Reduced Graphene Oxide (RGO) by Aqueous Chemistry. *Nanoscale* **2017**, *9* (27), 9562–9571. https://doi.org/10.1039/C7NR02943H.

(298) *CRC Handbook of Chemistry and Physics: A Ready-Reference Book of Chemical and Physical Data*, 92nd ed., 2011–2012.; Haynes, W. M., Lide, D. R., Eds.; CRC Press: Boca Raton, Fla., 2011.

(299) *Treatise on Geochemistry*, Second edition.; Holland, H. D., Turekian, K. K., Eds.; Elsevier: Amsterdam, 2014.

(300) de Vooys, A. C. A.; van Santen, R. A.; van Veen, J. A. R. Electrocatalytic Reduction of NO_3^- on Palladium/Copper Electrodes. *J. Mol. Catal. Chem.* **2000**, *154* (1–2), 203–215. https://doi.org/10.1016/S1381-1169(99)00375-1.

(301) Nitopi, S.; Bertheussen, E.; Scott, S. B.; Liu, X.; Engstfeld, A. K.; Horch, S.; Seger, B.; Stephens, I. E. L.; Chan, K.; Hahn, C.; Nørskov, J. K.; Jaramillo, T. F.; Chorkendorff, I. Progress and Perspectives of Electrochemical CO_2 Reduction on Copper in Aqueous Electrolyte. *Chem. Rev.* **2019**, *119* (12), 7610–7672. https://doi.org/10.1021/acs.chemrev.8b00705.

(302) Perez-Gallent, E.; Figueiredo, M. C.; Katsounaros, I.; Koper, M. T. M. Electrocatalytic Reduction of Nitrate on Copper Single Crystals in Acidic and Alkaline Solutions, 2017.

(303) Reyter, D.; Chamoulaud, G.; Bélanger, D.; Roué, L. Electrocatalytic Reduction of Nitrate on Copper Electrodes Prepared by High-Energy Ball Milling. *J. Electroanal. Chem.* **2006**, *596* (1), 13–24. https://doi.org/10.1016/j.jelechem.2006.06.012.

(304) Arnaut, L. G. *Chemical Kinetics: From Molecular Structure to Chemical Reactivity*, Second edition.; Elsevier: Amsterdam, Netherlands ; Cambridge, MA, 2021.

(305) Rand, L. N.; Flores, K.; Sharma, N.; Gardea-Torresdey, J.; Westerhoff, P. Quantifying Nanoparticle Associated Ti, Ce, Au, and Pd Occurrence in 35 U.S. Surface Waters. *ACS EST Water* **2021**, *1* (10), 2242–2250. https://doi.org/10.1021/acsestwater.1c00206.

(306) Lachas, H.; Richaud, R.; Herod, A. A.; Dugwell, D. R.; Kandiyoti, R.; Jarvis, K. E. Determination of 17 Trace Elements in Coal and Ash Reference Materials by ICP-MS Applied to Milligram Sample Sizes. *The Analyst* **1999**, *124* (2), 177–184. https://doi.org/10.1039/a807849a.

(307) Bicalho, B.; Grant-Weaver, I.; Sinn, C.; Donner, M. W.; Woodland, S.; Pearson, G.; Larter, S.; Duke, J.; Shotyk, W. Determination of Ultratrace (<0.1 Mg/Kg) Elements in Athabasca Bituminous Sands Mineral and Bitumen Fractions Using Inductively Coupled Plasma Sector Field Mass Spectrometry (ICP-SFMS). *Fuel* **2017**, *206*, 248–257. https://doi.org/10.1016/j.fuel.2017.05.095.

(308) *Sax's Dangerous Properties of Industrial Materials*; Lewis, R. J., Ed.; John Wiley & Sons, Inc.: Hoboken, NJ, USA, 2004. https://doi.org/10.1002/0471701343.

(309) Laborda, F.; Jiménez-Lamana, J.; Bolea, E.; Castillo, J. R. Critical Considerations for the Determination of Nanoparticle Number Concentrations, Size and Number Size Distributions by Single Particle ICP-MS. *J. Anal. At. Spectrom.* **2013**, *28* (8), 1220. https://doi.org/10.1039/c3ja50100k.

(310) Liu, M.; Cowley, J. M. Encapsulation of Lanthanum Carbide in Carbon Nanotubes and Carbon Nanoparticles. *Carbon* **1995**, *33* (2), 225–232. https://doi.org/10.1016/0008-6223(94)00140-U.

APPENDIX

SUPPLEMENTARY MATERIAL

S1. ICP-MS Operating Parameters

All quantitative analysis for ICP-MS of diluted digestate was performed by the following timing parameters: sweeps (40), readings (1), replicates (3) with a 50 ms dwell time. A dual detector (pulse & analog) was used for all digestate analysis.

Table S1: Operational parameters for ICP-MS analysis

Description	Standard	Minimum	Maximum
Nebulizer Gas Flow	0.71	0	1.5
AMS Gas Flow	0	0	0.9
Auxiliary Gas Flow	1.2	0.6	2
Plasma Gas Flow	15	10	20
ICP RF Power	1600	400	1600
Analog State Voltage	-1950	-3000	0
Pulse Stage Voltage	1050	0	2500
Discriminator Threshold	10	0	1000
Deflector Voltage	-11	-100	20
Quadrupole Rod Offset	0	-26	26
Cell Entrance Voltage	-11	-60	20
Cell Exit Voltage	-11	-60	20
Cell Rod Offset	-7	-40	10

Table S2: Parameters of the daily performance check

Analyte	Criterion
Be (9)	Intensity > 4500
In (115)	Intensity > 80000
U (238)	Intensity > 60000
Bkgd (220)	Intensity <=3
Ce	Formula: Ce^{++} (70) / Ce (140) <= 0.03
Ce	Formula: CeO (156) / Ce (140) <= 0.025

S2. Digestion Calculations, Dehydrated CB Masses, Statistical Considerations, and SRM Verification

Calculations:

$$\text{NIST certified mass fraction} = \frac{mg\ of\ metal}{kg\ of\ NIST\ SRM}$$

$$expected\ mass\ (mg) = \frac{mg\ of\ metal}{kg\ of\ NIST\ SRM}\ x\ kg\ of\ SRM\ digested$$

$$measured\ mass\ (mg) = measured\ conc\ \left(\frac{\mu g}{L}\right) \times\ digestate\ vol\ (L)\ \times DF\ \times \left(\frac{1\ mg}{1000\ \mu g}\right)$$

$$percent\ recovery = \frac{measured\ mass\ (mg)}{expected\ mass\ (mg)} \times 100\%$$

$$CB\ mass\ fraction = \frac{measured\ mass\ (mg)}{CB\ digested\ (kg)}$$

Table S3: Percent moisture calculated from the dehydration of standard reference materials and commercial carbon black varieties.

Carbon Powder Material	Percent Moisture
NIST SRM 1635a	16.2 %
NIST SRM 1633c	1.1 %
Emperor 2000 CB	12.30 %
Emperor 1800 CB	11.19 %
Monarch 1000 CB	6.12 %
Monarch 800 CB	1.29 %
Monarch 120 CB	0.1 %
Vulcan XC72r	0.54 %

In order to test the reliability of digestion and analysis protocols two standard reference materials (SRM), NIST 1635a, Trace Elements in Coal, and 1633c, Trace Elements in Coal Fly Ash, were utilized to compare the experimental recoveries to certified values. The intention of the

digestion was to break down the organic content of the CB and fully dissolve metal impurities for detection. The first SRM 1635a was closest in carbon mass percentage and metals concentration as seen from preliminary digestions for Emperor 2000 and Monarch 800 CB materials, therefore greater emphasis was placed on this digestion and analysis protocol. In addition, SRM 1635a had the largest variety of metals present which have been verified by ICP-MS, rather than other analytical techniques (i.e., wavelength dispersive X-ray Fluorescence, ICP-OES, instrumental neutron activation analysis). SRM 1633c contained one element of interest, La, that was not contained in 1635a. However, because SRM 1633c is a fly ash material, it has a higher inorganic content and lower carbon content then our commercial CB materials. Following the digestion of each SRM, as described in section 2.1 of the main text, the resulting digestate was diluted and analyzed by ICP-MS for 18 trace metals. Table S4 shows the 18 elements of interest as well as their corresponding mass, correlation coefficient, and slope from the analysis. The dissolved calibration for each metal analyte was comprised of four standard concentrations: 0.1, 1.0, 5.0, 15.0 µg/L. Calibrations with higher concentrations (10, 50, 100, 150 µg/L) were used for Mg and Ti due to their higher expected concentrations in SRM.

Table S4: Element of interest and isotopic mass utilized for ICP-MS analysis, with the corresponding correlation coefficient and calibration slope on the day of analysis.

Element	Mass	Cor.Coeff. (linear)	Slope
Ce	141.909	1	14434x
As	74.9216	0.9999	10335x
Cd	111.903	0.9999	21115x
Co	58.9332	0.9999	91702x
Cr	52.9407	0.9999	8960x
Pb	206.976	0.9999	26998x
La	138.906	0.9999	88868x
Mo	95.9046	0.9999	22148x
Ni	59.9332	0.9998	20026x
Sb	122.904	0.9998	22569x
Sr	85.9094	0.9998	18103x
Ti	47.948	0.9998	69701x
Mn	54.9381	0.9997	123118x
V	50.944	0.9992	94780x
Cu	64.9278	0.994	18067x
Zn	65.926	0.9933	9826x
Mg	25.9826	0.9832	4896x
Ba	136.905	0.9777	15028x

Recoveries from the digestion and analysis of SRM 1635a are presented in Figure S1 as percent recoveries, from the average of nine replicates (three separate tests of three replicates) with standard deviations shown as error bars. The data was evaluated for similarity between the experimental recovery compared to the certified, or reference, mass fractions provided by NIST. Recovery values were categorized as followed: 90 – 110% considered excellent, 90 – 70% adequate, and finally <70% considered poor recoveries for metal impurities. Of the 18 elements, 11 were measured by excellent standard recoveries, 4 by adequate standard recoveries, and finally 3 by poor standard recoveries. In another study which utilized SRM 1635a, similar recoveries were observed for Mn, Co, and Cu, while significant improvements were noted in the present study for V, Pb, Cr, Ni, Mo. For V and Pb, ≈ 30%. In addition the aforementioned study reported extreme overestimations for Cr, Ni, and Mo, while the current study reported excellent recoveries for these metals .[306] These improvements were attributed to a higher microwave power used in our method. Some improvement may also have been achieved by reducing polyatomic interference by choosing

appropriate isotopes, e.g. ^{53}Cr over ^{52}Cr, to circumvent the ^{40}Ar^{12}C$^+$ interference, that appeared to impact the previous study.[105] Of all the metal recoveries, Zn was the only element that suffered from either contamination or polyatomic interferences resulting in an overestimation in concentration (≈200%). This overestimation was further exacerbated when the ^{64}Zn isotope was tested as an alternative.

Compared to a more recent study that utilized nitric acid and small amounts of fluoroboric acid for a microwave assisted digestion, similar recoveries were accomplished for Cr, Mn, Ni, Cu, and V.[307] The present digestion method surpassed the Pb recoveries reported by Bicalho et al, while their Sb recovery was superior. This was most likely due to the fact that fluoroboric acid decomposes to hydrofluoric acid at temperatures above 130°C, which is capable of breaking apart inorganic species that are insoluble in nitric acid.[308] To reduce safety hazards, the use of hydrofluoric acid and its derivatives were avoided in this study.

It was determined that the nitric acid microwave assisted digestion was a reliable means for the quantification of 15 out of the 18 elements within commercially available CB materials. In order to establish metal profiles for CB, estimations of Sb, Cd, and Zn were also included in the analysis of the commercial CB materials.
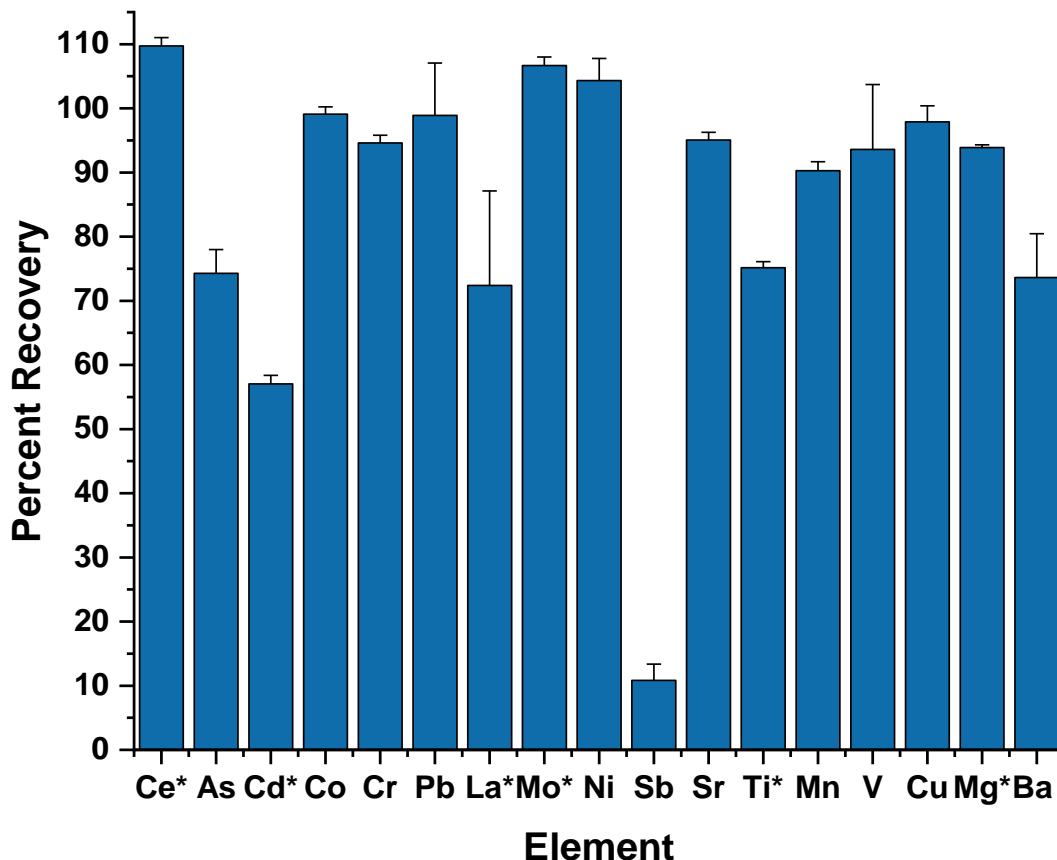
Figure S1: Recoveries for metal impurities within NIST SRM 1635a, as well as one metal from 1633c (La). Values reported with an * refer to reference mass fractions, while all other elements are certified values.

S3. Impact of Triton X-100 on Single Particle Analysis

In spICP-MS analysis, the mass flux calibration determines masses of particle occurrences from detector signal (counts). This incorporates both the dissolved La calibration as well as the transport efficiency determined from the Au NP standard to account for the percentage of particle loss during sample uptake to the plasma. To test for the surfactant's potential impacts to transport efficiency and particle mass flux, the TX-100 was added to dissolved Au, particulate Au, and dissolved La standards utilized in the mass flux calibration with no appreciable change to either the slope or R^2 (Table S5)

Table S5: The slope, y-intercept, and coefficient of determination (R^2) from the mass flux calibration are displayed for calibrations done in the absence and presence of initial TX-100 concentrations.

	No addition of TX-100			0.05% TX-100		
	Slope	y-intercept	R^2	Slope	y-intercept	R^2
Mass Flux Calibration	2.4E+11	0.023	0.999	2.27E+11	-0.014	0.999

Note that the mass flux calibration is used to calculate masses of particle occurrences from the detector signal. This is accomplished by converting signal intensity to mass using a dissolved calibration and then taking into account the transport efficiency determined from a particle standard. This approach is described in detail by Pace, et al.[99] In this study, the TX-100 matrix was included dissolved Au, particulate Au, and dissolved La standards utilized in the mass flux calibration with no appreciable change to linear regression or coefficient of determination (R^2).

As discussed in the main body of the paper, the presence of false positive peaks in the blank solutions increased with TX-100 concentration and necessitated a blank subtraction step in the CB calibration curves. The number false positives at each TX-100 concentration and corresponding impact to the number of La peaks counted in CB samples is shown in Table S6. This supports that an optimum concentration of TX-100 at 0.15% in the sample matrix boosted the detection of CB particles with minimal impact to the number of false positives.

Table S6: The number of peaks in the analysis of 500 ppb of M1000 CB in various concentrations of TX-100. The false positives (bkg peaks) are shown here to display how they were subtracted to account for false positives arising from the addition of TX-100.

% surfactant	# peaks	(#peaks - bkg)	bkg peaks
0.1	75	68	7
0.15	83	79	5
0.2	68	59	9
0.3	65	52	12
0.5	97	64	32
0.75	80	57	23
1	83	58	25

S4. Comparison to Gravimetric Analysis and UV-visible Spectroscopy

In order to evaluate the effectiveness of spICP-MS compared to other methods for CB quantification, suspensions of unknown concentrations were produced in a simple filtrate study. In this study 100 mL of a concentrated M1000 CB solution (1000 mg/L) was vacuum filtered through a Whatman P3 filter (pore size 6 µm) in a Büchner funnel. 40 mL of DI water was used to rinse the Büchner funnel and the filter flask. The addition of 2.5 mL of TX-100, and additional dilutions brought the final volume of the filtrate to 150 mL. The CB concentration in the filtrate was then determined by gravimetric analysis, then UV-vis and spICP-MS after diluting 10x. The entire procedure for filtration and subsequent gravimetric, UV-vis, and spICP-MS analyses was carried out three times (trials 1, 2, 3).

Gravimetric analysis determined the CB concentration based on the difference between original dry mass of CB in the suspension pre-filtration and the CB dry mass collected on the filter. The dehydrated masses of CB and the filter paper were measured before and after the filtration. Before filtration, the CB used to make the concentrated suspension and the filter paper were dried in an oven at 110°C for two hours then allowed to cool in a desiccator for 20 min before weighing. Afterwards the filter paper with the accumulated CB was allowed to dry overnight at 110°C to ensure full dehydration before cooling in a desiccator and weighing.

Table S7: Comparison of filtrate concentrations based on calculations form the gravimetric analysis and the spICP-MS analysis for particulate La, based on a 10x dilution of filtrate.

Quantification method	Trial 1	Trial 2	Trial 3
[Gravimetric analysis]	7.32 ppm	5.9 ppm	4.75 ppm
[spICP-MS]	6.48 ppm	4.57 ppm	4.18 ppm
Percent agreement	88.52%	77.46%	88.06%
Average percent agreement	**84.68%**		

With an average percent agreement of approximately 85%, this simple validation study shows good agreement between the calculated concentration of the filtrate based on mass differences and quantification by spICP-MS utilizing La as a tracer. The 15% disparity between these values may result from CB loss to glassware surfaces during filtration and transfer processes. Another contributing factor may be that CB M1000 contains 6.1% moisture (Table S3), which was not accounted for in procedure to prepare the spICP-MS calibration curves. The calibration procedure was designed with practicality in mind and dehydration is not required for the technique, therefore the added time for constant dehydrations of CB M1000 stock solutions was deemed unnecessary.

For the UV-vis and spICP-MS determination of concentration, the filtrate was first diluted by a factor of 10. To determine the concentration via UV-vis, a 5-point calibration curve was established with excellent linearity as seen in Figure S2. UV-vis measurements were performed on an Ocean Optics Flame spectrophotometer, with $\lambda=447.48$ nm, an integration time of 1.1 ms, 100 scans to average, and boxcar width of 10. The spICP-MS analysis was carried out as described in the main body of the paper. The comparison resulted in an excellent agreement of 91.7% between spICP-MS and UV-vis for the quantification of CB M1000 in a deionized water matrix.

When the test was repeated on a CB suspension in a synthetic drinking water matrix (described in Section S5), agreement between the methods was 93.4% (Figure S5). This indicates that in a matrix containing common ions at concentrations representative of a drinking water source would have little to no effect on the quantification capability of the proposed method.
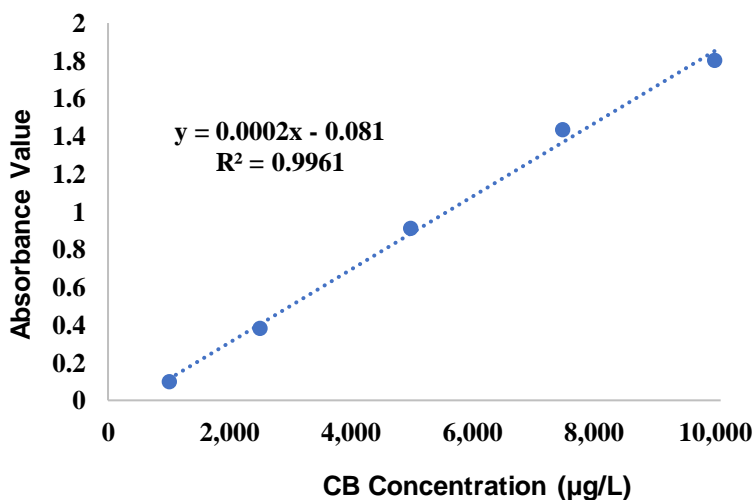
Figure S2: Five-point calibration for UV-vis absorption spectroscopy of CB M1000 suspension in DI water, λ=447.48 nm.
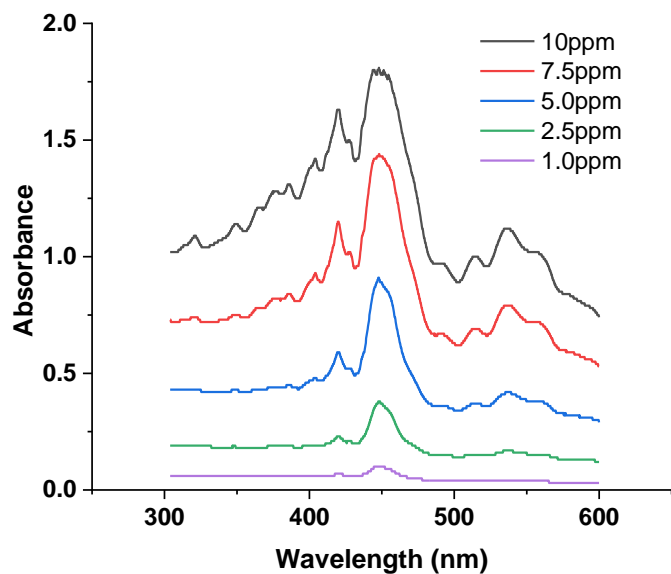
Figure S3: UV-VIS absorption spectra from 300 to 600 nm for 10, 7.5, 5, 2.5, and 1 mg/L suspensions of CB in water.

As previously discussed, although the spICP-MS results are in good agreement with UV-vis and gravimetric analysis in all three trials, spICP-MS is the only analytical technique capable of extending CB quantitation below 1 mg/L. While linear calibration is possible for UV-vis down to 0.1 absorbance units, accurate determination of concentration cannot be expected at values much below this point. Similarly, gravimetric analysis becomes impractical for handling sub-mg samples and the likelihood of error from loss to container surfaces increases. On the other hand, the spICP-MS method developed has been shown to quantify CB as low as 122 µg/L and reliably detect starting at 64 µg/L of CB M1000 in water.

S5. Tests for Matrix Effects in the Presence of Dissolved La and Major Ions in Drinking Water

When dissolved La was added to CB samples at environmentally relevant concentrations (based on average abundance in surface waters), no significant impact to the method sensitivity or detection was observed.
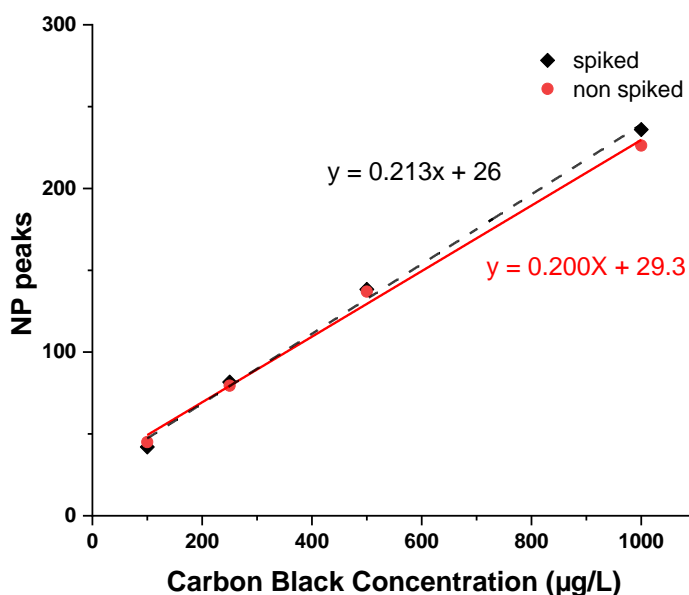
Figure S4: Calibration curves based on four concentrations of CB in spiked (4 ng/L of dissolved La in MilliQ + 0.15% TX-100) and non-spiked matrices (MilliQ + 0.15% TX-100).

In order to test the performance of this method for CB measurement in a matrix similar to what would be expected in water samples used in drinking water treatment, major cations and anions (Na^+, Ca^{2+}, Mg^{2+}, K^+, HCO_3^-, Cl^-, SO_4^{2-}) common to drinking water matrices were spiked into CB suspensions used in the filter tests described in Section S4.[117] The synthetic drinking water matrix was formulated based on the reported concentrations[118] of the Wasatch Aquifer as an example of a drinking water source which also meets the definition of a mineral water[119] by having total dissolved solids of 263 mg/L. Table S8 below shows the ionic composition of the Wasatch aquifer in comparison to the synthetic drinking water matrix created in this study.

Table S8: Comparison of the most abundant ionic components between USGS analysis of a Wasatch aquifer and synthetic drinking water matrix utilized in this study.

	Ca (mg/L)	Mg (mg/L)	Na (mg/L)	K (mg/L)	Cl (mg/L)	HCO_3 (mg/L)	SO_4 (mg/L)	Dissolved Solids
Wasatch Aquifer	6.2	1.5	97	2.2	8.1	251	13	263
Synthetic water matrix	6.2	2.6	147.9	2.2	10.97	251	13	–

The presence of major cations and anions in the CB suspensions at concentrations relevant to waters used in treatment technology development did not result in major differences to the CB concentration determined in the filtration test described in the previous section (Figure S5 below).
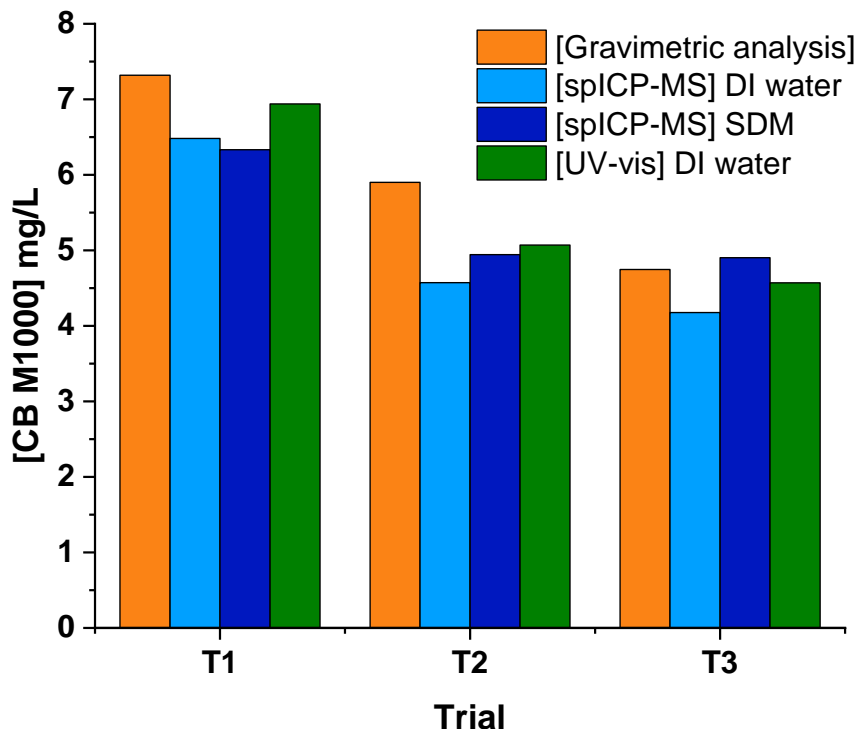
Figure S5: Quantification comparison between gravimetric analysis, spICP-MS analysis in a deionized water matrix, spICP-MS analysis in synthetic drinking water (SDW) matrix, and finally UV-vis.

S6. Considerations for particle sizing analysis

Data from the previous section was utilized for the determination of a threshold value (discrimination of background/dissolved analyte from a nanoparticle event) for the detection of carbon black by spICP-MS analysis. The threshold serves as the minimum intensity a nanoparticle event must surpass to be considered distinguishable from the background. This value can be used to calculate the smallest particle size possible under specified parameters.[309] Figure S6 shows an analysis of blank (0.15% TX-100) under the same dwell time as studies conducted for the optimization of the TX-100. Out of caution, the background threshold determined by the Syngistix Nano software was manually overridden to 5 counts to exclude any false positives.
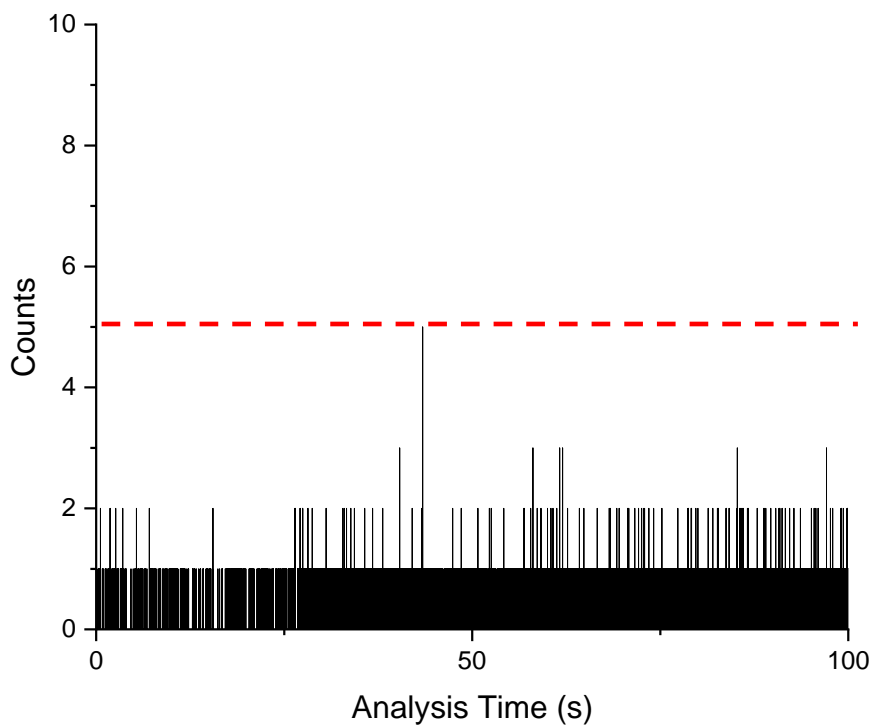
Figure S6: Determination of necessary threshold for spICP-MS analysis.

The threshold value can be applied to the following calculation to estimate the particle size limit of detection (LOD_{size}), in which A refers to the intensity of nanoparticle pulse, B is the average background intensity of a sample, C refers to the y-intercept of the mass flux calibration curve, X is the slope of the mass flux calibration, Y is the analyte mass fraction, and Z is the density of the particle[309].

$$LOD_{size} = \left(6 * \frac{A - B - C}{X * Y * Z * \pi} \right)^{1/3}$$

This equation indicates that accurate calculation of particle size from the La mass is highly dependent on the chemical speciation of the La-containing particles. The actual mass fraction of La in CB particles as well as density has not been established and likely varies between different CB materials (i.e. Monarch versus Vulcan product lines), and potentially even may vary between individual particles within a given sample. A previously published study on carbon nanotubes synthesized via a similar process of arc discharge (where La_2O_3 was used as the filament source)

identified the La species as LaC_2.[310] For demonstration, we estimated the smallest detectable CB particle size using LaC_2, La_2O_3, and pure La as particle species. The corresponding analyte mass fractions, particle densities, and resulting size LOD are provided below. The adjustment of the background threshold to 5 counts, which corresponded to a LaC_2 diameter of ~18 nm, also appeared to reduce the variability between replicate size distributions.

Table S9: Estimation of smallest detectable particle for three various La containing particles

Identity	Mass fraction	Particle Density (g/cm^3)	Size LOD (nm)
LaC_2	0.837	5.29	18.4
La_2O_3	0.853	6.51	17.1
La	1	6.16	16.5

Since a conclusive La speciation within the CB materials was beyond the scope of the present study, further analysis of the size distributions generated by spICP-MS was carried out leaving the measured sizes in terms of the La mass detected in each CB particle event. Because the Syngistix Nano application exports particle data in pre-sorted and binned size histograms, it was necessary to reverse this process and create a list of unbinned particulate La masses measured in each sample prior to statistical testing. A script was written in R Studio to transform the individual La mass histograms from each replicate into a list of each particulate La mass measured, repeated for the number of times a peak corresponding to that La mass was detected. The resulting list of masses for each replicate were then tested for statistical equivalence by non-parametric Kruskal-Wallis ANOVA and post-hoc Dunn's Test of pairwise comparisons. While the replicates of each concentration were not significantly different from each other, many comparisons between different concentrations differed. The complete tabulated results available in the excel file additionally available as supplementary material. The list of measured masses for statistically equivalent replicates were combined for the side-by-side comparison of all concentrations shown

in Figure 5 in the main text, as well as Figure S7 below. Descriptive statistics of the combined size datasets for each concentration are shown in Table S10 below.

Table S10: Descriptive Statistics over the observed La particle masses in carbon black particles over large concentration range (75-10,000ppb)

CB Conc. (µg/L)	n total	Mean (fg La)	Standard Deviation (fg La)	Sum (fg La)	Mode (fg La)	Minimum (fg La)	Median (fg La)	Maximum (fg La)
75	316	0.4839	0.95808	152.913	0.01877	0.01877	0.06334	7.74293
100	180	0.79815	1.03927	143.6667	0.01877	0.01877	0.22179	5.56077
200	261	0.41933	0.82444	109.446	0.01877	0.01877	0.05028	5.02302
250	318	0.6317	1.03659	200.8812	0.02207	0.01877	0.09138	6.13559
500	548	0.70071	1.1468	383.9869	0.02207	0.02207	0.09587	7.74293
750	673	0.71831	1.12186	483.4238	0.02207	0.02207	0.10545	6.74871
1000	894	0.76147	1.16174	680.7502	0.02207	0.01877	0.10545	8.09483
2500	1789	0.80392	1.06534	1438.221	0.01877	0.01877	0.29324	8.64242
5000	3630	0.90699	1.23023	3292.357	0.02207	0.02207	0.31323	9.02087
10000	7977	0.98068	1.24053	7822.904	0.01877	0.01877	0.45248	8.8303
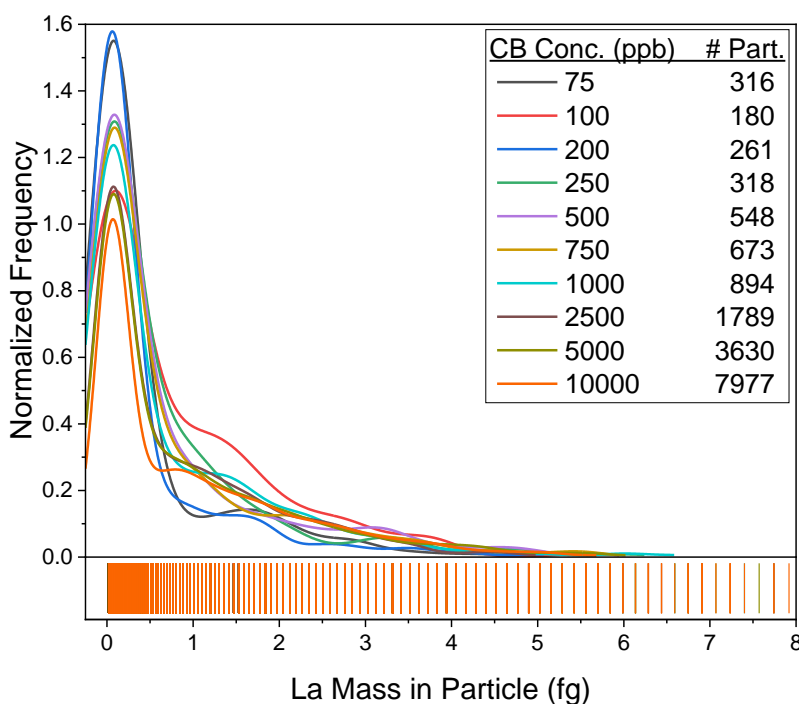
Figure S7: Overlayed distribution curves and rug plot for the observed La masses in carbon black particles over large concentration range (75-10,000 µg/L).

CB M1000 suspensions were analyzed by dynamic light scattering (DLS, Brookhaven Instruments – NanoBrook 90Plus PALS) to determine hydrodynamic sizes of the M1000 particles. Comparison of the DLS size distribution to the La mass distribution measured by spICP-MS may be informative, though interpretation must be limited in consideration that DLS and spICP-MS differ greatly in their fundamental bases and size calculations from light scattering are prone to artifacts in complex particle suspensions. The spICP-MS distributions indicate the frequency at which La is present in various masses in individual particles, while the DLS distribution provides an estimation of the range of hydrodynamic diameters of CB particles. The DLS results (Figure S8) indicate a bimodal size distribution, with each relatively narrow ranges in size around 200 and 900 nm.
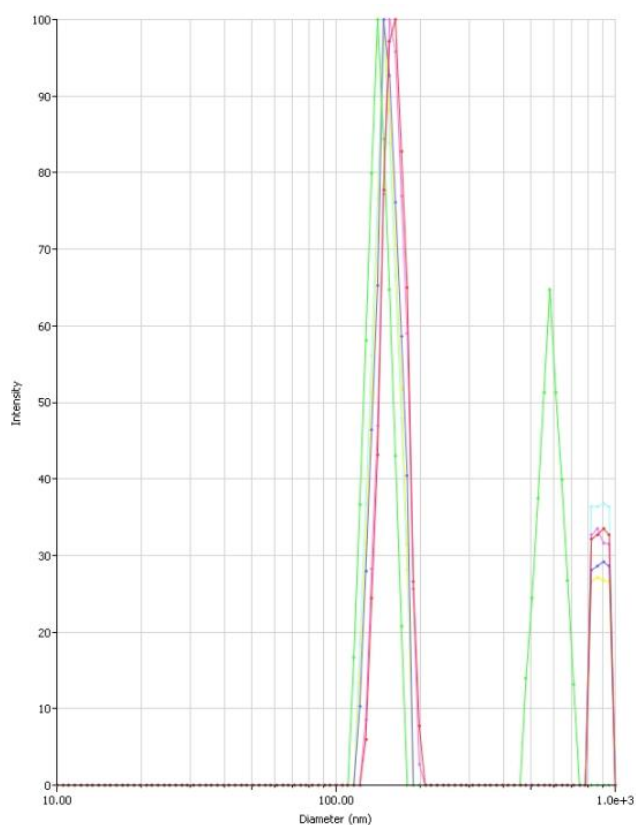
Figure S8: Hydrodynamic size distribution of M1000 CB determined via DLS.

Although this distribution differs from the distribution of La masses, the two techniques are not necessarily in disagreement. While the narrowness of the interquartile range around the ~200 nm mode size is reflected in the sharpness of the spICP-MS mode at 0.02 fg, the presence of the second mode at ~900 nm may be reflected in the shoulder around 1.5 – 2 fg. Light scattering is poorly suited to polydisperse samples, so it's possible that the presence of particles between 300 – 800 nm are present even though they are not reflected in the DLS data. It is also possible that if higher resolving power between La masses was available, the shoulder on the spICP-MS distribution might instead be separated into a bimodal distribution. Additionally, it is possible that even with the use of surfactant, some aggregation occurred in the DLS cuvette which was not observable in the sample taken up into the ICP-MS. However, this is somewhat speculative and to avoid overinterpretation, we refrain from utilizing the DLS sizing results to estimate the mass fractions of La within the varying sizes of carbon particles. This subject would be interesting to study in future work, with additional complementary characterization such as electron microscopy and energy dispersive spectroscopy.

PERMISSIONS FOR CHAPTER I, II, & III

CCC

RightsLink

🏠 Home   ❓ Help ∨   ✉ Email Support   👤 Sign in   👤₊ Create Account

Environmental applications and recent innovations in single particle inductively coupled plasma mass spectrometry (SP-ICP-MS)

Author: Kenneth Flores, , Reagan S. Turley, et al

Publication: Applied Spectroscopy Reviews

Publisher: Taylor & Francis

Date: Jan 2, 2021

Rights managed by Taylor & Francis

Thesis/Dissertation Reuse Request

Taylor & Francis is pleased to offer reuses of its content for a thesis or dissertation free of charge contingent on resubmission of permission request if work is published.

BACK   CLOSE

CCC

RightsLink

🏠 Home   ❓ Help ∨   ✉ Email Support   👤 Sign in   👤₊ Create Account

ACS Publications
Most Trusted. Most Cited. Most Read.

Targeting Metal Impurities for the Detection and Quantification of Carbon Black Particles in Water via spICP-MS

Author: Kenneth Flores, Logan N. Rand, Carolina Valdes, et al

Publication: Environmental Science & Technology

Publisher: American Chemical Society

Date: Oct 1, 2022

Copyright © 2022, American Chemical Society

PERMISSION/LICENSE IS GRANTED FOR YOUR ORDER AT NO CHARGE

This type of permission/license, instead of the standard Terms and Conditions, is sent to you because no fee is being charged for your order. Please note the following:

- Permission is granted for your request in both print and electronic formats, and translations.
- If figures and/or tables were requested, they may be adapted or used in part.
- Please print this page for your records and send a copy of it to your publisher/graduate school.
- Appropriate credit for the requested material should be given as follows: "Reprinted (adapted) with permission from {COMPLETE REFERENCE CITATION}. Copyright {YEAR} American Chemical Society." Insert appropriate information in place of the capitalized words.
- One-time permission is granted only for the use specified in your RightsLink request. No additional uses are granted (such as derivative works or other editions). For any uses, please submit a new request.

If credit is given to another source for the material you requested from RightsLink, permission must be obtained from that source.

BACK   CLOSE WINDOW

CCC
RightsLink

🏠 Home   ❓ Help ⌄   ✉ Email Support   👤 Sign in   👤➕ Create Account

---

ACS Publications
Most Trusted. Most Cited. Most Read.

Outlining Key Perspectives for the Advancement of Electrocatalytic Remediation of Nitrate from Polluted Waters

Author: Kenneth Flores, Gabriel Antonio Cerrón-Calle, Carolina Valdes, et al

Publication: ACS ES&T Engineering

Publisher: American Chemical Society

Date: May 1, 2022

Copyright © 2022, American Chemical Society

CURRICULUM VITAE

Kenneth Flores was born in 1993 in Harlingen, Texas and grew up in the Rio Grande Valley. He completed his Bachelor of Science Degree in Chemistry at the University of Texas Rio Grande Valley in December of 2016. During his undergraduate studies Kenneth began with environmental chemistry research, specifically in the removal of heavy metals from water with nano adsorbents. In January of 2017, Kenneth began his M.S degree in Chemistry where he focused on the photocatalytic degradation of herbicides in water. In December of 2018, he defended his M.S thesis work on "The effect of hybrid zinc oxide/graphene oxide (ZnO/GO) nano-catalysts on the photocatalytic degradation of simazine" and earned his degree from the University of Texas Rio Grande Valley.

In January of 2019, Kenneth joined the doctoral program in Chemistry at the University of Texas at El Paso. Kenneth was supported by the UTEP Doctoral Excellence Fellowship for tuition and by Dr. Gardea-Torresdey's NSF ERC NEWT (EEC-1449500) in the UTEP Chemistry Department as a research assistant. Kenneths's research during his doctoral studies focused on novel detection methods for nanoparticles, single particle ICP-MS analysis, and electrocatalytic remediation of nitrate from polluted waters. Kenneth has a total of four first author and thirteen coauthor peer reviewed publications.

Mr. Flores may be contacted at flrs_knny@yahoo.com

Permanent Address: 14414 Coyote Trai Dr.

El Paso, Tx, 79938